DEVELOPMENT AND TESTING OF A WALL-SHEAR-STRESS SENSOR FOR MEASUREMENTS WITHIN NOTEBOOK COMPUTERS

by

Samer Afara

Department of Mechanical Engineering

McGill University
Montréal, Québec, Canada

December 22, 2011

A thesis submitted to the Faculty of Graduate Studies and Research in partial fulfilment of the requirements for the degree of Master of Engineering

Abstract

The design, construction, and validation of a novel wall-shear-stress sensor, and measurements obtained using this sensor in air flows downstream of blockages in a mini-channel are presented and discussed in this thesis. The novel sensor consisted of a hot-wire mounted over a small cavity, and operated using a constant-temperature anemometer. The flows investigated herein have features similar to those within the mini-channels inside notebook computers. The main goal of this work was to develop a sensor suitable for measurements of the wall-shear stress in such flows, which can be used to validate corresponding numerical simulations, which are known to be often surprisingly inaccurate. The values of Reynolds number investigated (based on average velocity and hydraulic diameter) ranged from 100 to 1000, and the mini-channel heights considered were 2 and 4 mm. The average and root-mean-square wall-shear stresses were obtained at different distances downstream of the blockages, with blockage ratios of 39.7%, 59.2%, and 76.2%. Also obtained were (complementary) pressure distributions over three blockages, with blockage ratios of 38%, 57%, and 76%. The results confirmed the presence of unsteadiness, separation, reattachment, and laminar-turbulent transition. The novel wall-shear-stress sensor was determined to be suitable for measurements in such flows, with some limitations. Design modifications are suggested to improve its performance.

Résumé

La conception, construction, et validation d'une nouvelle sonde capable de mesurer la contrainte de cisaillement est présentée dans le cadre de cette thèse. La nouvelle sonde est évaluée en écoulements d'air en aval d'une obstruction placée au sein d'une mini-conduite de section transversal rectangulaire. La sonde est composée d'un fil-chaud placé au-dessus d'une cavité et opérée au moyen d'un anémomètre à température constante. Les écoulements d'air étudiés sont semblables aux mini-conduites trouvées à l'intérieur d'ordinateurs portables. L'objectif principal de ce travail est de développer une sonde capable de mesurer la contrainte de cisaillement et de fournir des résultats expérimentaux pour valider les simulations numériques dans de tels écoulements qui se manifestent complexes. Les nombres de Reynolds (basés sur la vitesse moyenne et le diamètre hydraulique) des écoulements en mini-conduite variés de 100 à 1000, et les épaisseurs des conduites ont été de 2 et 4 mm. La moyenne et la moyenne quadratique de la contrainte de cisaillement sont measurées à de différentes distances en aval de trois obstructions ayant des rapports d'obstruction (l'épaisseur de l'obstruction divisé par l'épaisseur de la conduite) de 39.7%, 59.2%, et 76.2%. Pour compléter ces données, la distribution de la pression statique est mesureé au-dessus de trois obstructions ayant des rapports d'obstruction de 38%, 57%, et 76%. Les résultats confirment l'existence de plusieurs phénomènes, tels que l'instabilité, la séparation, le recollement, et la transition laminaire-turbulente. La nouvelle sonde s'est avérée practique pour la mesure de tels écoulements, bien qu'elle possède quelques limitations. Des modifications qui amélioront sa performance sont proposées.

Acknowledgments

I would like to express my innermost gratitude to my two supervisors, Professor B. Rabi Baliga and Professor Laurent Mydlarski, for giving me the opportunity to work on such a challenging and interesting project. I would also like to thank them for guiding and helping me throughout this work and for passing on to me some of their wisdom, knowledge, and experience. Furthermore, I would like to thank them for their financial support and for making this experience enjoyable.

I would like to thank Intel Corporation for funding this project. More specifically, I would like to thank Dr. Mark Macdonald, who was directing the project from Intel and whose advice and recommendations were very important contributions to this work.

I could not have completed this project in time without the help of my laboratory partners, Professor Baliga, James Medvescek, Alexandre Lamoureux, and Brandon Tulloch. I would especially like to thank James Medvescek for helping me design and construct the channel, laminar flow elements, and novel sensor, and for assisting me during my experimental runs. I am also very grateful to Mr. Juan Vasquez and Mr. Ariel Kemer of Arsal Industries, and the technical staff of the Faculty of Engineering [Antonio (Tony) Micozzi, Sam Minter, J. Roy Westgate, Andy Hofmann, Gary Savard, and John Boisvert], for their invaluable help in machining various elements of the experimental setups. Thanks are also due to Ms. Joyce Nault for her help with the formalities of graduate school and the thesis submission tasks.

Special thanks are owed to Professor Mydlarski, Arpi Berajeklian, and Jason Lepore for teaching me the practical aspects of hot-wire anemometry and the fundamental principles of turbulent flow measurements. I would also like to thank Jeffrey Poissant for letting me use his stereomicroscope, which allowed me to take some wonderful pictures of the novel sensor.

I owe my dearest thanks to my mother and to my sister for their continuous love and support. To my father, thank you for shaping me into the man I am today. You will always be loved.

Table of Contents

List of Figures

List of Tables

Nomenclature

English Symbols

a	Gap height of test section
A	Hot-wire and hot-film anemometry calibration constant
A_{cs}	Cross-sectional area of duct
b	Width of test section (spanwise direction)
B	Hot-wire and hot-film anemometry calibration constant
BR	Acronym for blockage ratio
D_h	Hydraulic diameter
D_i	Inner diameter of laminar flow element tubes
D_w	Diameter of a hot-wire
E	Anemometer voltage output
H	Actual height of blockage (including double-coated tape thickness, if applicable)
H_d	Channel height downstream of a backward-facing step
H_u	Channel height upstream of a backward-facing step
L	Length between the two pressure taps located on the laminar flow element tubes
L_c	Length of the laminar flow element tube used in the calculation of D_i
L_{TS}	Length between the test-section-wall-static-pressure taps used to measure ΔP_{TS}
L_w	Length of a hot-wire
m_1	Mass of the laminar flow element tube (length = L_c) used in the calculation of D_i
m_2	Mass of the water and laminar flow element tube (length = L_c) used in the calculation of D_i
M	Total mass flow rate through the test section or the laminar flow elements
M_{FE}	Mass flow rate in one laminar flow element tube
n	Hot-wire and hot-film anemometry calibration constant
P	Density of air
P_{abs}	Absolute pressure of air
P_{atm}	Atmospheric pressure in the Laboratory

P_{std}	Standard atmospheric pressure of air
P_w	Wetted perimeter of duct
P_x	Pressure gradient (dP/dx) in the test section along the streamwise direction
ΔP_{FE}	Pressure drop across the pair of pressure taps located on each laminar flow element tube
ΔP_{TS}	Largest pressure drop measured by the test-section-wall-static-pressure taps
R_a	Hot-wire ambient-temperature resistance
R_{cable}	Electrical resistance of the 5 m BNC cable connecting the TSI support column to the constant temperature anemometer or multimeter
R_{column}	Electrical resistance of the TSI support column
$R_{contact}$	Electrical contact resistance between the sensor and the TSI support column
R_{pr}	Electrical prong resistance of the sensor
R_w	Hot-wire operating resistance
Re	Reynolds number
Re_{FE}	Reynolds number in each laminar flow element tube
Re_{TS}	Reynolds number in the test section
T_a	Hot-wire ambient temperature
T_{abs}	Absolute temperature of air
T_w	Hot-wire operating temperature
TS	Acronym for test section
u	Instantaneous velocity of a fluid along the streamwise direction
U	Instantaneous velocity of a fluid perpendicular to a hot-wire
U^+	Dimensionless instantaneous velocity unit
U_τ	Shear or friction velocity
V_{out}	Output voltage
W	Dimensionless velocity
X	Distance between the downstream-end of the blockage and the sensor
X_1	Reattachment length of primary recirculation zone
y	Height from the bottom surface of a duct
Y^+	Dimensionless height unit from the bottom surface of a duct

Greek Symbols

α	Overheat ratio
β_n	Parameter used in equation 3.9
γ	Flow angle
η	Wall-shear-stress turbulence intensity
λ_n	Parameter used in equation 3.9
μ	Dynamic viscosity of air
ν	Kinematic viscosity of air
ρ_w	Density of water
τ_{avg}	Average value of wall-shear stress
τ_{rms}	Root-mean-square value of wall-shear stress fluctuations
τ_w	Wall-shear stress
Ω	Parameter that accounts for the geometry of the test section in equation 4.1

Chapter 1

Introduction

1.1 Background, Motivation, and Overall Objectives

Notebook computers are becoming increasingly popular because their performance is approaching that of desktop computers; yet, they are getting smaller and lighter; and, most importantly, they are portable. Their popularity has made them the primary market for some computer manufacturers. There is a relentless push to make notebook computers faster and more powerful, while reducing their size and weight, and lowering their cost. One of the important factors limiting the performance of notebook computers is their ability to effectively reject the heat dissipated by their various electronic components. This task is becoming even more challenging because the amount of heat dissipated by these devices per unit volume is continually increasing. To keep up with these challenges, and to meet anticipated future needs, engineers at Intel Corporation, which is a leader in notebook cooling technologies and also a sponsor of the research reported in this thesis, are currently interested in improving their thermal management solutions.

To this day, the most practical and cost-effective cooling technology for notebook computers remains air cooling. It consists of forcing air through the mini-channels (of heights ranging from 1 to 4 mm) present within these devices. The mini-channels are bounded by the casing and the various electronic components, which are cooled by the air flow. However, the air flow is partially blocked by these components, resulting in fluid flow phenomena such as unsteadiness, separation, reattachment, and laminar-turbulent transition. The numerical simulation of the thermal and hydraulic aspects of such flows is very difficult and Intel is interested in obtaining experimental data to validate their numerical models and verify their simulation results. This data can also provide some very interesting and useful insights on these flows. These facts are the main motivation behind this thesis.

Having provided the context and motivation for this work, its main goals can now be discussed. The data that Intel wants to obtain requires measurements of a quantity that can be used to assess the various phenomena encountered in the flows within notebook computers. The

question remains as to which such quantity is representative of these flows and yet lends itself to reliable measurements. The most popular candidate, and perhaps the first one to come to mind, is velocity. However, air velocity measurements are difficult to obtain in the mini-channels within notebook computers, because commercially available velocity sensors are simply too big to fit inside them. Even if they did somehow fit, these sensors are incapable of accurately measuring the flow in the vicinity of boundaries, which is a significant problem in such mini-channels. Furthermore, commonly used air velocity sensors, such as hot-wire and hot-film sensors, are often intrusive, so they disturb the flow field and compromise the accuracy of the resulting measurements. There are other techniques for measuring flow velocity, such as laser-Doppler anemometry and particle-image velocimetry, which are nonintrusive to the flow field. However, these techniques require optical access, which is very difficult, if not effectively impossible, to meet within a notebook computer. An alternative approach to investigating the flows within notebook computers is the measurement of the wall-shear stress. As the name implies, this measurement is performed at the boundaries of walls and can therefore be nonintrusive to the air flow. Wall shear-stress sensors, unlike velocity sensors, are usually inserted from the bottom of channels. This removes the problem of having to fit them in the confined spaces within these mini-channels. These two facts make these sensors ideal for this work. Multiple wall-shear-stress-measurement techniques have been used in the literature. However, the commercially available ones have inadequate response times and are therefore not suitable to the flows of interest, as will be explained later. Consequently, the main goal of this thesis is to design and construct a novel sensor that is suitable for measuring wall-shear stress in flows that are geometrically and physically similar to the ones encountered within notebook computers.

1.2 Specific Objectives

In this thesis, five specific objectives are proposed to accomplish the main goal described in the previous section: 1) determination of the relevant dimensionless parameters that characterise the flows within the mini-channels of notebook computers; 2) based on these parameters, design and construction of a geometrically similar mini-channel; 3) design, construction, calibration, and validation of a novel wall-shear-stress sensor inside this mini-channel; 4) measurements of wall-shear stress at various distances downstream of partial blockages of different heights inserted in the aforementioned mini-channel; and 5) measurements

of the pressure distribution over these blockages, as complementary data to the wall-shear-stress measurements.

1.3 Literature Review

The design and construction of the experimental apparatus and the novel wall-shear-stress sensor required knowledge of i) the cooling of notebook computers, ii) the fluid flow over and in the vicinity of partial obstructions in ducts, and iii) the available wall-shear-stress measurement techniques. A review of the published literature on these subjects was done and is presented below.

1.3.1 Cooling of Notebook Computers

According to Mouromtseff (1942), early thermal issues in electronics were solved by "the cut-and-try method" rather than by calculations. However, with the advancements in technology and performance, thermal considerations are now becoming integral to the early stages of the design process (Bergles 2003). The notebook computer industry has always struggled to remove the heat generated by the ever-growing number of electronic components (semiconductor devices), even though the efficiency of these components has drastically increased. For this reason, the power required to cool these computers has increased relative to the power inputs to the semiconductor devices (Yazawa and Bar-Cohen, 2002) and yet the packaging size has decreased. To understand the significance of this problem, it is important to become familiar with the system-level cooling techniques used in modern notebook computers.

Depending upon their performance, a total of 15 to 30 W of heat is typically generated by the components of notebook computers. The major components responsible for this heat generation are: the graphics processing unit (GPU), CD-ROM, hard-disk drive, power supply, battery, and, most importantly, the central processing unit (CPU), which produces almost 50% of the total heat generation. The heat generated by the CPU must be dispersed effectively or "hot-spots" will be formed underneath it. It is transported away using either a thin aluminum bar or a heat pipe. The evaporator end of the heat pipe is connected to the CPU, while the condenser end is attached to a finned surface that is usually exposed to the ambient air (Bergles 2003). A fan is then used to blow air through the finned surface to reject the heat that was transported from the

CPU. At the same time, the air flowing through the computer is used to cool the other components via forced convection. The remaining components that are not exposed to any air currents are cooled by natural convection, conduction and radiation.

As was previously mentioned, air cooling remains the most popular and cost-effective technique for the thermal management of notebook computers. However, as these devices are becoming both smaller and more powerful, both the hydraulic resistances of the airflow passages and the required rates of cooling are increasing. This means that unless some special cooling techniques are developed and implemented, a bigger, noisier, and more powerful fan will eventually be needed to effectively reject the heat in an environment where the space allocated for this task is limited. Furthermore, the battery life will be considerably reduced if a more powerful fan is used. These are the challenges that thermal management engineers are faced with today, and it is generally expected that micro-channel heat exchangers will be the breakthrough that will enable them to keep up with the rapid pace of advances in electronic devices (Garimella et al. 2002). However, significant research remains to be done before such technologies become commonly available, which means that the focus still lies in maximizing the efficiency of current cooling technologies, usually achieved by undertaking numerical modelling, rather than experimenting with different prototypes. This strategy reduces the design times and related costs, and it has enabled effective cooling solutions. However, there is an urgent need for benchmark data that can be used to validate these models, which requires a fundamental understanding of the flows encountered within notebook computers (Garimella et al. 2002).

1.3.2 Fluid Flow Over and In the Vicinity of Partial Obstructions in Ducts

Flows within notebook computers have been investigated numerically by thermal-management engineers working in the notebook computer industry. To the best knowledge of the author, there are very little or no in-situ experimental data suitable for validating these specific numerical models. The paucity of such experiential data can be attributed to the difficulties involved in using commercially available fluid-flow sensors within notebook computers, which is why a novel sensor is needed. However, the design of such a sensor is dependent on the type of flows that will be investigated. Therefore, a fundamental understanding of these flows is first required. As an initial effort to gain such an understanding, a notebook computer was provided to the author and his thesis supervisors by Intel, and the author conducted some rudimentary

measurements on this computer. From these measurements, it was determined that the hydraulic diameters[1] of the mini-channels directing the air flow within the computer ranged between 2 and 8 mm, and that the values of Reynolds number (Re), based on the average velocity and hydraulic diameter, ranged between 100 and 1000. It was also found that the electronic components present within these mini-channels could be represented by partial blockages, with blockage ratios (BR = blockage height / channel height) ranging between 20% and 80%. This preliminary analysis also showed that these flows are similar to those over and in the vicinity of partial obstructions in closed channels. Such flows have been investigated extensively in large channels both numerically and experimentally. However, no attempt has been made to measure the wall-shear stress in mini-channels (values of hydraulic diameter between 2 mm to 8 mm) with values of Reynolds numbers similar to those encountered within notebook computers.

Carvahlo et al. (1987) measured the velocity profiles of the flow downstream of blockages (BR = 25%, 50%, and 75%) that were inserted on the bottom surface of a closed 10 mm height channel for values of Reynolds numbers between 50 and 10000. They measured these profiles using laser-Doppler anemometry and compared the results to predictions obtained with different numerical schemes. Although their data did not contain any real-time wall-shear stress measurements, they showed that the flows downstream of blockages could be unsteady, and contain separation, recirculation, and reattachment zones. A primary recirculation zone was present on the bottom surface of the channel, immediately downstream of the blockages, for all blockage ratios and Reynolds numbers investigated. A secondary recirculation zone was present on the top surface of the channel, and downstream of the primary recirculation zone, for all blockage ratios higher than 25%. The reattachment length of the primary recirculation zone (X_1) was estimated from the velocity measurements. They noted that this length depended on both the blockage ratios and Reynolds number (based on average velocity upstream of the blockage and blockage height). They also observed three distinct regimes in the variation of X_1 with Re: a laminar regime ($Re < 250$) where X_1 increased with Re, a transitional regime ($250 < Re < 1500$) where X_1 decreased with Re; and finally, a turbulent regime ($Re > 1500$) where X_1 became relatively independent of Re. They also observed that X_1 decreased with increasing blockage

[1] The hydraulic diameter (D_h) is defined as four times the cross-sectional area (A_{cs}) for the flow divided by the wetted perimeter (P_w), which is the perimeter of the cross-sectional area that is exposed to the air flow. The hydraulic diameter is commonly used as the characteristic length scale for flows in non-circular ducts. For a large-aspect-ratio (width / height) channel, this parameter is two times the channel height.

ratio and explained that this trend was caused by the appearance of a secondary recirculation zone that appeared on the wall, on the opposite side of the blockage, at higher blockage ratios.

The previously described dependence of the primary reattachment length on the Reynolds number and blockage ratio follows a similar trend to that observed in flows in a channel with a backward-facing step[2] (Goldstein et al., 1970; Armaly et al., 1983; Lee & Mateescu, 1998). In such flows, the expansion ratio replaces the blockage ratio as the parameter of interest. It is defined as the ratio of the channel height downstream of the step (H_d) to the channel height upstream of the step (H_u). Furthermore, the Reynolds number is usually based on the average velocity upstream of the step and the step height (H_d - H_u). There have been numerous investigations of this type of flow. An extensive list of publications on this subject was provided by Le et al. (1997). Lee & Mateescu (1998) investigated the flow downstream of a backward-facing step numerically and verified their results experimentally using hot-wire sensors and closely-spaced, multi-element hot-film arrays. They tested expansion ratios ranging from 1.17 to 2.0 for Reynolds numbers smaller than 3000. Of particular relevance to the experiments herein is the work of Spazzini et al. (2001). They studied the unsteady flow over a backward-facing step by measuring the fluctuating wall-shear stress using a novel in-house sensor. Their results agreed with those in the literature, thus validating their experimental measurement technique. They also found that a region with high negative wall-shear-stress values existed inside the primary recirculation zone, and that the absolute maximum value of the wall-shear stress in this region decreased with increasing Re. This phenomenon was also reported by Eaton & Johnston (1980), Westphal et al. (1984), Adams & Johnston (1985), Driver & Seegmiller (1985), and Le et al. (1997).

So far, the present discussion has focussed on the flow downstream of blockages and backward-facing steps. However, the flows in channels with partial blockages or forward-facing steps[3] are of equal importance. Such flows have also been extensively investigated in the literature. Leclercq et al. (2001) and Addad et al. (2003) investigated flows over both backward- and forward-facing steps. Their results for the forward-facing step showed a region where a

[2]A backward-facing step in this case is essentially a sudden expansion of the channel towards the bottom (that is, the top surface of the channel remains unchanged, while the bottom surface is suddenly dropped).

[3]A forward-facing step in this case is essentially a sudden contraction of the channel towards the top (that is, the top surface of the channel remains unchanged, while the bottom surface is suddenly raised).

small recirculation bubble is formed immediately adjacent to the step, and another region on top of the step where a much larger recirculation bubble was formed.

The works discussed in the previous paragraphs demonstrate the importance of using a highly responsive sensor in the measurement of flows involving different types of blockage, given that unsteadiness of such flows is a common observation. These works also pointed out the presence of flow reversals, which means that the measurements must either be insensitive to flow direction or they must somehow account for them. These considerations were essential to the design of the novel wall-shear-stress sensor.

1.3.3 Techniques for Measuring Wall-Shear Stress

Many techniques are available for the measurement of the wall-shear stress. However, this discussion will be limited to the ones capable of measuring both average and fluctuating quantities. These techniques are classified into two distinct categories: direct and indirect.

1.3.3.1 Direct Techniques

As the name implies, direct techniques are capable of measuring the quantity of interest directly and do not require any calibration. Floating elements and oil-film interferometry represent the two most common direct techniques for measuring the wall-shear stress. A floating element is a sensor that is secured to a surface of interest and the wall-shear stress can be calculated based on how much it is strained. Such sensors are fundamentally problematic because they must have a surface area large enough to be able to accurately measure the wall-shear stress, yet must be small enough to have a high spatial resolution and frequency response (Fernholz et al., 1996). Micromachining technology has allowed researchers to minimize the surface area of the floating element without compromising the accuracy of the wall shear-stress measurement (Schmidt et al., 1988; Padmanabhan et al., 1995; Jiang et al. 1995). Unfortunately, there has not been enough research undertaken to validate the capabilities of such sensors and the microfabrication process remains costly. It is also difficult, if not impossible, to install such sensors in the confined air-flow passages inside notebook computers.

The other direct technique of relevance is oil-film interferometry. In this technique, the thinning rate of an oil film, which is linearly related to the wall-shear stress, is measured using

interferometry hardware. An elaborate explanation of its principles of operation, as well as an extensive list of references, is provided by Fernholz et al. (1996) and Ng et al. (2007). Contamination of the oil-film and the uncertainty in the properties of the oil are some of the problems that affect the accuracy of oil-film interferometry. Furthermore, Murphy & Westphal (1986) measured the skin friction on a boundary layer using this technique and noted that it suffered from response issues and surface-wave instabilities at high shear-stress values. Given these limitations, oil-film interferometry is not suitable to this research due to the space, mounting, and optical requirements for the interferometry hardware.

1.3.3.2 Indirect Techniques

Indirect techniques allow calculation of the wall-shear stress by the measurement of another quantity. One such technique is laser Doppler velocimetry (LDV) where the velocity of a small particle near the wall is measured by recording the Doppler-shift of laser light scattered from it, and the wall-shear stress subsequently calculated. Another technique, called particle image velocimetry (PIV), can be used to measure velocity by tracking particle displacement over a known time interval. Provided that i) the velocity is measured in the region very close to the boundaries, where the velocity profile is almost linear, and ii) the precise height of the measurement above the boundary is known, the wall-shear stress can be calculated. However, both LDV and PIV rely on the seeding of particles in the flow, and near the boundaries, the particle count is much lower due to particle lift-off caused by the sharp velocity gradient at the wall (Khoo et al 1996). This leads to discontinuous, biased, and non-uniform signals in the vicinity of walls, which renders these two techniques unsuitable for the measurement of the fluctuating wall-shear stress. Furthermore, both LDV and PIV require optical access (transparent enclosures), which is nearly impossible to achieve within notebook computers.

The most popular indirect technique is thermal anemometry, in which principles of heat transfer are used to deduce velocity or shear stress. Thermal anemometry can be divided into two main categories: hot-wire and hot-film anemometry. It has been used extensively for over 60 years for measurements of turbulent flow (Freymuth 1983a). The sensors used in these techniques are relatively inexpensive, have a good spatial resolution, and a fast frequency response, which makes them ideal for such measurements. The remainder of this literature

review will be dedicated to the description of both hot-wire and hot-film anemometry techniques, as well as their inherent limitations.

1.3.3.2.1 Hot-Wire Anemometry Techniques

The basic principles of hot-wire anemometry are explained in detail in Brunn (1995). A brief summary is provided here because it is essential to the understanding of its limitations. A standard TSI hot-wire sensor (model 1201) is shown in figure 1.1. The hot-wire consists of a tungsten or platinum wire with a very small diameter, ranging between 2 to 5 microns (μm). The wire is soldered or spot-welded to the tips of thin prongs that are connected to a constant-temperature anemometer (CTA) by means of a BNC cable. The CTA is an instrument that accomplishes two specific tasks. Firstly, it maintains the hot-wire at a user-set operating temperature (T_w) or equivalently, operating hot-wire resistance (R_w), greater than the ambient-flow temperature (T_a) or ambient-hot-wire resistance (R_a). Secondly, it outputs a voltage that is directly related to the power required to maintain the wire at this resistance. This power, under ideal conditions, is equal to the heat transfer from the wire, which can be related to the instantaneous velocity of a cross-flow (perpendicular to the hot-wire) using a semi-empirical convective heat transfer correlation. The final correlation, which relates the output voltage of the CTA to the cross-flow velocity, is called King's Law and is given in equation 1.1. In this equation, E is the output voltage of the CTA, U is the velocity of the fluid over the hot-wire, and A, B, and n are constants determined by calibration.

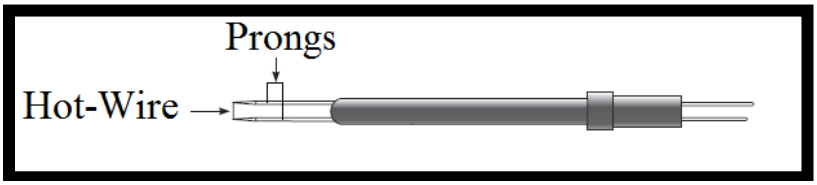

Figure 1.1 – Standard TSI hot-wire probe (model 1201)

$$E^2 = A + BU^n \tag{1.1}$$

To understand how a hot-wire can be used to measure the wall-shear stress, it is important to first note that for a laminar or turbulent flow, there exists a region very close to the wall called the viscous (or laminar) sublayer where the velocity profile is almost perfectly linear

in y (the wall-normal direction). This region extends from the wall to a dimensionless height value (Y^+) of 5, which is defined as:

$$Y^+ \equiv U_\tau \frac{y}{\nu}, \tag{1.2}$$

where $U_\tau \equiv \left(\sqrt{\tau_w/\rho}\right)$ is the shear or friction velocity, τ_w is the wall-shear stress, and ρ and ν are the density and kinematic viscosity of the fluid, respectively (Temekes & Lumley (1972); Pope (2000)). In this region, the velocity profile can be approximated by $U^+ = Y^+$, where $U^+ \equiv u/U_\tau$, and u is the instantaneous velocity of a fluid along the streamwise direction. Rearranging the above gives the wall-shear stress in terms of u and y:

$$\tau_w = \mu \frac{u}{y} \tag{1.3}$$

Commercial hot-wire manufacturers (such as Dantec and TSI) produce special near-wall-hot-wire sensors with bent prongs in order to minimize their interference with the flow near the wall. However, as indicated by, Wills (1962), Singh & Shaw (1972), Zemskaya et al. (1979), Bhatia et al. (1982), Azad (1983), Krishnamoorthy et al. (1985), Ligrani & Bradshaw (1987), Chew et al. (1995), Khoo et al. (1996), Chew et al. (1998a), and many other authors, a sensor calibrated in a wall-remote environment will lead to inaccurate measurements when it is brought in proximity to a wall. This causes the CTA output to be erroneously large, due to enhanced heat transfer to the wall. Furthermore, the extent of the region where the error starts to appear corresponds to the viscous sublayer region – the region of interest when making measurements of the wall-shear stress (i.e. $Y^+ < 5$). Before proceeding with the solution to this problem, a discussion of the nature of this error is in order.

Bhatia et al. (1982) investigated possible causes of the above-mentioned error by running a computer simulation of a linear-profile flow over a hot-wire mounted a small distance above the wall. The hot-wire was represented by an infinitely thin linear heat source, thereby neglecting any flow interference caused by it, and the wall was represented by both adiabatic (non-conducting) and conducting boundary conditions. Their results showed that the error increased with increasing proximity to the wall and increasing wall thermal conductivity. In the limit of an adiabatic wall, they showed that there was no error at all. They concluded that the sole cause of the increased CTA output could be attributed to the extra heat transfer to the wall. Chew et al.

(1995) ran a similar simulation, but represented the sensing element by an infinitely long cylinder, thereby accounting for flow interference. Their simulations also showed that the error increased with increasing proximity to the wall and increasing wall thermal conductivity, but that this error was not zero for an adiabatic wall. They therefore concluded, and verified experimentally (Khoo et al. 1996), that the error was attributed to both the extra heat transfer to the wall and the changes to the flow field resulting from the presence of the hot-wire in the vicinity of the wall. The effects of wall-wire interference have also been discussed by Comte-Bellot et al. (1965), and Azad (1983).

Other parameters also adversely affect near-wall hot-wire measurements. These include the effect of the wire diameter and the overheat ratio (α). The latter is defined as the ratio of the hot-wire's operating resistance to its ambient resistance. Zemskaya et al. (1979), Krishnamoorthy et al. (1985), and Chew et al. (1995) numerically determined that a hot-wire with a large diameter increased the heat transfer to the wall, thus increasing the error. However, there was debate as to the influence of the overheat ratio on the error. Theoretically, a higher overheat ratio leads to a higher hot-wire temperature, which should increase both the heat transfer to the flow and to the wall. These two effects are almost proportional to each other, thus removing the dependence of the overheat ratio on the percent error. This result was confirmed by the numerical simulations of Chew et al. (1995). However, Zemskaya et al. (1979) showed that higher overheat ratios lead to larger percent errors. The discrepancy between these two conclusions can be explained as follows. The model used by Chew et al. (1995) ignored conduction to the prongs because the hot-wire was represented by an infinitely long cylinder. In reality, the hot-wire has a finite length and the heat loss to the prongs is proportional to the wire temperature (or overheat ratio). Since heat transfer to the fluid decreases near the wall (due to low velocities), the three-dimensional effect of heat transfer to the prongs is more significant in that region. Therefore, using a greater overheat ratio will increase the percent error in near-wall measurements. Krishnamoorthy et al. (1985) also observed such three-dimensional conduction effects in their simulations because they simulated a hot-wire with a finite length. Therefore, their observation that overheat ratio affected the error was correct, although they failed to explain that it was simply due to three-dimensional effects. Blackwelder & Haritodinis (1983) and Ligrani & Bradshaw (1987) showed that the effects of three-dimensional prong conduction are minimized when the hot-wire's length to diameter ratio (L_w/D_w) is greater than 200. Chew et al

(1998b) verified this result experimentally and suggested that an (L_w/D_w) larger than 250 was necessary to remove any influence of the overheat ratio on the percent error.

To overcome the above limitations, different approaches have been undertaken. Chew et al. (1995) realised that for an adiabatic wall, errors only started to appear for $Y^+ < 2$, which is well within the viscous sublayer ($Y^+ < 5$). Therefore, if a wall with a sufficiently low thermal conductivity is used there is a region ($\approx 3 < Y^+ < 5$) where accurate wall-shear stress measurements can be obtained using equation (1.3). However, the extent of this region is i) very small, and ii) strongly dependent on the flow rate (or wall-shear stress), which makes this technique impractical. Another approach is for the sensor to be calibrated at a fixed distance from the wall (within the viscous sublayer) against a flow where the wall-shear stress is known. The extra heat transfer to the wall, as well as the interference caused by the hot-wire in proximity to the wall, is then incorporated into the calibration constants. Khoo et al. (1996) successfully used a similar approach in a variable height channel (1.6 - 16.6 mm). They inserted their sensor from the bottom of the channel, such that the prongs were the only parts that were exposed to the air flow. They then soldered a bent U-shaped hot-wire onto the prongs in an effort to minimize any flow interference. However, their approach required a complex mounting arrangement for the sensor, and an elaborate soldering technique (see Chew et al., 1998b for details on the construction of the sensor) which makes it impractical to use within notebook computers. What is required for this research is a hot-wire or hot-film sensor mounted flush with the wall of interest. Such sensors can easily be inserted from the bottom surface of channels and their construction makes them essentially non-intrusive to the flow. The remainder of this literature review is dedicated to the discussion of such sensors.

1.3.3.2.2 Hot-film Anemometry Techniques

The most common technique for measuring the *mean* wall-shear stress is flush-mounted hot-film anemometry (Brunn, 1995). Although this technique can also be used to measure the fluctuating wall-shear stress, it has a very limited frequency response, as will be explained later. Its operating principles are very similar to those of hot-wire anemometry. The main differences is that the hot-wire is replaced with a thin film deposited onto a low conductivity substrate (generally quartz). The theory behind this technique was developed by Liepmann & Skinner (1954), Bellhouse & Shultz (1966), and Menendez & Ramaprian (1985), and is based on the

steady-state analytical solution for a heated surface exposed to a flow with a linear velocity profile. The theory is valid under the (reasonable) assumption that the thermal boundary layer over the thin-film sensor is well within the viscous sublayer for the flow of interest. The resulting analysis gives the following relationship between the sensor voltage and the wall-shear stress:

$$E^2 = A + B{\tau_w}^{1/3}, \tag{1.3}$$

where A and B are calibration constants. One of the main limitations of hot-film anemometry is the poor frequency response of the sensor, which is directly related to conduction losses to the substrate (Alfredsson & Johansson, 1988). To further understand this phenomenon, suppose that a hot-film sensor is operated by a CTA and allowed to reach steady state. For all flow rates, the temperature of the hot-film will be the same (due to the electronics of the CTA). However, the temperature of the substrate will vary because the convective heat transfer from the substrate to the flow depends on the flow rate. This will cause the temperature field in the vicinity of the hot-film to vary and affect the output of the CTA. The time it takes for the entire system to reach a thermal steady-state is limited by the (relatively massive) thermal inertia of the substrate itself. This is not an issue when the sensor is being calibrated statically, because sufficiently long waiting periods occur between each calibration point. Furthermore, this is also not an issue when the sensor is being used to measure the mean value of the fluctuating wall-shear stress, because the sampling time required to obtain a statistically converged quantity is generally longer than the time it takes for the system to reach steady-state. However, this becomes a serious issue when a time-series of a fluctuating wall-shear stress is to be obtained, as the thermal inertia of the substrate will delay the response of the CTA to changes in wall-shear stress. This phenomenon is called amplitude attenuation and i) is the principle cause for the sensor's inadequate response, and ii) is directly related to the reason why these sensors measure an erroneously low value for the turbulence intensity[4], (η), defined here as the ratio of the root-mean-square value of the wall-shear-stress fluctuations (τ_{rms}) to the mean wall-shear stress (τ_{avg}).

[4] A good way to test the frequency response of a wall-shear-stress sensor is to measure the wall-shear-stress intensity in a turbulent channel flow, and compare it to the generally accepted value for this quantity, which is approximately 0.4. If the sensor has an insufficient response, then it will be insensitive to rapid wall-shear-stress fluctuation and will measure an erroneously low value of τ_{rms}, thus causing η to be lower than 0.4. A large range of values of η (0.05–0.24) have been obtained in the literature when this quantity was measured using hot-film sensors in gaseous flows (Eckelmann, 1977; Chambers et al., 1982; Madavan et al., 1985).

The previously-described problem can be solved by minimizing the conductive heat transfer to the substrate and/or by maximizing the convective heat-transfer to the flow. Many such solutions have been proposed in the literature, and some are presented here. One approach involves the use of liquids, which have higher thermal conductivities than gases, resulting in improved convective heat transfer in liquids as compared to gases. Therefore, in experiments performed with liquids, the response of hot-film sensors is better than that in experiments done with gases (Eckelmann, 1974; Madavan et al., 1985; Alfredsson & Johansson, 1988; He et al., 2011). However, it is not always possible to switch from a gas to a liquid in an experiment.

In their attempts to reduce the conduction to the substrate, Cook & Giddings (1988) and Shah & Antonia (1987) mounted a hot-wire flush with the substrate instead of a hot-film. Chew et al. (1998a) also constructed a similar sensor and compared its dynamic response with a standard hot-film sensor. The hot-wire had a surface contact area much smaller than the hot-film, which reduced the conduction to the substrate and improved the frequency response, which remained nevertheless unacceptably low. Aoyagi et al. (1986) embedded a hot-film sensor within a substrate and mounted another hot-film sensor on top. The embedded sensor acted as a "heat guard" to keep the substrate temperature relatively constant. This lowered the effects of conduction and improved the correspondence between static calibration and dynamic measurements. Alfredsson et al. (1988), Wagner (1991), Nagano & Tsuji (1994), Chew et al. (1994), and Fernholz & Warnack (1998), used a hot-wire sensor that was mounted a few wire diameters above the substrate (called a wall- or marginally-elevated hot-wire). Doing so considerably reduced the heat conduction to the substrate and improved the sensor's response. Khoo et al. (1998a) tested the dynamic response of such a sensor using a specially designed rig, and determined that it was suitable for the measurement of the fluctuating wall-shear stress in a turbulent flow. They also obtained some rather contradictory results and showed that parameters leading to enhanced conduction to the substrate, such as increased substrate thermal conductivity and hot-wire diameter, improved the response. Cook (1994), Spazzini et al. (1999), and Sturzebecher (2001), mounted a hot-wire flush with a substrate into which was machined as small cavity located beneath the hot-wire (cavity-hot-wire). This technique eliminated any prong interference with the flow, considerably reduced the heat conduction to the substrate, and improved the sensor's response. A double hot-wire version of this sensor was developed by Spazzini et al. (1999) and, using a special calibration procedure, allowed the direction of the

wall-shear stress to also be measured. This sensor was then used by Spazzini et al. (2001) to analyse the unsteady behaviour upstream of a backward-facing step, similar to the work involved in this thesis.

Several other wall-shear-stress measurement techniques exist, such as flash photolysis (Popovich, 1969), electro-chemical methods (Kamalesh et al., 1970), and pulsed-wire anemometry (Castro, 1992). They have, however, never really gained much popularity due to the complexities involved in their implementation. Therefore, they will not be discussed further in this review.

Finally, there has been a great deal of interest in the development of micro-machined sensors within the last decade (Löfdahl & Gad-el-Hak, 1999). These sensors solve many of the issues involved with the previously listed techniques, and they are expected to become more popular in the near future. However, they remain expensive to produce.

Based on all the wall-shear-stress sensors described in the above literature review, it was decided that the cavity-hot-wire sensor held the most promise for the present research. The novel wall-shear-stress sensor that was developed and used in this work is based on this design. It will be discussed in detail in Chapter 4.

1.4 Organization of the Thesis

The background and motivation as well as the goals and specific objectives of this thesis were presented in sections 1.1 and 1.2. The remainder of Chapter 1 was dedicated to a literature review on the following subjects: notebook cooling, flows over and in the vicinity of blockages, and wall-shear stress measurement techniques. In Chapter 2, all aspects of the experimental facility will be presented and explained. In Chapter 3, the flow measurements systems used in this work will be presented and discussed. In Chapter 4, the design, construction, operation, and validation of the novel wall-shear-stress sensor will be discussed. In Chapter 5, the results and discussion will be presented. Finally, in Chapter 6, the contributions of this work will be summarized and suggestions for improvements and future work will be presented.

Chapter 2

Experimental Apparatus and Techniques

The specific objectives of this thesis include the design and fabrication of a mini-channel with flow characteristics similar to those encountered within notebook computers. Such a channel was constructed, and all the necessary equipment required to operate it was installed. This entire system is shown in figure 2.1 and will be referred to as the channel facility herein. The different components of this facility are discussed from its upstream- to downstream-ends. They consist of: i) variable-height mini-channel; ii) transition box and laminar flow elements (LFEs); iii) flow-rate control valves; iv) commercial air-flow meter; and (v) blower.

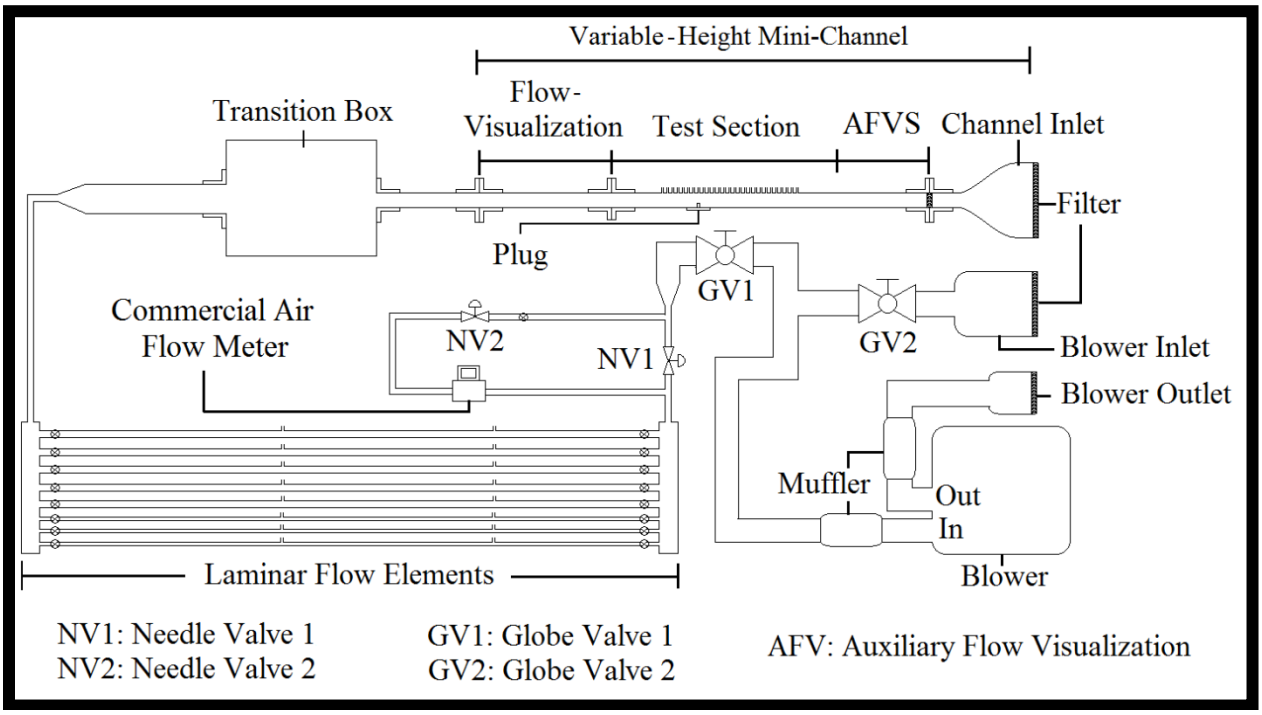

Figure 2.1 - Schematic of experimental facility

2.1 Variable-Height Mini-Channel

The mini-channel shown in figure 2.1 is composed of an inlet, auxiliary flow-visualization section (AFVS), test section (TS), and flow-visualization section (FVS). The gap or channel height (a) of the entire mini-channel, except for the inlet, can be changed to 1, 2, 3 or 4

mm. However, only the 2 and 4 mm gap heights were investigated in this thesis. In this section of the thesis, the inlet and AFVS are first described. The components and operational aspects of the TS are then explained in detail, followed by the procedure used to seal the mini-channel. The FVS was used by another master's student, who performed temperature measurements on the surface of various heated partial blockages using liquid crystal thermography. Since these thermal aspects were not part of this thesis, no further discussion on the FVS will be provided.

2.1.1 Inlet and Auxiliary Flow-Visualization Section

A converging inlet was designed and attached to the upstream-end of the mini-channel. A relative humidity sensor (Vaisala HMP60) was purchased and installed next to its entrance to assess the influence of the relative humidity on the wall-shear stress. The operating instructions for this sensor are provided in Appendix A. Because the flows investigated in this thesis were laminar and fully-developed (upstream of the partial blockages), flow conditioning was not required, and the design of the inlet simply focused on smoothly feeding the air to the TS. Two filters were fitted to the inlet: one at its entrance and another at its exit. Both filters, which were sandwiched between two wire-mesh screens, prevented dust particles from entering the mini-channel. The exit of the converging inlet section was connected to the upstream-end of the AFVS, which was used in previous experiments (Samuel, 2009), in which the uniformity of a particle packed bed of spheres needed to be inspected upstream of the TS. The AFVS was not used in this thesis, but remained integrated into the mini-channel as it could be needed in future work.

2.1.2 Test Section

Both the calibration of the wall-shear-stress sensor and the wall-shear-stress measurements downstream of the blockages were conducted in the TS. A plug (shown in figure 2.1) was designed and inserted through its bottom surface. It held the sensor in place during both the calibration procedures and the experiments. More details on the insertion of the sensor into this plug are provided in Chapter 4. The TS also contained taps that were used to measure the wall-static-pressure distribution, upstream, over, and downstream of the blockages. The wall-

static-pressure distributions upstream of the blockages also provided an independent means of measuring the flow rate in the TS.

In this subsection, the geometric parameters of the TS are first defined, and the procedure for modifying the channel height is explained. A description of the wall-static-pressure taps is then provided and followed by a summary of the techniques used to position the blockages at different locations upstream of the sensor.

2.1.2.1 Geometric Considerations

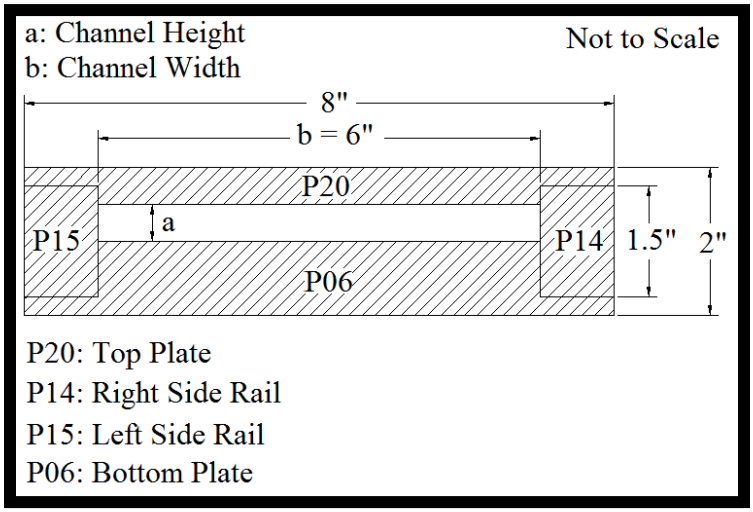

Figure 2.2 - Cross-section of the test section

A schematic of the TS cross-section is shown in figure 2.2. The gap height (a) is determined by the respective dimensions of the four parts shown in this figure. Details pertaining to the assembly of these parts and how they can be arranged to achieve four different channel heights (1, 2, 3, 4 mm) are provided in section 2.1.2.2. This figure also shows that the width or spanwise extent (b) of the channel has a fixed value of 6 in. (152.4 mm).

The top plate shown in figure 2.2 (part P20) is 5 ft (1524 mm) long and was manufactured and used by McBrien (1986). It was constructed from a half-inch thick aluminum plate and 221 equally-spaced wall-static-pressure taps were inserted along its length (streamwise direction) on its top surface (see section 2.1.2.3 for details on these taps). The left and right side rails (part P15, and P14, respectively) were machined out of a 1 in (25.4 mm) wide, 1.5 in. (38.1 mm) thick, and 12 ft (3.8576 m) long aluminum bar that was cut in half. Machining these two rails out of the same bar improved their dimensional similarity. Furthermore, these two rails were

purposely designed to be long so as to extend through the AFVS, TS, and FVS. This arrangement ensured a good alignment and consistent channel height between these sections. The last part shown in figure 2.2 is the bottom plate (part P06). Four versions of this part with different thicknesses were manufactured out of a 1.5 in. (38.1 mm) Delrin sheet. Since all other parts in figure 2.2 have fixed dimensions, the overall channel height was controlled by the thickness of the bottom plate.

A three-inch (76.2 mm) diameter hole was machined through the four bottom plates at a distance of 2 ft (609.6 mm) from their upstream-end. Four identical flanged plugs were machined out of a 5 in. (127 mm) Teflon rod and pushed through these holes until their respective flanges met with the bottom surfaces of the bottom plates. An O-ring grove was machined on each of the plug flanges and an O-ring (Seal Science AS568-152) was placed inside the groove. The plugs were then secured to the bottom surface of the bottom plate by means of four machine screws. This procedure prevented any air leakage between the two parts. The plugs were initially machined with an overall thickness that was slightly larger than the largest thickness of the bottom plates. Therefore, they initially protruded out from the three inch holes by a small amount. Once fitted and secured, the top (or wetted) surfaces (exposed to the air flow) of both the plug and bottom plates were given a final smooth cut together on a milling machine, such that any misalignment between the two parts was removed. Finally, a 0.25 in. (6.35 mm) hole was reamed through the center of the plug, through which the wall-shear-stress sensor was inserted. The final assembly of one of the bottom plates and plugs is shown in figure 2.3.

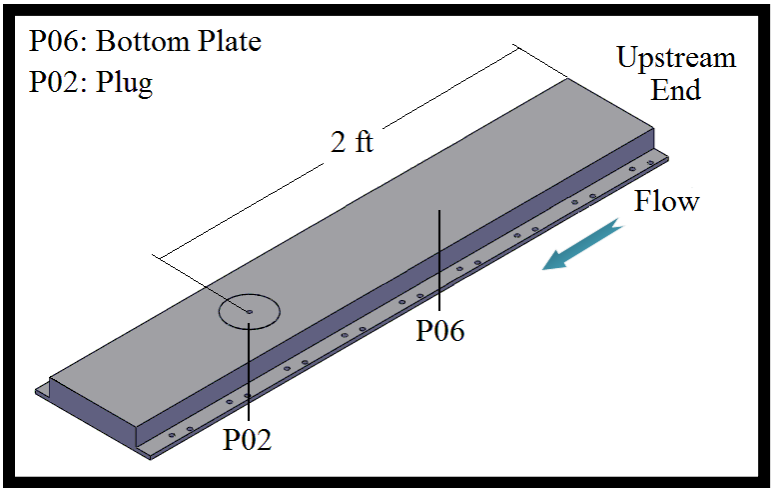

Figure 2.3 – Bottom plate and plug assembly

In summary, it was ensured that the wetted surface of the TS was free of any imperfections and/or discontinuities, so that the channel height in the TS was as consistent as possible, and air leakage into the TS was essentially eliminated. These factors affect the accuracy of the measurements, as will be explained in Chapter 3.

2.1.2.2 Assembly and Height Adjustment

The variable height mini-channel was designed to allow four different channel heights (1, 2, 3, or 4 mm). The procedure required to modify this height is provided here. Figure 2.4 depicts the following: A) the assembled channel inlet, AFVS, TS, and FVS; and, B) an exploded view of this assembly. This figure also shows that the assembly is composed of a top, middle, and bottom layer. Four versions of all the parts shown in the middle layer (P09, P10, P11, P12, and P13), except for the two side rails (P06 and P14), were machined with different thickness dimensions. The same was done for the test section bottom plate (P06) and plug (P02), as was explained in section 2.1.2.1. The four different versions of these seven parts will be denoted as subparts from now on. The modification of the channel height is achieved by replacing the correct subpart inside the channel. Table 2.1 is a reference for selecting the correct subpart for the desired channel height. This table also contains the abbreviated name of these subparts, which is written on the actual parts themselves.

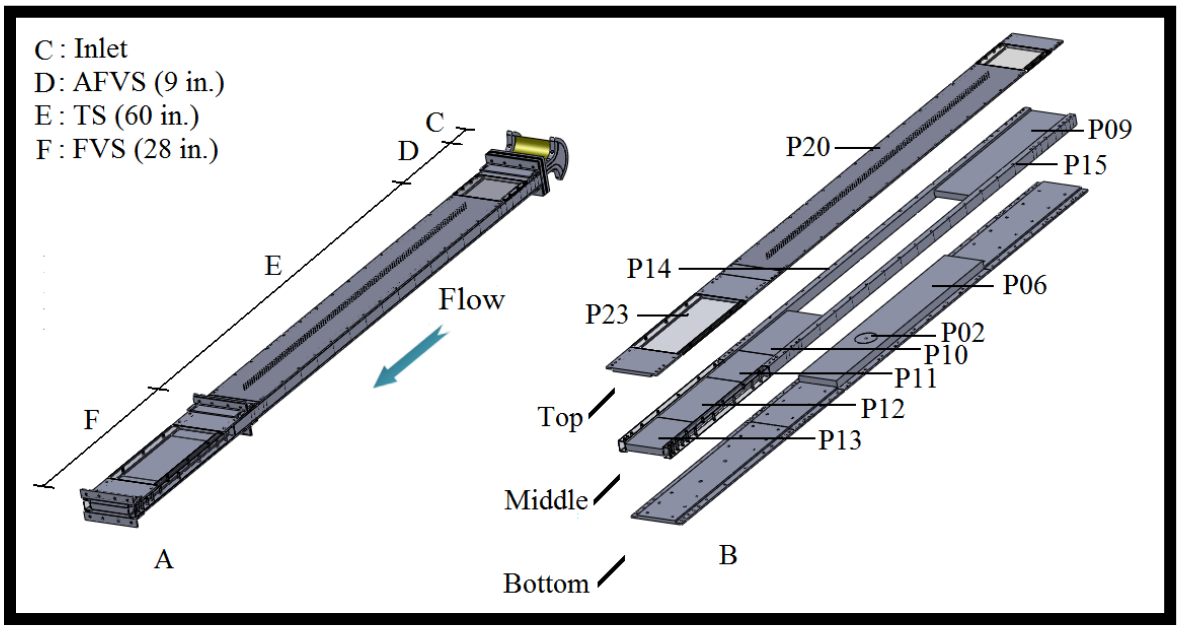

Figure 2.4 - A) Inlet, AFVS, TS, and FVS assembly; B) exploded view

Part Number in Fig. 2.3	Abbreviated Subpart Name and Corresponding Channel Height			
	1 mm	2 mm	3 mm	4 mm
02	TSP28	TSP29	TSP30	TSP31
06	TSP10	TSP16	TSP19	TSP22
09	TSP08	TSP14	TSP17	TSP20
10	TSP09	TSP15	TSP18	TSP21
12	FVP07	FVP11	FVP13	FVP15
11 & 13	FVP08	FVP12	FVP14	FVP16

Table 2.1 - Correspondence between abbreviated part name and channel height

The correct procedure for replacing the subparts described in the previous paragraph is outlined here. The first step is to remove the test section top plate (part P20), the flow visualization central top plate (part P23), and the test section bottom plate (part P06) and corresponding plug (part P02). Once this is done, the parts in the middle layer, except for the two side rails, can be removed and replaced with the desired subpart, as given in Table 2.1. Once replaced, the desired test section bottom plate and corresponding plug can be reassembled, followed by the two parts removed in the first step.

2.1.2.3 Details of Wall-Static-Pressure Taps

As previously mentioned, the top plate of the test section included 221 wall-static-pressure taps. The latter consisted of brass tubes with an outer and inner diameter of 1/16 in. (1.6 mm) and 1/32 in. (0.8 mm), respectively. However, the actual holes in the TS that connected these taps to the bottom surface of the top plate were 0.5 mm in diameter. These holes were purposely drilled very small to minimize the disturbance caused by them on the wall-static-pressure measurements. An elaborate and ingenious machining procedure, explained in McBrien (1986), had to be undertaken to machine and fit these taps into the test section. The taps were numbered from 1 to 221 with 1 being closest to the inlet (upstream-end). The nominal distance between successive taps was 1/4 in (6.35 mm). However, for increased accuracy, the precise distance separating the taps was recorded during the machining procedure. The data set containing the pressure tap numbers, as well as their respective distances away from the upstream-end of the test section, is provided in Appendix B.

As previously mentioned, the wall-static-pressure taps are used to determine the pressure distribution in the TS. Given that multiple pressure drop measurements along the length of the channel were required, a differential pressure transducer (Datametrics, model 590-D-1kPa-2Q8-V1X-4D), and a mechanical multiplexer (Scanivalve model # 48D9) with a solenoid drive and controller (Scanivalve model # CTLR10(P)/S2-26) were used. The multiplexer, allowed one of 48-low pressure lines and one high-pressure line to be linked from the test-section-wall-static-pressure taps to the pressure transducer. All pressure lines were composed of 1/16 in. vinyl tubing (Scanivalve model # Vinl-063). The solenoid drive controller was connected to a data acquisition and control unit (HP 3497A), which was linked to a computer using an HPIB cable. This enabled the switching of the 48 low-pressure lines to be controlled using a LabVIEW program that was created (and named "Scanivalve Controller").

2.1.2.4 Blockage Insertion and Adjustments

The wall-shear-stress sensor was calibrated in the TS described in the previous subsections. However, the ultimate goal of this work is to measure the wall-shear stress behind partial blockages. Consequently, blockages needed to be added to the TS at different locations upstream of the sensor. These blockages consisted of 6 in. long and 1 in. and 0.755 in. wide, precision-ground flat bars with different thicknesses (thickness tolerance of ± 0.001 in.). The procedure required to position these blockages will be explained here.

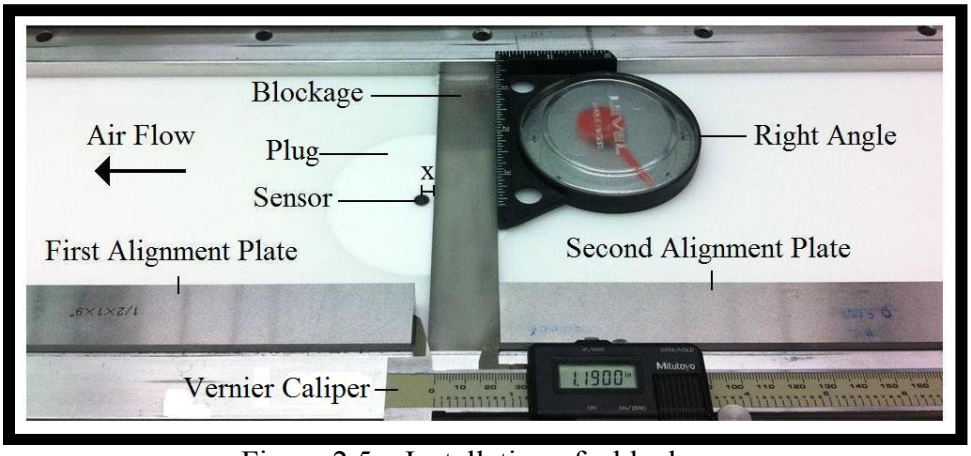

Figure 2.5 – Installation of a blockage

Figure 2.5 is a picture of the TS with the top plate removed. The positioning of the blockage was done using a Vernier calliper, a right angle, and two precision-ground alignment

plates. The first alignment plate was slid along the left side rail (P15 in figure 2.2) until it contacted a piece of electrical tape that was placed on the rail and aligned with the center of the hole on the plug, through which the sensor was inserted. A Vernier calliper was then placed with one of its jaws parallel to the upstream-end of the first alignment plate. The second jaw was then moved upstream to a distance corresponding to the desired location of the downstream-end of the blockage (X) plus the width of the blockage, and then locked into place. Then the downstream-end of the second alignment plate was placed parallel with the upstream jaw of the Vernier calliper. Finally, the upstream-edge of the blockage was placed parallel with the downstream-end of the second alignment plate, and squareness was ensured using a right angle. Before, removing all the positioning tools, the blockage was secured to the bottom surface of the test section by applying a small amount of hot glue (from a glue gun) to its four corners. A small amount of glue was also applied on the top of the blockage, along the two sides in contact with the left and right side rails. This glue ensured that the blockage was held down when the top plate was reinstalled and secured. It was essential, as it prevented blockage vibrations, which would otherwise lead to erroneous wall-shear-stress measurements. However, after having measured the wall-shear-stress downstream of the 60% and 80% blockages (see chapter 5), it was realised that an excessive amount of glue placed on top of the blockage could potentially increase the channel height in the vicinity of the blockage. Since the gap above the 60% blockage was larger than the gap above the 80% blockage, a larger amount of glue was applied to the 60% blockage to ensure that it was held down firmly. This caused the wall-shear-stress measurements obtained using the 60% blockage to be non-repeatable. Therefore, these measurements were repeated using a different technique for securing the blockage to the channel. This technique consisted of placing a ¾ in. wide strip of double-coated tape (3M 667C) along the entire bottom length of the blockage before placing it in the channel. Since repeatable results were obtained using this technique, the 40% blockage measurements of wall-shear stress were also performed using the double-coated tape.

2.1.3 Sealing

The air through the entire channel facility was driven by a blower in suction mode, which caused the absolute pressure of the air inside the mini-channel, LFE, and connecting ducts to be lower than the atmospheric pressure in the lab. Consequently, any small gaps in the channel

facility caused air to leak into it. This was a serious issue because the LFE (one of the flow measurements systems) was mounted downstream of the mini-channel, which meant that it would i) overestimate the mass flow rate inside the TS if any leaks were present between the TS and the LFEs, and ii) result in an inaccurate calibration of the wall-shear-stress sensor. To minimize the air leakage, a procedure was developed to seal the channel (and test how well it was sealed).

All the gaps, bolts, nuts, connection points, and contact areas between parts were sealed using removable caulking[5]. The only contact area in the channel facility that was not sealed with removable caulking was between the TS top plate (P20) and the left and right side rails (P15 and P14 respectively). The reason for this was that the top plate needed to be removed frequently, during the insertion and positioning of the blockages, which rendered the use of removable caulking impractical. Instead, these parts were sealed using electrical tape, which can be easily removed and reapplied without leaving any residue. The electrical tape worked very well for these parts because, when assembled, their adjoining surfaces have metal-to-metal contact. Finally, standard 1/4 in. bonded washers were used on the bolts that secured the top plate to the side rails and bottom plate. These washers contained a thin rubber gasket, which prevented air leakage through the threads of the bolts and removed the need to caulk them.

Once the channel facility was sealed, it was tested for leaks. This was done by first conducting a "vacuum test," which involved blocking the air inlet of the mini-channel, using layers of Saran Wrap, and opening all the valves connecting it to the blower. With this setup, the blower lowered the pressure inside the channel facility to a value significantly lower than the room air pressure. Consequently, if any air leakage did occur, it was amplified to a point where a hissing sound could be heard at the corresponding leakage locations. These locations were then resealed using suitable amounts of removable caulking. Once all such hissing sounds were removed, a more elaborate leakage test was performed after having removed the Saran Wrap.

Before describing the second more-elaborate leakage test, it is important to note that the air leakage is minimized at the smaller flow rates. This is because the corresponding overall pressure drops in the channel facility, and hence the difference between the absolute room pressure in the lab and that within the channel facility, decrease with decreasing flow rate. The

[5] The best technique for using removable caulking is to apply a generous amount on the surface of interest, wait five minutes, and then spread it out in a convex manner. Once applied, it takes about 12 hours to solidify.

second leakage test first compared the lowest possible mass flow rates that could be measured by the LFEs, and the corresponding ones deduced using the pressure distribution obtained with the test-section-wall-static-pressure taps. Theoretically, the two sets of the mass flow rates should be identical. However, experimental uncertainty and air leakage inevitably caused them to be different. If the difference between these flow rates was greater than 3%, the above-mentioned vacuum test was repeated. If this difference was less than 3%, the same comparison was made at higher flow rates. If the percent error remained the same at the higher flow rates, then it was concluded that the channel was well-sealed. If not, the above-mentioned vacuum test was repeated, once again.

2.2 Transition Box and Laminar Flow Elements

As can be seen in figure 2.1, a box-like structure, labelled the transition box, was included in the flow circuit downstream of the variable-height mini-channel. This box was used in the past as a device that allowed appropriate transition for the rectangular cross-section of the TS to the circular cross-section of a flow-measurement tube. In this flow-measurement tube, a traversing pitot tube and wall-static-pressure taps were located, and the related measurements were made to calculate the flow rate. More details on the operating principles of this flow-measurement system are provided in McBrien (1986). Unfortunately, this flow-measurement system was not suitable for the relatively low overall flow rates investigated in this thesis. For this reason, another flow-measurement system (consisting of the LFEs) was constructed in collaboration with another master's student (James Medvescek), and incorporated into the facility. This new system was connected to the mini-channel using the same transition box and circular flow-measurement tube, with some small modifications. The operating principle of the LFEs is based on the analytical relationship between the mass flow rate of a fully-developed laminar flow in a tube of circular cross-section and the corresponding pressure drop per unit length.

The LFEs consist of two eight-port manifolds connected by eight stainless-steel seamless tubes of circular cross-section, as shown in figure 2.1. The first five top tubes and the remaining bottom three tubes have an outer diameter of 1/2 in. and. 3/8 in., respectively. The inner diameters of these tubes (D_i) needed to be accurately determined. To do this, i) the density of the tap water in the lab (ρ_w) was determined by weighing a 250 ml sample (measured in a graduated

cylinder with a volume accuracy of ± 0.02 ml) using a digital scale (Acculab VI-350 with accuracy 0.01g), ii) a segment of one of the tubes was cut (length (L_c) = 1.606 ± 0.002 m), and weighed (m_1) using the same scale, iii) the cut segment was filled with tap water and weighed (m_2), and finally iv) the inner diameter of the tube was calculated using:

$$D_i = \frac{4(m_2 - m_1)}{\pi \rho_w L_c}. \tag{2.1}$$

The resulting inner diameters for the large and small tubes turned out to be exactly the same as the ones provided by the manufacturer (0.402 in., and 0.277 in., respectively). The accuracy of these diameters was calculated based on the general formula for the error propagation of a function q (with variables x_1, x_2, ... , x_n), which is given in Taylor (1997). This formula is shown below for convenience:

$$\frac{\delta q}{q} = \frac{1}{q}\left[\sum_{i=1}^{n}\left(\frac{\partial q}{\partial x_i}\delta x_i\right)^2\right]^{1/2}. \tag{2.2}$$

Using equation 2.2, the accuracy of these diameters was determined to be 0.5%.

Each manifold port contained a check valve, which was used to direct the flow between the eight tubes in two different configurations. A schematic of one of these tubes and its connection to the manifolds is shown in figure 2.6. Each tube contained a pair of 1/16 in. outer diameter pressure taps separated by a distance (L) of 2.075 ± 0.005 m, and the first of these pressure taps was located 2 m downstream of the upstream manifold. These pressure taps were mounted on the LFE tubes using a specially-designed block and Swagelok compression fittings. The pressure-tap pairs were connected to the differential pressure transducer described in section 2.1.2.3, using a series of small manifolds and electronic switching valves. These valves were also connected to the same data acquisition and control unit described earlier, which allowed the pressure drop across any pair of pressure taps to be measured using a specially designed LabVIEW program (named “Pressure Read”). The pressure drop measurements were then used to calculate the total mass flow rate through the entire LFEs, which was also equal to the total mass flow rate inside the TS (assuming there were no air leakages). However, the equations used for this calculation, which will be described in section 3.4.1, are only valid when the flow in each LFE tube is laminar and fully-developed in between the aforementioned pressure-tap pairs.

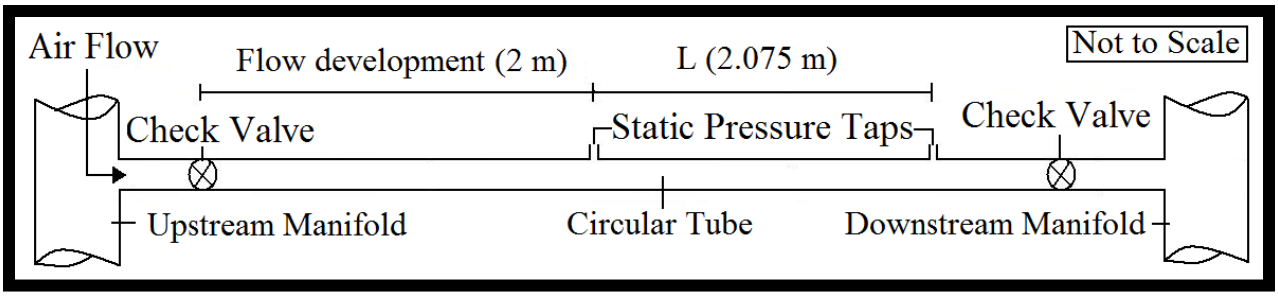

Figure 2.6 – Schematic of one of the LFE tubes

The LFEs were designed to be used in two different configurations. In the first configuration, the flow from the TS is directed through the five larger LFE tubes. In this arrangement, the values of Reynolds number in the TS (Re_{TS}) that can be measured lie in the range 400 – 1000. In the second configuration, the flow from the TS is directed through the three smaller LFE tubes. In this arrangement, the values of Re_{TS} that can be measured lie in the range 50 – 425. The lower-end of these operating ranges is set by the minimum pressure drop that can accurately be measured by the pressure transducer. The upper-end of these operating ranges is set by the maximum value of Reynolds number that ensures the flow is laminar inside each of the LFE tubes (Re_{FE}) (here, it was taken as 2000).

Having explained the two operating ranges of the LFEs, another important issue can now be discussed. The calculation of the flow rate in each LFE tube requires the flow between the pressure taps to be both laminar and fully-developed. Provided that there is no significant air leakage into the mini-channel, and the operating range of the LFE is respected, the flow within the LFE tubes is guaranteed to be laminar, by design. Furthermore, if a sufficiently long development length > $(0.06 \cdot Re_{FE} \cdot D_i)$ is provided upstream of the pair of pressure taps, then the flow is also guaranteed to be fully-developed in that region of interest (Fox, 2006). Using this relation for the worst-case scenario (Re_{FE} = 2000 and D_i = 0.402 in.), the maximum development length required for the LFE was calculated to be 48.24 in. (1.22 m). Therefore, the 2 m development length provided before the pressure drop-measurement section of each LFE tube is sufficiently long for all values of the Reynolds number investigated in this thesis.

2.3 Flow-Rate Control Valves

Once the air exists the LFEs, it encounters four control valves (NV1, NV2, GV1, and GV2), which are shown in figure 2.1. If all these valves are closed, there will be no flow through

the channel. (Any future user of this apparatus should note that the blower will be damaged if these valves are all closed while the blower is running. For this reason, globe valve (GV2), which provides a "clear air" path – independent of the other valves – to the blower inlet, must always remain opened and locked in this position, if possible.) During normal operation (calibration and experiments), globe valve (GV1) is fully opened and the needle valve (NV2) is fully closed. In this arrangement, the flow rate through the test section and laminar flow elements can be fine-tuned by adjusting the needle valve (NV1). When the commercial air-flow meter (discussed in the next section) is being used, GV1 is, once again, fully opened; however, NV1 is fully closed and the flow through the TS and LFE is controlled using NV2.

2.4 Commercial Air Flow Meter

A commercial air-flow meter (Alicat M-100SLPM-D) was purchased and installed in the channel facility, as a check on the two other flow-measurement systems (LFE and test-section-wall-static-pressure taps). The operating range of this flow meter was (0-100) standard litres per minute (SLPM)[6]. It requires a 7-30 VDC input, and it outputs the mass flow rate on an onboard LCD screen in SLPM. It has an accuracy of (0.4% reading + 0.2 % full scale) provided that it has been zeroed before use by cutting off the gas flow to it (closing the check valve immediately downstream of the device), and pressing a button labelled "tare" (which is located on the top right corner of the device).

The operating principles of this commercial air-flow meter are very similar to those of the eight used in the LFE. The only two differences are i) the commercial meter uses hundreds of small-diameter tubes instead of eight, and ii) it only measures the pressure drop across the entire tube bundle rather than across each individual tube. This commercial air-flow meter, also like the LFE, takes into account the temperature and absolute pressure effects on the density and viscosity of the air. The only inconvenience of using this commercial air-flow meter is that the pressure drop across it is quite large (17 kPa at 100 SLPM). The maximum pressure drop across it corresponds to 70% of the total pressure drop that the blower can handle in suction mode. When it was used, the maximum possible Re_{TS} was only 700, which was below the desired Re_{TS}

[6] It should be noted that, technically speaking, litres per minute (LPM) is a unit of volumetric flow rate, but it has become an industry standard to express mass flow rates in terms of standard litres per minute. To obtain the mass flow rate in the correct units the SLPM unit must be multiplied by the density of the gas at the standard conditions used during the calibration of the gas flow meter (25 °C and 1 atm).

= 1000 limit. Nevertheless, it was useful as a check on the previously described methods for calculating the flow rate. Furthermore the LFEs were found to be more accurate than this commercial air-flow meter at the lowest of the flow rates. A more detailed description of this device can be found in its operating manual.

2.5 Blower

The tubing immediately downstream of the control valves was connected to a centrifugal air blower (Regenair R7100A) driven by a 10-horsepower 3-phase AC motor, which was used, in suction mode, to induce flow in the channel facility. This blower is rated at 100 in. of H_2O in blowing mode and 95 in. of H_2O in suction mode. The motor requires a 550 Volt, 3-phase power supply. At this voltage, the rated motor speed is 3450 rpm. However, a 3-phase 600V power supply, which was available in the laboratory, was used to run the motor of the blower. Operating the blower at a slightly higher voltage (than the rated voltage) does not cause any problems. However, there are some crucial steps that need to be followed before powering the blower to avoid damaging it.

As previously mentioned, the blower should never be operated unless globe valve (GV2) is fully opened. Opening this valve provides a "clear path" (free of hydraulic resistance) to the blower inlet. The channel and flow elements provide a significant resistance to the flow, and without this "clear path," the blower would be starved of air and overheat. Furthermore, the blower is contained within a sound-proof box with a built-in convective cooling system (not shown in figure 2.1). Before running the blower, the fan controlling the air flow through the soundproof box (for convective cooling) must be turned “on”. Failure to do so will cause the blower to overheat and the soundproof box could then become a fire hazard.

Once operating, the air leaving the blower will be at a high temperature (≈ 110 °C). This occurs because this type of blower acts like a compressor which raises the absolute pressure of the air leaving it, and consequently raises its temperature. For this reason the outlet air flow was directed outside the lab window, using a thermally-insulated high-temperature-resistant silicone vacuum hose. However, the muffler connected to the outlet is not insulated and should, therefore, never be touched during operation. It is also important to mention that all hose connection points between the channel, blower, and lab window have been fitted with quick-release couplings.

These coupling were installed to facilitate the tasks of disconnecting and moving the blower when needed, and closing the lab window blinds during optical experiments.

As a final note, before starting a calibration or an experiment, the blower should be operated for at least two hours to allow sufficient warm-up time. The temperature of the blower increases gradually during this time, causing the winding resistance inside the motor to increase, and resulting in a loss of motor efficiency. Consequently, the flow rate in the channel will decrease continually until thermal stability is achieved. It is important to note that the motor efficiency is not sensitive to the flow rate in the channel because most of the flow, supplied to the blower inlet, comes from the "clear path." This means that no warm-up type is required when the flow rate in the channel is changed as long as globe valve (GV2) remains in its fully open position. However, as a precaution, every time the flow rate was changed, a 20-second delay was used before any measurements were taken.

Chapter 3

Flow Measurement

In this section, a summary of the three following flow-measurement systems are provided: laminar flow elements (LFEs); test-section-wall-static-pressure taps (TSWSPTs); and a commercial gas-flow meter. The instruments and techniques used to measure the properties of the air and the different pressure drops in the channel facility are then described, and followed by the theoretical aspects of the calculation of the mass flow rates using data obtained from the LFEs and the TSWSPTs.

3.1 Summary of Flow-Measurement Systems

During the design of the present experiment, the possibility that the blockages inserted in the test section (TS) could (erroneously) affect the pressure distribution measured using the TSWSPTs, which would therefore prevent accurate calculation of the corresponding flow rate, was considered. Thus, as an alternative, a new flow-measurement system (based on the LFEs) was designed to provide another means of obtaining the mass flow rate, independent of the TSWSPTs. These two flow-measurement systems were also independently checked against a commercial gas-flow meter. (As was previously mentioned, this commercial gas-flow meter generated a significant amount of hydraulic resistance, which is why it could not be used to cover the entire TS Re range.) Based on these checks, the following conclusions were made: i) the flow rates calculated using the data from the LFE were accurate, provided there was no air leakage in the channel facility, and ii) those calculated using data from the TSWSPTs were also accurate if the channel height used in the calculations was slightly modified from its nominal value. (As will be explained in section 3.5, it was difficult to directly measure this channel height. Instead, an average channel height was inferred from the mass flow rate calculated using the LFE data.) Furthermore, it was determined that if a blockage was inserted in the downstream-end of the TS, then the pressures measured using the TSWSPTs in the upstream-end of the TS were *not* affected by the presence of the blockage, so they could be used to accurately calculate the mass flow rate. Such a situation also prevailed during measurements of the wall-shear stress

downstream of the blockages because i) the plug holding the sensor was located in the downstream-end of the TS, and ii) the blockages were placed very close to the plug, so they did not affect the flow in the upstream-end of the TS. However, during the measurement of the pressure distributions before, over, and after the blockages, they (the blockages) were positioned in the middle of the TS to minimize any possible disturbances caused by the plug holding the shear-stress sensor. Consequently, the LFEs were used to obtain the flow rate in these latter experiments. Lastly, during the calibration of the sensor, the TSWSPTs were used (instead of the LFEs) to minimize any errors cause by air leakages.

3.2 Air Property Measurements

For calculations of mass flow rates using data from the flow-measurement systems described in the previous section, the values of the density and the viscosity of air at different locations in the channel facility were required. These two properties were calculated based on the temperature and absolute pressure of the air at these locations. The determination of the latter two properties will be explained in this section, as well as the techniques used to measure the pressure drops at the different locations in the channel facility. However, before proceeding, it is important to note that all data needed for the flow-measurement and air-property calculations were recorded using the HP 3497A data acquisition and control unit. This unit is powered by a standard 120 VAC supply, has an 8-bit resolution, and a maximum sampling frequency of 13 Hz. Instructions on using its multiple features can be found in its operating manual.

3.2.1 Temperature

The overall experimental facility contained thirteen type-E (chromel–constantan) 30-gauge thermocouples installed at different locations. These thermocouples were used to measure the temperature of the air flow. A schematic showing the locations of 10 of these thermocouples, as well as the abbreviated codes used for reference purposes herein, are shown in figure 3.1. Eight thermocouples (T41-T48) were mounted on the outer wall of each of the LFE tubes at the midpoint between the corresponding pair of pressure taps. One thermocouple (T49) was placed at the inlet of the mini-channel and another (T40) was positioned on the downstream-end of the

TS top plate. The remaining three thermocouples (T50-T52) are not shown in this figure because they were not used in this work.

The thermocouples were fabricated and calibrated in the Heat Transfer Laboratory. A total of 30 calibration points were used over the range of 5 to 62 °C. A least-squares, second-order polynomial was fitted to the calibration data for each thermocouple. The resulting curve-fit constants are provided in Appendix C. A high-precision water bath (Neslab RTE-220) was used for this calibration, and a previously calibrated quartz thermometer (model HP 18111A; accuracy of +/-0.005 ºC) was used as a secondary temperature reference. Thus, it was possible to achieve a thermocouple-calibration accuracy of +/- 0.02 ºC.

All thirteen thermocouples were connected to a connector box, which was linked to the same data acquisition and control unit (HP 3497A) that was previously described. It enabled the voltage output from any of the thirteen thermocouples to be transmitted to a lab computer. A LabVIEW program (named "Temperature Read") was written, tested, and used to convert the average voltage output from each thermocouple to its corresponding temperature. This program also allowed the user to control the number of voltage readings (samples) and the time delay between these readings, required for the calculation of the average. It was found that 25 samples taken at 4 Hz produced average temperature values that were repeatable to within +/- 0.002 ºC, provided that the thermocouples were at steady-state.

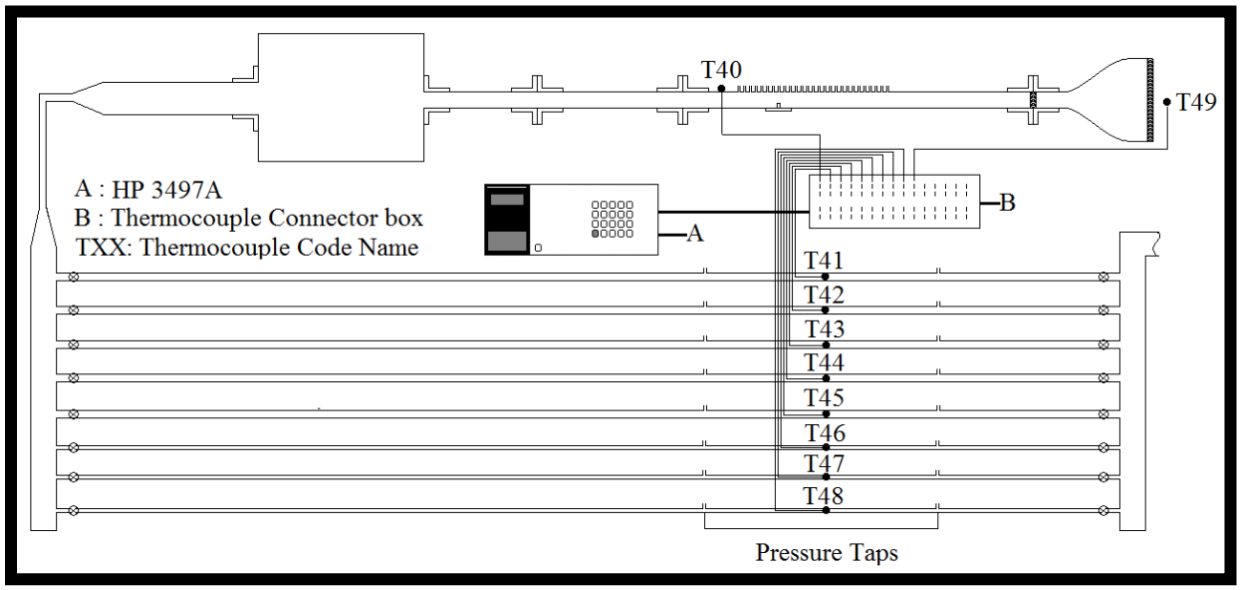

Figure 3.1 - Schematic of thermocouple locations and code names

3.2.2 Absolute Pressure

The absolute pressure of the air was calculated by subtracting the pressure drop in the channel facility (from the inlet of the mini-channel to the location of interest) from the atmospheric pressure (P_{atm}) in the lab. The different pressure drops that were measured are explained in the next section. However, the measurement of P_{atm} is described here. This measurement was obtained using an electronic barometer (Vaisala PTA 427), which was accurate to ± 40 pascals (Pa). This device required a stable 11-30 VDC power supply, and outputted a voltage (V_{out}) of 0-5 VDC. The calibration curve for the barometer is:

$$P_{atm} = 133.367\,[39.3064\,V_{out} + 599.875], \tag{3.1}$$

where P_{atm} is in pascals (Pa) and V_{out} is in volts (V).

3.3 Pressure-Drop Measurements

The pressure-drop measurements required for both the LFEs and the TSWSPTs were made using a temperature-compensated integral Barocel (capacitance type) pressure transducer (Datametrics, Model 590-D-1kPa-2Q8-V1X-4D), with an accuracy of 0.05% of the reading plus 0.01 Pa. This device, which will be denoted as the Barocel herein, was also connected to the HP 3497A data acquisition and control unit. As previously mentioned, the Barocel is a differential pressure transducer, which means it can be used to measure a pressure difference (maximum of 1 kPa for this model). It was powered using a stable, laboratory grade power supply (15-30 VDC), and given a two-hour warm-up time before use. Furthermore, it had to be zeroed about every 30 minutes, even after it had been fully warmed up. The zeroing was achieved by shorting the high- and low-pressure inputs of the Barocel, and rotating a zeroing screw, using a specially mounted screwdriver, until the shorted voltage output (offset), which was displayed on the HP 3497A, was as close to zero as possible (offset < 0.0005 VDC). The measurement of this offset was accomplished by using a specially written LabVIEW software (named "Measure Barocel Offset"), and the offset (in Pa) was obtained by multiplying the voltage by 100. Earlier, it was determined that this conversion from voltage to Pa is valid for the entire voltage output range of the Barocel (0-10 VDC).

Before describing the theoretical aspects of the mass flow rates calculated using data obtained with the two flow-measurement systems, it is important to be familiar with the 12 pressure-drop measurement locations in the overall flow circuit. A schematic showing these locations, as well as the codes used for reference purposes herein, are shown in figure 3.2. An average reading of each of these pressure drops could be obtained using a LabVIEW program that was developed and implemented for this purpose (and named "Pressure Read"). Once again, this program enables the user to select the number of readings to average and the delay time between these readings. Unlike the average temperature, however, with increasing flow rate, a larger number of readings were required to obtain a consistent value of the average pressure drop, and this number also depended on the location of the pressure-drop measurement (figure 3.2). In general, the pressure drops measured in the LFE (P1-P8) required more samples to obtain a consistent average than the pressure drops measured in the test section (P9). However, as a rule of thumb, 200 samples taken at 4 Hz, to suitably account for the worst-case scenario, were used to calculate an average pressure value that was repeatable to about ± 0.3 Pa. It is also important to have a 10-second delay in between the acquisition of successive sets of pressure-drop measurements, to ensure mechanical stability of the Barocel. Lastly, for increased accuracy, it was found necessary to obtain and subtract the Barocel offset from the averaged pressure measurement.

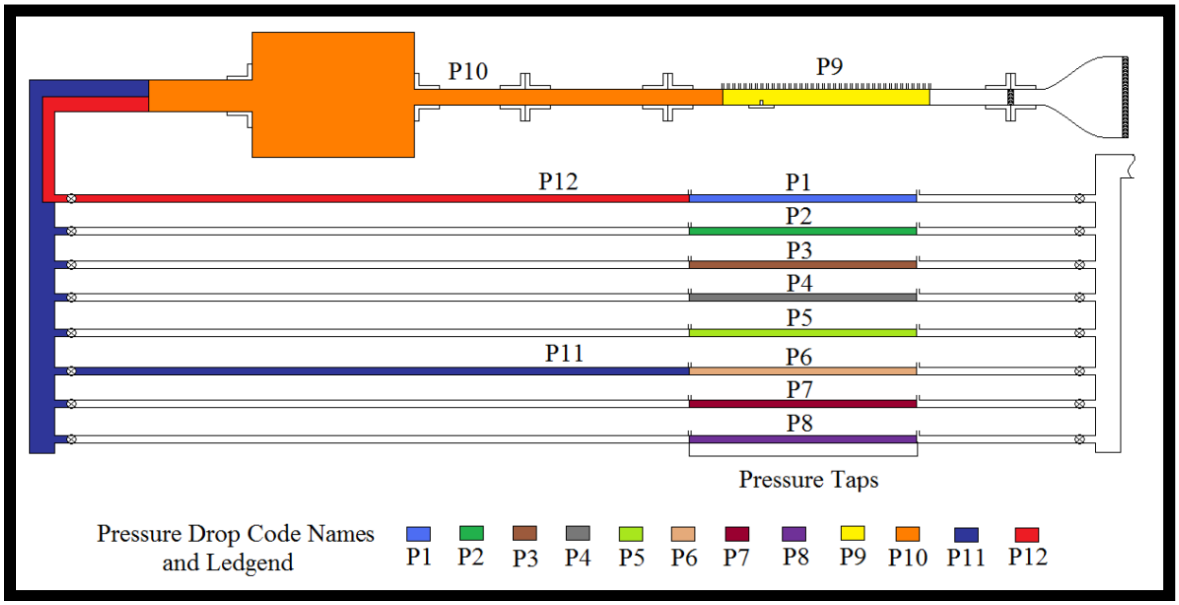

Figure 3.2 – Schematic of pressure-drop-measurement locations and code names

3.4 Flow-Rate Measurements Using Laminar Flow Elements

The equations used to calculate the mass flow rate through the flow circuit, based on the pressure drop data from the LFE, are explained here. The relation between the mass flow rate in one LFE tube (M_{FE}) and the corresponding pressure drop (ΔP_{FE}) across a pair of pressure taps separated by a length (L), was based on the analytical solution of steady, fully-developed laminar flow of a constant-property fluid in a circular tube. This relation is:

$$M_{FE} = \rho \pi D_i^{\,4} \Delta P_{FE} / (128 \mu L), \tag{3.2}$$

where D_i is the inner diameter of the tube, and ρ and μ are the average density and dynamic viscosity of the air, respectively. The total mass flow rate through the test section (M) was calculated by summing the individual mass flow rates obtained from all LFE tubes that were used. The length (L = 2.075 ± 0.005 m), and the inner diameters (D_i = 0.01021 m ± 0.5% or 0.007036 m ± 0.5%, depending on whether the large or small LFE tubes were used, respectively) were constant. On the other hand, ρ is dependent on the average absolute temperature (T_{abs}, in units of kelvin) and absolute pressure (P_{abs}, in units of pascal) of the air. The relation between the absolute temperature and density of the air was obtained by curve-fitting the property data for air provided in Incropera et al. (2007). The relation between the absolute pressure and density of air was obtained from the ideal gas law. The equation resulting from these two relations is:

$$\rho \left[\frac{kg}{m^3}\right] = \frac{P_{abs}}{P_{std}} \left(3.49699 \text{ x } 10^2 \cdot T_{abs}^{\,-1.00064}\right), \tag{3.3}$$

where P_{std} is the standard atmospheric pressure of air (101325 Pa). The absolute air temperature, between each pair of pressure taps, was measured for each tube using the thermocouples located on them (T41-T48 in figure 3.1). The absolute pressure of the air was determined by first calculating the total pressure drop, from the inlet of the mini-channel up to the midpoint between the pair of pressure taps located in the LFE, and then subtracting this value from the atmospheric pressure in the lab (P_{atm}), which was measured using the barometer described in section 3.2.2. This calculation is provided below in terms of the pressure drops shown in figure 3.2.

$$\text{large LFE tubes:} \quad P_{abs} = P_{atm} - (P9 + P10 + P12 + P1/2) \tag{3.4}$$

$$\text{small LFE tubes:} \quad P_{abs} = P_{atm} - (P9 + P10 + P11 + P6/2) \tag{3.5}$$

The final parameter in equation 3.2 is the dynamic viscosity of the air. This quantity is primarily dependent on the temperature of the air. A relation between the dynamic viscosity and the absolute temperature of the air can be obtained by curve-fitting the property data for air in Incropera et al. (2007). The result of such a curve fit is:

$$\mu\left[\frac{\mathrm{kg}}{\mathrm{m}\cdot\mathrm{s}}\right] = C1\cdot T_{abs}{}^{3} + C2\cdot T_{abs}{}^{2} + C3\cdot T_{abs} + C4, \tag{3.6}$$

where C1, C2, C3, and C4 are constants equal to $1.1832\cdot10^{-9}$, $-3.8080\cdot10^{-6}$, $6.7374\cdot10^{-3}$, and $1.3554\cdot10^{-1}$, respectively. The absolute temperature required in the previous equation was measured using the same thermocouples as those used for the density calculation.

Now that all the parameters in equation 3.2 have been discussed, the accuracy of the LFE measurements of mass flow rate, principally dependent upon the accuracies of ΔP_{FE} and D_i, can be calculated. The accuracy of D_i ($\delta D_i/D_i$) was previously determined to be 0.5%. The accuracy of ΔP_{FE} ($\delta\Delta P_{FE}/\Delta P_{FE}$), was determined by dividing the uncertainty in the pressure measurement (± 0.3 Pa) by the ΔP_{FE} that would result at the different mass flow rates investigated. A simplified version of equation 2.2, which is shown below, was then used to calculate the accuracy of the total mass flow rate ($\delta M/M$).

$$\delta M/M = \sqrt{(\delta\Delta P_{FE}/\Delta P_{FE})^2 + 4(\delta D_i/D_i)^2} \tag{3.7}$$

The resulting accuracy in the mass-flow-rate calculations using the LFE data, for both configurations used (see section 2.2), is summarised in Table 3.1.

Re (Test Section)	Mass Flow Rate (x 10^4 kg/s)	Mass-Flow-Rate Accuracy Using 3-Tube Configuration (%)	Mass-Flow-Rate Accuracy Using 5-Tube Configuration (%)
100	1.387	1.6	9.3
200	2.775	1.2	4.7
300	4.162	1.1	3.2
400	5.550	1.0	2.5
500	6.937	NA	2.1
600	8.324		1.8
700	9.712		1.7
900	12.49		1.5

Table 3.1 – Accuracy of the LFE measurements of mass flow rate

Theoretically, if the manifolds used in the LFEs were perfect, the mass flow rate should be evenly distributed to the connected tubes, and, therefore, the total mass flow rate could be calculated by multiplying the mass flow rate in one of the LFE tubes by the total number of tubes used, In reality, however, the mass flow rates within the different LFE tubes differed from each other by up to 2%. However, when the five large tubes were used, the total mass flow rate calculated by summing up the individual ones was consistently within 0.5% of the mass flow rate calculated based on that in the second tube (from the top) multiplied by five. No data was available for recommending such a convenience for the other LFE configuration (three small tubes), as it was rarely used.

3.5 Flow-Rate Measurements Using the Test-Section-Wall-Static-Pressure Taps

The test-section-wall-static-pressure taps (TSWSPTs) were used to determine the pressure gradient ($P_x = dP/dx$) along the length of the TS. Provided that the flow is fully developed in that region, P_x will be constant (Fox, 2006). Once determined, the mass flow rate can be calculated using the analytical solution of steady, fully-developed laminar flow in the straight rectangular test section. The cross-sectional height and width of the test section are denoted by 'a' and 'b', respectively. The final equation relating the mass flow rate (M) to P_x is:

$$M = -\frac{\rho a^3 b W}{\mu} P_x, \tag{3.8}$$

Where W is a dimensionless velocity, which is given by:

$$W = \frac{1}{12} - \frac{8}{\beta}\sum_{n=0}^{\infty} \frac{\tanh(\lambda_n \beta)}{{\lambda_n}^5}, \tag{3.9}$$

where $\lambda_n = (2n+1)\pi$, and $\beta = b/(2a)$. The width of the mini-channel (b) was 6 in. (0.1524 m). The height of the mini-channel (a) was nominally either 1, 2, 3 or 4 mm. The word 'nominally' is used here because the value of 'a' slightly differed from its desired value due to machining tolerances. The exact channel height was nevertheless required because the accuracy of this flow measurement system depends on it. However, direct measurement of the channel height is complicated for three particular reasons. Firstly, the channel height is determined by the

dimensions of the four parts of the test section (TS), shown in figure 2.2, which means that the individual heights of these parts must be measured to calculate it. Secondly, because the pressure gradient is calculated along the length of the TS, this height must be calculated at different streamwise and spanwise locations in the TS, then averaged. Thirdly, the direct measurement of this height is very difficult to do accurately when the TS is fully-assembled. To solve this problem, the average channel height was inferred from the mass flow rates calculated using data from the LFEs and the pressure gradient along the TS. The relation between these two parameters and the channel height can easily be derived by rearranging equation 3.8, and it is valid provided that there is no air leakage between the LFEs and the TS. The channel height was inferred for the entire range of TS Reynolds numbers that were investigated in this thesis [100 – 1000], and the results showed that the nominal 2 and 4 mm channel heights were 2.08 ± 0.02 mm and 3.97 ± 0.03 mm, respectively. Since the 1 and 3 mm channel heights were not used in this work, their corresponding inferred heights were not determined.

With the above-mentioned inferred channel heights, there remained three quantities that needed to be measured to calculate the mass flow rate using equation 3.8. These quantities were P_x, and the average density and dynamic viscosity of the air in the TS. The pressure gradient (P_x) was obtained by measuring the pressure distribution using 10 of the TSWSPTs, fitting a least-squares straight line to this data, and then determining the slope of this line. However, the flow in the region used to measure this distribution had to be fully-developed. Fortunately, this was not an issue, because the mini-channel has a small hydraulic diameter, which meant that the actual length of the developing region was much smaller than the total length of the TS over the full range of Re investigated in this work.

The density and viscosity of the air in the region of interest were calculated using equations 3.3 and 3.6, respectively. The average absolute temperature required in these equations were obtained using the arithmetic-mean of the temperatures measured by the thermocouples (T40 and T49), shown in figure 3.1. The average absolute pressure, which is also required in these equations, was calculated using:

$$P_{abs} = P_{atm} - P9/2, \tag{3.10}$$

where P9 is the pressure drop across the entire test section shown in figure 3.2. Now that all the parameters in equation 3.8 have been discussed, the accuracy of the TSWSPT measurements of

mass flow rate can be calculated. This accuracy was found to depend mostly on the accuracies of the channel height and the largest TS pressure drop (ΔP_{TS}) used in the measurement of the pressure gradient. The accuracy of the channel height ($\delta a/a$) was previously determined to be approximately 1%. The accuracy of the largest TS pressure drop ($\delta\Delta P_{TS}/\Delta P_{TS}$), was determined by dividing the uncertainty in the pressure measurement (± 0.3 Pa) by ΔP_{TS} for different mass-flow rates and for different distances (L_{TS}) between the pressure taps used to measure ΔP_{TS}. A simplified version of equation 2.2, which is shown below, was used to calculate the accuracy of the total mass flow rate ($\delta M/M$).

$$\delta M/M = \sqrt{(\delta\Delta P_{TS}/\Delta P_{TS})^2 + 3(\delta a/a)^2} \tag{3.11}$$

The resulting accuracies for the 2 and 4 mm height (nominal) channels are provided in Tables 3.2 and 3.3, respectively, for different values of L_{TS} and test-section Reynolds numbers.

Re (Test Section)	Mass Flow Rate (x 10^4 kg/s)	Mass-Flow-Rate Accuracy (%)				
		L_{TS} = 0.2 m	L_{TS} = 0.3 m	L_{TS} = 0.4 m	L_{TS} = 0.5 m	L_{TS} = 1.0 m
100	1.387	7.5	5.1	4.0	3.4	2.2
300	4.162	2.9	2.3	2.1	1.9	1.7
400	5.550	2.5	2.1	1.9	1.8	1.7
500	6.937	2.2	1.9	1.8	1.8	1.7
600	8.324	2.1	1.9	1.8	1.7	1.7
700	9.712	2.0	1.8	1.7	1.7	1.7
900	12.49	1.9	1.8	1.7	1.7	1.7

Table 3.2 – Accuracy of the TSWSPT mass-flow-rate calculation at different L_{TS} (2 mm channel)

Re (Test Section)	Mass Flow Rate (x 10^4 kg/s)	Mass-Flow-Rate Accuracy (%)				
		L_{TS} = 0.2 m	L_{TS} = 0.3 m	L_{TS} = 0.4 m	L_{TS} = 0.5 m	L_{TS} = 1.0 m
100	1.387	58.2	38.8	29.1	23.3	11.7
300	4.162	19.4	13.0	9.8	7.9	4.1
400	5.550	14.6	9.8	7.4	6.0	3.2
500	6.937	11.7	7.9	6.0	4.8	2.7
600	8.324	9.8	6.6	5.0	4.1	2.3
700	9.712	8.4	5.7	4.4	3.6	2.1
900	12.49	6.6	4.5	3.5	2.9	1.8

Table 3.3 – Accuracy of the TSWSPT mass-flow-rate calculation at different L_{TS} (4 mm channel)

By comparing Tables 3.1 and 3.2, it can be seen that for a TS Reynolds number ranging between 100 and 400, the best accuracy in the calculation of the mass flow rate is achieved using the 3-tube configuration of the LFEs. For the larger TS Reynolds numbers (400-900), the 5-tube configuration of the LFEs is slightly more accurate than the TSWSPTs (with the 2 mm channel height). Based on these results, it was decided that the TSWSPTs (with $L_s > 0.3$) should be used for the 2 mm channel height (nominal), even though they yielded mass flow rates that were a bit less accurate than those obtained with the LFEs, because this removed i) any leakage issues, and ii) the necessity of using two different LFE configuration modes to cover the entire range of Reynolds numbers investigated. However, Table 3.3 shows that the accuracy of the TSWSPTs is very bad when the channel height is 4 mm (nominal). Therefore, for this channel height, the LFEs were used instead of the TSWSPTs.

Chapter 4

Shear-Stress Sensor: Design, Construction, Operation, and Validation

The design of the wall-shear-stress sensor was based on the cavity-hot-wire construction (Spazzini et al., 1999), which will be subsequently herein referred to as Spazzini's sensor. As discussed in Chapter 1, a cavity-hot-wire consists of a hot-wire mounted flush with a substrate, with a cavity machined under it (the wire). The cavity reduces heat conduction to the substrate and increases the sensor's frequency response. Spazzini's design consisted of mounting two 5 μm diameter hot-wires separated by 0.25 mm, over a 1 mm deep and 1 mm diameter circular cavity. The sensor used in this work consisted of a single 2.5 μm diameter wire, mounted over a 0.1 mm deep and 1 mm wide rectangular cavity that traversed the entire 0.25 in. diameter of the body of the sensor.

In this chapter, details of the procedure used in the construction of the wall-shear-stress sensor will be first provided. It will be followed by a description of the sensor's operating principles and techniques. Finally, the validation of the sensor will be discussed.

4.1 Design and Construction

The construction of the wall-shear-stress sensor was accomplished in two main steps. First, the different components of the sensor's body were manufactured and assembled. Then, a hot-wire was soldered to the prongs of the sensor. These two main steps are outlined in this section.

4.1.1 Sensor Body

To understand the different steps in the construction of the sensor's body, it is important to become familiar with its different parts. Figure 4.1 is a schematic (not to scale) of the sensor's assembly (A) and the exploded view of this assembly (B). The sensor has a total of six parts: two prongs, the upper body, the lower body, the outer casing, and the hot-wire. In this subsection,

descriptions of these parts, with the exception of the hot-wire, are first provided. They are followed by a description of the technique used to measure the electrical resistance of the prongs. Finally, the assembly procedure is described.

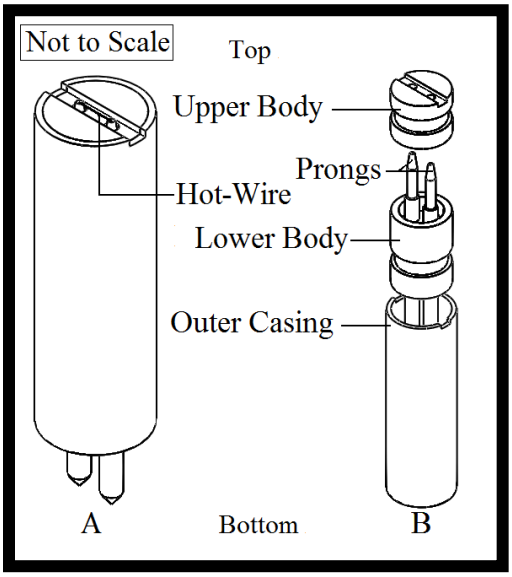

Figure 4.1- Sensor parts: A) assembly; B) exploded view

4.1.1.1 Prongs

The prongs were made up of two subparts: the upper and lower prongs. The assembly of these subparts is shown in figure 4.2, from which it can be seen that the upper prongs are inserted into the lower prongs. The tops of the upper prongs were connected to the hot-wire and the bottoms of the lower prongs were designed to connect to a standard TSI probe support (TSI 1150-18), which provides the link between the sensor and anemometer.

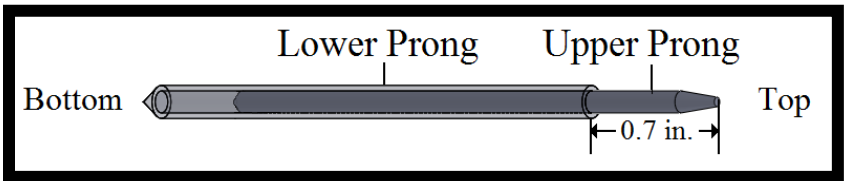

Figure 4.2 - Prong assembly

4.1.1.1.1 Upper Prong

The upper prongs were constructed using two size 12 Lance beading needles made of nickel-plated steel. These needles had a diameter and length of 0.0140 in. and 2.0 in., respectively, and were purchased from a hobby shop called Bead Box. These needles had to be

modified to accommodate the hot-wire and lower prongs. The steps required for this modification are provided below.

Step 1: One of the needles was clamped in a vice with its eye sticking out, as shown in figure 4.3. A protective rubber sheet was inserted between the vice jaws to avoid damaging the needle. The eye of the needle was then removed using a rotary cutting tool (Dremel). During the cut, a low rotary speed was used to avoid burning the nickel coating on the needle.

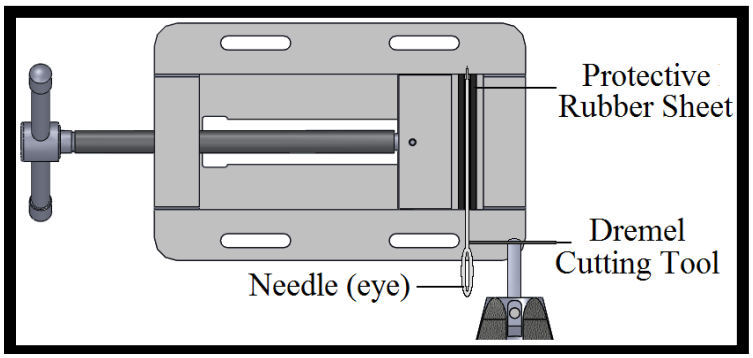

Figure 4.3 – Removal of the eye of the needle

Step 2: The end of the needle, which was cut in step 1 (bottom end), was sharpened to facilitate its insertion into the lower prong. The sharpening was achieved by first clamping the Dremel vertically, such that its blade was horizontal, then setting its rotary speed to high, and finally rotating the bottom end of the needle against the blade, as shown in figure 4.4.

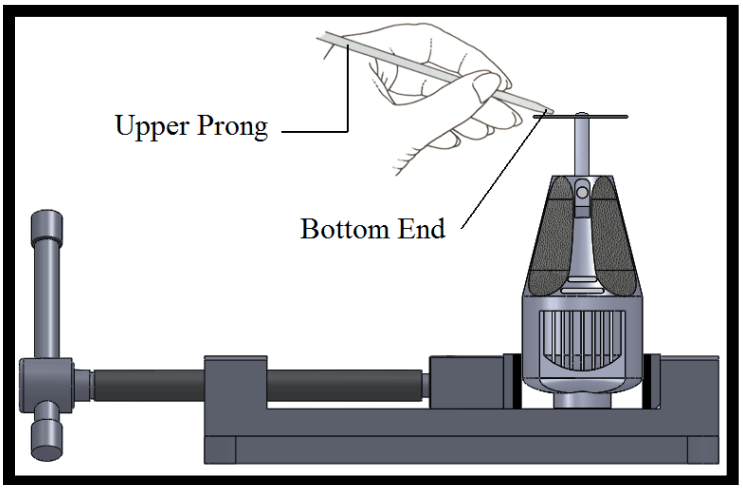

Figure 4.4 – Sharpening of the bottom end of the upper prongs

Step 3: The top end of the upper prong needed to be flattened out to provide a surface for soldering the hot-wire. This was accomplished by placing the needle horizontally on the bottom surface of a vice, with its top end sticking out from the side of the vice. A 0.020 in. gauge block

was then placed flush against this side of the vice, and a precision ground flat bar was used to push the top end of the needle flush against it. The needle was then clamped firmly in place, and the slab and flat bar were removed. At this point, the top end of the needle was sticking out from the side of the vice by exactly 0.020 in.. The top end was then sanded down using 400 grit sandpaper until it was completely flush with the side of the vice. It was then sanded down again using a wet 600 grit-sand paper. This procedure resulted in a flat and smooth top end with a consistent diameter.

Step 4: As was previously explained, the upper prong had to be eventually inserted into the lower prongs. However, after the completion of the three steps described above, it would not be able to fit because of burrs formed when cutting the lower prongs. To solve this problem, the diameter of the upper prong was turned down a small amount. This was accomplished by first clamping the top end of the upper prong about a half inch inside the chuck of a small drill press, then setting the drilling speed to high and squeezing the needle with 400 grit sandpaper, while rotating. The amount of pressure and duration of the squeeze was determined by trial and error, and was applied so that the end of the upper prong would fit snugly into the lower prong. Once this was accomplished, steps 1 to 4 were repeated for the remaining upper prong.

4.1.1.1.2 Lower Prong

The lower prongs were constructed using 24 gauge, 304 stainless steel, thin-walled hypodermic tubes with outer and inner diameters of 0.0220 in. and 0.0141 in., respectively. They were purchased from a company called smallparts.com. These tubes were first cut into 2.5 in. long pieces using a similar cutting procedure as that described in step 1 of section 4.1.1.1.1. To remove the burrs created during this cut, the lower prongs were individually placed in a vice with one of their ends sticking out by a small amount. This end was faced off by moving the rotary blade of the Dremel towards it, as shown in figure 4.5. This end is designated as the top end of the lower prong herein; the bottom end of the upper prong is inserted in this end. The other ends of the lower prongs were then cut and sharpened, such that their tip-to-tip length measured 1.25 in. These ends were sharpened to facilitate their insertion into the TSI support column. This procedure was similar to the one used in step 2 of section 4.1.1.1.1.

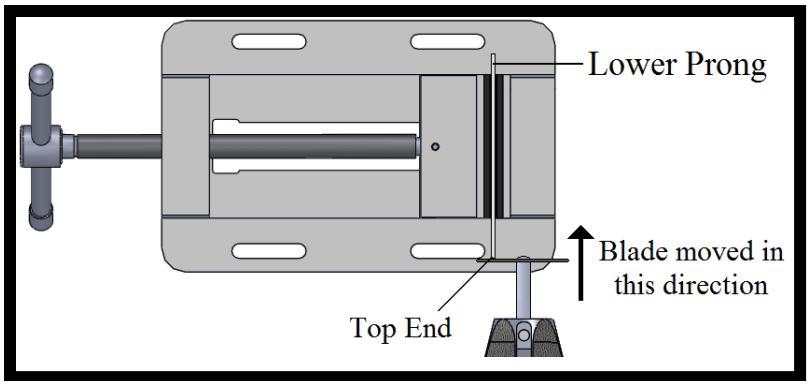

Figure 4.5 – Facing off of the top end of the lower prong

4.1.1.1.3 Assembly of Upper and Lower Prongs

Once the lower and upper prongs were completed, they were assembled together and secured. To do so, the lower prongs were first clamped individually in a vice with their top ends sticking out. The bottom ends of the upper prongs were then pushed through the top ends of the lower prongs until they extended a distance of 0.7 in. from the top ends of the lower prongs, as shown in figure 4.2. Once assembled, the top ends of the lower prongs were individually clamped in one of the top corners of a vice, as shown in figure 4.6. The vice clamp was then tightened as much as possible, which crimped the connection between the lower and upper prongs. This securing technique finalizes the construction of the prongs.

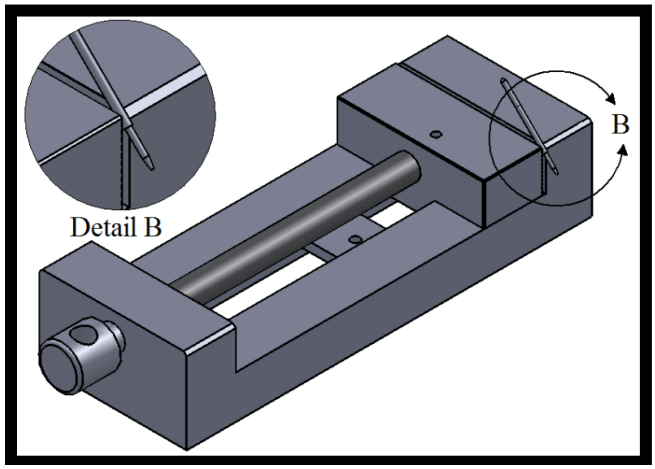

Figure 4.6 – Crimping of the upper and lower prongs

4.1.1.2 Upper Body

The upper body is the part of the sensor that contains the cavity and determines the distance between the top ends of the prongs (1.25 mm). This distance also determines the length of the hot-wire, which is mounted flush against the top surfaces of the prongs and the upper body. Therefore, it is important for this part to be constructed using a material with i) a high maximum operating temperature, to ensure that it does not melt when the hot-wire is operated, and ii) a low thermal conductivity to minimize the heat conducted to it from the hot-wire. Furthermore, it must have a high dielectric strength to prevent the prongs from being shorted, and a thermal coefficient of expansion similar to the outer casing of the sensor, to ensure that the two parts expand at a similar rate when heated. A material that meets these considerations was found and purchased from a company called Crystex composites. This material is a Glass-Mica composite, purchased as a 1/4 in. diameter rod (MM 400). The relevant properties of this material are provided in Table 4.1, and the detailed drawings for this part can be found in figure D.1 of Appendix D.

Max. continuous operating temperature	400 °C
Thermal conductivity	0.87 W/m·K
Dielectric strength	28.7 kV/mm
Thermal expansion coefficient	12.5×10^{-6}

Table 4.1 – Properties of Glass-Mica composite (MM 400)

4.1.1.3 Lower Body

For convenience, the lower body was constructed using the same material as the upper body. As was mentioned in section 4.1.1.2, the upper body separated the top ends of the prongs by a fixed distance. Similarly, the lower body separated the bottom ends of the prongs by a fixed distance (1.7 mm). This was required to ensure a proper connection between the bottom end of the prongs and a TSI support column. The detailed drawings for the lower body are provided in figure D.2 of Appendix D.

4.1.1.4 Outer Casing

The outer casing was constructed using a seamless stainless steel tube with outer and inner diameters of 0.0250 and 0.210 in., respectively. This tube was purchased from a company

called New England Small Tubes. The purpose of the outer casing was to house and protect the upper and lower bodies. It also provided a smooth outer surface, which was important for the insertion of the sensor into the test section (TS), through a teflon plug inserted into and fixed to the bottom surface of the TS. Detailed drawings for the outer casing are provided in figure D.3 of Appendix D.

4.1.1.5 Prong Electrical Resistance

Before assembling and using epoxy on the different parts that were described above, the electrical resistance of the prongs, denoted by R_{pr}, had to be determined. The discussions in the following paragraphs describe i) why this resistance must be obtained prior to assembly and ii) the technique used to determine it.

It is often desirable to operate the sensor using a precise overheat ratio (α). This is especially useful when compensating for a drift in ambient temperature of the room air, as will be explained in section 4.2.5. The setting of α requires the precise value of the electrical resistance of the hot-wire (R_a) to be known at the ambient temperature. However, it is nearly impossible to measure this resistance directly, which means that it must be inferred from R_{pr}. The measurement of the latter resistance requires the top ends of the prongs to be shorted, as will be explained in the next paragraph. However, since these ends are mounted flush with the top of the upper body, it would be almost impossible to short them, which is why R_{pr} must be determined before the sensor parts are glued together.

The prong resistance was determined by first assembling the different parts of the sensor, except for the prongs themselves, without the use of any epoxy, as shown in figure 4.1. The top ends of the prongs were then pushed through the lower and upper bodies of the sensor, such that they protruded from the top end of the upper body by approximately 0.25 in. A shorting probe, shown in figure 4.7 A), was manufactured out of a small copper rod, with two very small holes, separated by a distance of 1.25 mm, drilled on one of the rod's flat ends. These holes where designed to fit snugly onto the top ends of the prongs, such that when fitted, a short-circuit would be produced between them. The shorting probe was inserted on the ends of the prongs, and pushed against the top surface of the upper body of the sensor. The bottom ends of the lower prongs were then connected to a TSI support column, which was connected to a multimeter (Agilent 34401A**)** using a BNC cable. The entire resistance of this circuit (R_{tot1}) was measured.

This resistance included the resistance of the BNC cable (R_{cable}), the resistance of the TSI support column (R_{column}), the contact resistance between the bottom end of the lower prongs and the TSI support column ($R_{contact}$), the prong resistance (R_{pr}), and finally the resistance of the short, which was negligible. The sensor was then removed, and a TSI shorting probe, shown in figure 4.7 B), was used to short the TSI support column. The resistance of this circuit was then measured (R_{tot2}), which included R_{cable}, R_{column}, and $R_{contact}$. The desired prong resistance was then calculated by subtracting R_{tot2} from R_{tot1}.

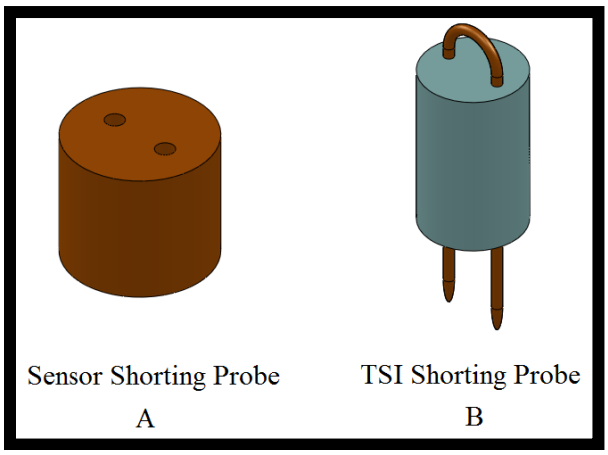

Figure 4.7 – Shorting probes: A) sensor; B) TSI

4.1.1.6 Assembly

Once the electrical resistance of the prongs was determined, the five parts that composed the body of the sensor were secured using a low-electrical- and low-thermal-conductivity epoxy (EE 4525), purchased from a company called Cotronics. The epoxy was injected into the different parts of the sensor using a syringe with a 20 gauge tip. The procedure for gluing these parts together follows.

The prongs were inserted through the small holes in the upper and lower bodies. Epoxy was then injected through the larger holes located on the bottom end of the upper body and the top and bottom ends of the lower body. The bottom end of the lower body was then pushed down through the top end of the outer casing until the circular groove located on its outer surface was positioned slightly above the top surface of this casing. Epoxy was injected into the aforementioned circular groove, and the lower body was pushed further into the outer casing until the circular groove located on the upper body was positioned slightly above the top surface

of this casing. Epoxy was, once again, injected into this groove and the upper body was pushed down until its top surface was protruding out of the outer casing by a small amount. At this point, the upper body was rotated about is axis, such that the straight rectangular cavity on its top surface was lined up with the small notches located on the top surface of the outer casing. All excess epoxy residues were cleaned and the entire sensor was turned upside down and pushed against a precision ground flat bar until the top end of the upper body was completely flush against the bar. The bottom ends of the lower prongs were also pushed down to ensure that they too were flush with this bar. The sensor was kept in this position for 24 hours, which allowed the epoxy to fully cure. After curing, the sensor body was complete and ready for the attachment of the hot-wire.

4.1.2 Hot-Wire Attachment

The list of equipment required to attach the hot-wire to the prongs is provided below:

- Stereo microscope (minimum of 60 X) and flexible LED lamp
- Soldering iron with pointy tip and station
- Glue gun (low temperature), sharp cutting blade, and tweezers
- Leaded solder (63/37, 0.81 mm) and acid flux (Decapant 817)
- Cotton plugs, rubbing alcohol, toothpicks, 400 grit sand paper
- 2 wire holders, 2 wire-holder supports, and wire-transfer-block (figure 4.8)
- 3-axis micromanipulator and base.
- 2.5 micron Tungsten hot-wire bobbin

The attachment of the hot-wire to the prongs was done in three main steps. The hot-wire was first transferred onto a micromanipulator. The micromanipulator was then used to position the hot-wire on top of the prongs, and, finally, the hot-wire was soldered to the prongs. These three steps are discussed below.

4.1.2.1 Transferring to Micromanipulator

The hot-wire was purchased from a company called Auspex Scientific (AMP-TWB-10A). It consisted of a 2.5 μm diameter wire (about 40 times smaller than the average human

hair) and came in a spool, which contained 10 feet of the material. Because of its small diameter, the wire was very difficult to see and needed to be manipulated delicately. The hot-wire was first transferred onto a temporary location, a Wire Holder (WH), which was designed to fit onto a micromanipulator. The hardware required to transfer the hot-wire to the WH was designed and constructed, with the exception of the hot-wire spool, and is shown in figure 4.8. This hardware consisted of a wire transfer block (WTB), two WHs, two wire-holder supports (WHSs). As indicated in this figure, the WH placed inside the slot in the WTB is designated as primary, and the other one, lying beside the WTB, is designated as secondary. Furthermore, this figure shows that each WH contains two pins.

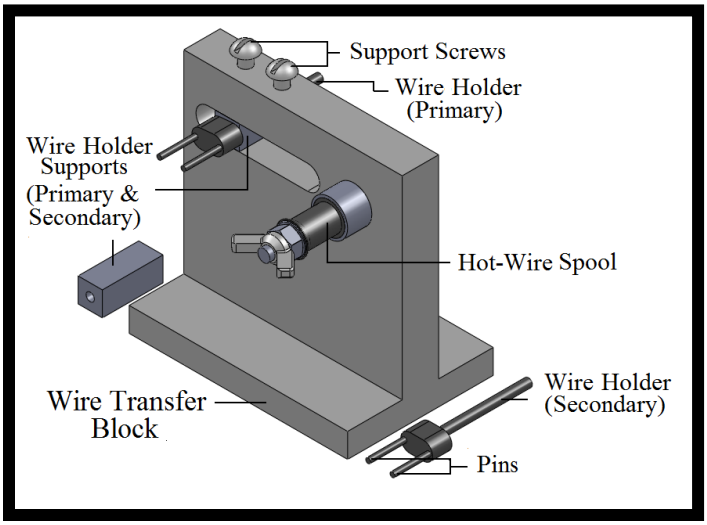

Figure 4.8 – Wire transfer block and wire-holder transfer hardware

Although not shown in figure 4.8, the hot-wire was extended from the spool to the two primary WH pins and secured on these pins, using a small amount of glue from a glue gun. The hot-wire was always maintained taut, and it was connected to something, because if it was let loose, it could unwind from the spool. However, the primary WH had to be eventually removed from the WTB and placed on the micromanipulator. Thus, a second WH (secondary) was required. The steps used to properly remove the primary WH are illustrated in figure 4.9 and explained below.

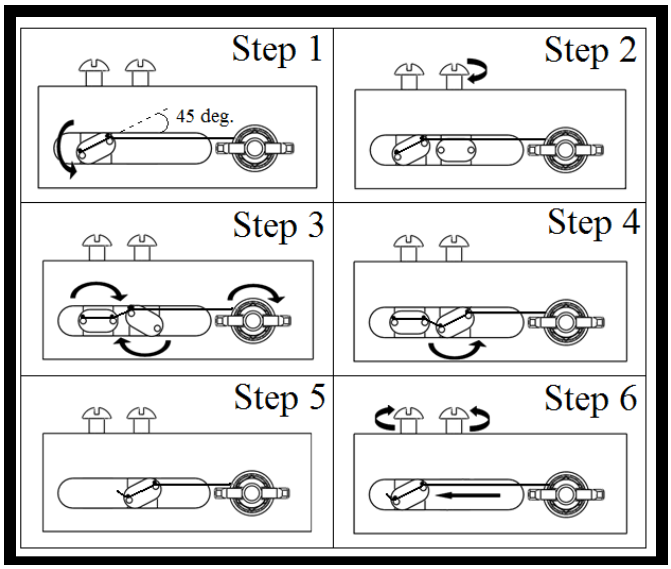

Figure 4.9 – Primary wire holder removal steps

Step1: The primary WH was rotated counter-clockwise (CCW), such that the primary WH pins formed a 45-degree angle with the horizontal.

Step 2: The secondary WH was inserted into the other WH support, and the two parts were placed in the slot located on the WTB without coming in contact with the extended hot-wire. These two parts were then positioned as close as possible to the primary WH and secured using the support screw above them.

Step 3: The primary WH was rotated clockwise (CW), such that its pins were horizontal. While doing so, the spool was also rotated in the same direction to ensure that the hot-wire was kept taut. The secondary WH was rotated CW by a small amount to ensure that the hot-wire was resting firmly on its left pin (closest to primary WH). A small amount of glue, from a glue gun, was applied on top of this pin to secure the hot-wire at that location.

Step 4: The secondary WH was rotated CCW, such that the hot-wire rested firmly on its right pin. A small amount of glue was applied on top of this pin to secure the hot-wire in that location.

Step 5: The hot-wire segment, which extended between the two wire-holders, was cut using a sharp razor blade. The support screw above the primary WH was loosened and the latter was carefully removed from the WTB.

Step 6: The screw located above the secondary WH was loosened and the latter was dragged to the previous location of the primary WH. The screw above it was tightened thus returning the WTB to its original state before the transfer.

4.1.2.2 Positioning of the Hot-Wire on Top of the Prongs

Once the primary WH was removed, it was placed on a 3-axis micromanipulator, shown in figure 4.10, which was used to position the hot-wire flush and parallel to the top surface of the prongs. This figure also shows the location of the sensor-holder (SH), and the different knobs and screws required for manipulation and securing purposes. The wall-shear-stress sensor was inserted in the SH and secured in place using screw 2 (S2). The three knobs (K2, K1, and K3) were used to translate the hot-wire along the x, y and z axes respectively. The roll of the hot-wire relative to the prongs was adjusted by rotating the WH. The yaw of the hot-wire relative to the prongs was adjusted by rotating the SH and then securing it via screw 1 (S1). Details of the procedure for manipulating the hot-wire, and adjusting the yaw and roll, are concisely described below.

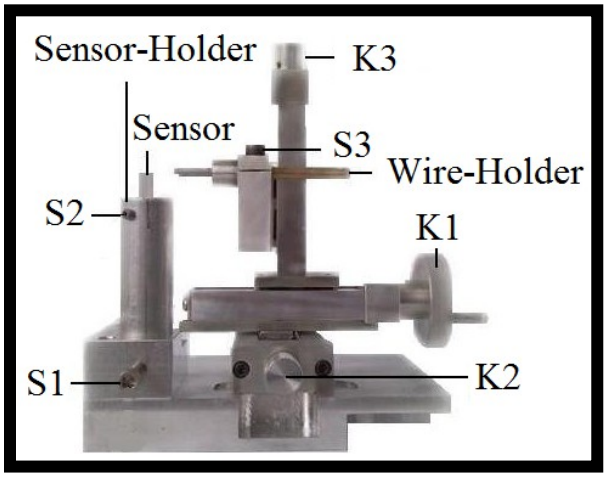

Figure 4.10 – Micromanipulator and mounting base

The micromanipulator was placed under a stereomicroscope (SM), and light from a flexible LED lamp was directed towards the top surface of the sensor, as shown in figure 4.11. Using the three knobs described earlier, the hot-wire was manipulated such that it was positioned approximately over and parallel to the prongs. The focus and zoom of the SM were adjusted such that the flat surface of the prongs clearly spanned the area visible through the eyepiece. The hot-wire was lowered by rotating knob K3 until it appeared just over the prongs. The SH was rotated to remove any parallel misalignment remaining between the prongs and the hot-wire. The SH was locked in place using S1, which completed the yaw adjustment.

The amount of misalignment in the roll of the hot-wire relative to the prongs was determined by the hot-wire's shadow on the prongs. The WH was rotated, until this shadow appeared directly above the center point of the flat surface on top of the prongs. The WH was then locked in place using screw S3, which completed the roll adjustment. Once this was completed, the hot-wire was ready to be soldered.

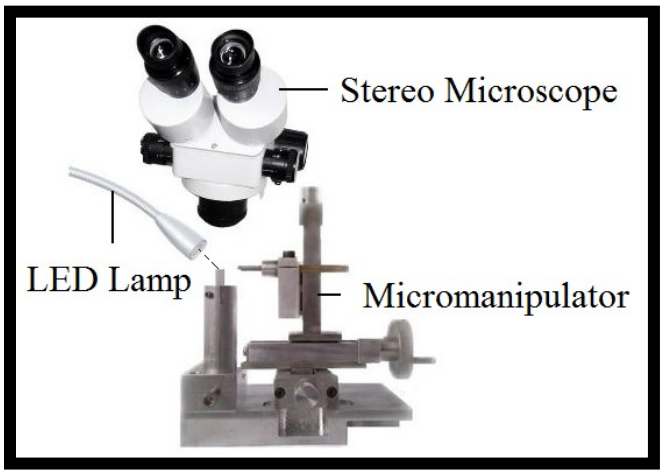

Figure 4.11 – Micromanipulator, LED lamp, and stereo microscope

4.1.2.3 Soldering

A novel soldering technique was required to attach the hot-wire to the prongs. This technique was determined by experimentation and is described here. The soldering iron was first turned "on" and set to a temperature of 350 °C. Once heated, the tip of the iron was cleaned by sanding it with 400 grit sandpaper, and wiped with a wet sponge. The hot-wire was manipulated away from the prongs and a small amount of acid flux (Decapant 817) was applied to the top surface of the prongs using the pointy end of a toothpick. The hot-wire was then placed flush with the center of the prongs, and lowered by rotating knob K3 by a full turn. This created some tension in the hot-wire and resulted in a significantly more stable (repeatable) ambient-temperature-hot-wire resistance (R_a). A small bubble of leaded solder (63/37, 0.81 mm) was applied to the tip of the soldering iron. This bubble was then placed over one of the prongs for a very short period of time (< 1 s), which resulted in some of the solder to transfer and form a much smaller bubble on that prong. The hot-wire was then lowered further by rotating K3 by half a turn and the same soldering procedure was repeated for the other prong. At this point, the hot-wire was fully attached to the prongs. However, before removing the sensor, the hot-wire

had to be detached from the WH. To do this, a razor blade was used to cut the segments of the hot-wire located between the prongs and the WH pins. All remaining hot-wire segments, between the prongs and the outer casing of the sensor, were removed using tweezers. A microscopic view of the sensor after this procedure is shown in figure 4.12. This description of the soldering procedure brings to an end the discussion on the construction of the wall-shear-stress sensor.

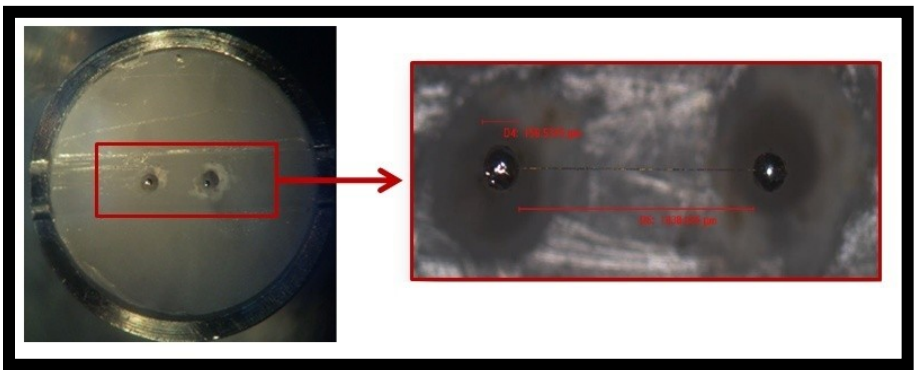

Figure 4.12 – Microscopic view of the sensor with the hot-wire soldered to the prongs

4.2 Operation

The operating guidelines for the use of the wall-shear-stress sensor are provided in this section. The procedure required to insert the sensor in the test section is explained first. Then a description of the techniques used to operate and calibrate the sensor using a constant temperature anemometer (CTA) is presented.

4.2.1 Insertion in Test Section

As was previously mentioned in section 2.2.2.1, the wall-shear-stress sensor is inserted through a plug located in the test section and mounted flush with the bottom surface of the mini-channel. Any offset between the top surface of the sensor and the bottom surface of the mini-channel leads to significant errors, as will be explained in section 4.2.2. Therefore, an elaborate technique, for consistently positioning these two surfaces flush with each other, was developed and is explained here.

A total of four new parts (shaft collar, shaft collar holder, aligning rod, and stopper) were constructed and used to accomplish the task of flush mounting the sensor. These parts are shown

in figure 4.13 along with the top isometric view (A) and bottom isometric view (B) of the test section with the top plate removed. The stopper contained a small 0.15 in. (3.81 mm) hole that was larger than the diameter spanned by the two prongs of the sensor (1.25 mm), yet smaller than the diameter of the outer casing of the sensor (6.35 mm).

The bottom surface of the stopper was placed against the bottom surface of the mini-channel. The alignment rod was then pushed through the hole in the plug and the stopper. This ensured that these holes were perfectly aligned. The stopper was then secured to the two side rails of the mini-channel using four bolts, and the alignment rod was removed. Once removed, the sensor was inserted through the plug and pushed up until its top surface contacted the bottom surface of the stopper. Because the hole in the stopper was larger than the length of the hot-wire, and because the sensor was perfectly aligned with the stopper hole, the delicate hot-wire was not damaged in this step. At this point, the bottom part of the sensor was extending out from the bottom of the plug by about an inch. The shaft collar was then inserted around the sensor, pushed up against the plug, and secured to the sensor's outer casing by tightening its clamping screw. The stopper was then removed and the shaft collar holder was bolted to the plug. The shaft collar holder was designed to push the shaft collar against the plug when it was secured, thus holding the sensor firmly in place. This procedure ensured that the hot-wire was mounted flush with the bottom surface of the mini-channel. Furthermore, the sensor could now be removed and put back at will without having to repeat the entire procedure, provided that the shaft collar was not disconnected from the sensor and that the channel height was not modified.

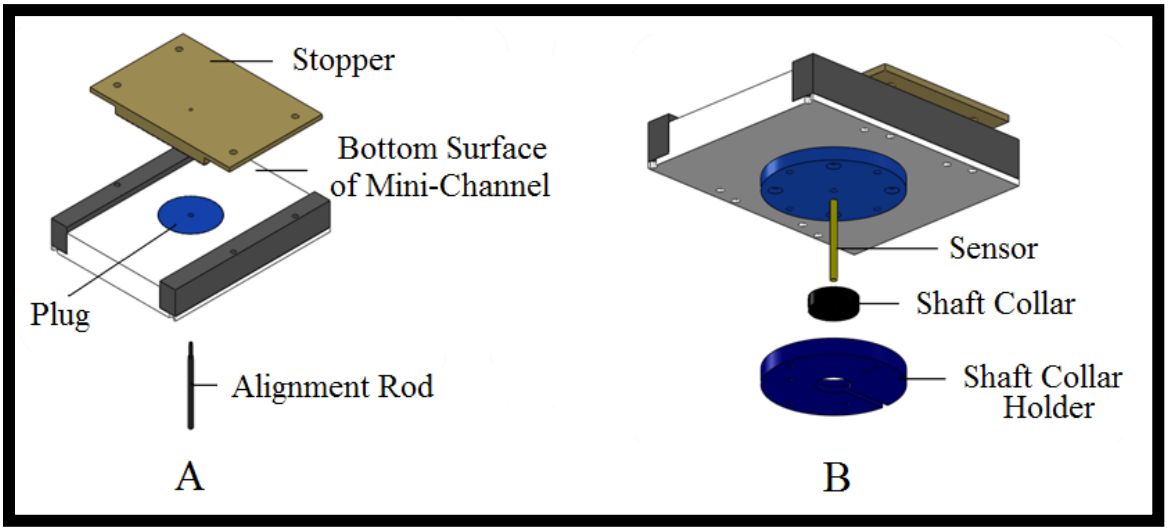

Figure 4.13 – Parts required for flush-mounting the wall-shear-stress sensor

4.2.2 Calibration

Once the sensor was properly flush-mounted with the bottom surface of the test section, it was rotated, such that the hot-wire was perpendicular to the side rails or the main air-flow direction. With the hot-wire aligned in this position, the sensor was now ready to be calibrated, once the ambient-temperature resistance of the hot-wire (R_a) was determined. To measure this quantity, the sensor was connected to the TSI support column (TSI 1150-18), which was connected to a constant-temperature anemometer (CTA; DISA 55M01) using a 5 m BNC cable. The electrical resistance formed by this circuit was measured using the CTA. The TSI support column was then disconnected from the sensor, shorted, and the new circuit resistance was measured and subtracted from the previous one. The prong resistance (R_{pr}) was then subtracted from this result to obtain R_a.

The operating resistance of the hot-wire (R_w) was calculated by multiplying R_a by the desired overheat ratio (α). For most of the calibrations performed and for all of the wall-shear-stress measurements discussed in Chapter 5, an overheat ratio of 1.8 was used to maximize the sensor's sensitivity (Brunn, 1996). The operating resistance was then set on the CTA, and the CTA was set to "run". The output from the CTA was connected to a BNC connector box (NI BNC-2110), which was connected to a 16-bit data acquisition card (NI PCI-6221), which had a maximum sampling frequency of 250 kHz, and variable analog voltage input ranges of ± 1, 2, 5, and 10 VDC. The voltage output from the CTA was recorded using LabVIEW software.

After setting the CTA to "run," the voltage output from the CTA increased rapidly, then decreased with time until it became stable after about 60 s for an α of 1.8. This decay in voltage is attributed to the decrease in heat conducted from the hot-wire to its substrate, after the initial start-up phase. Therefore, the time required for this voltage to stabilize is dependent on parameters that are relevant to conductive heat transfer in the substrate, such as its thermal inertia and the temperature of the hot-wire, which is proportional to α. This time was relatively independent of the flow rate in the test section. Furthermore, once the substrate reached a stable temperature, no major decay in the CTA output was observed when the flow rate was suddenly changed. This finding showed that there was indeed heat conducted to the substrate, and suggested that the substrate's temperature was, at most, only slightly dependent on the flow rate. The latter realization was a good indication that the sensor was suitable for the measurement of a fluctuating flow (see section 1.3.3). Furthermore, it demonstrated that no waiting time was

required between calibration points. With this in mind, the sensor was calibrated in the nominally 2 mm channel (a = 2.08 mm) at different test-section Reynolds numbers ranging from 100 to 2000. For every calibration point, a 20 s delay was provided before measuring the average CTA output, and recording the average wall-shear stress (τ_w). The latter was based on the pressure gradient (P_x) measured by the wall-static pressure taps in the TS, and calculated using:

$$\tau_w = \frac{P_x a}{2}\Omega, \tag{4.1}$$

where, $\Omega\{= 1 - 8\sum_{n=0}^{\infty} 1/{\lambda_n}^2 \cosh(\lambda_n \beta)\}$ is a term that accounts for the channel geometry. This term was neglected because Ω is almost equal to 1 for the wide aspect-ratio of the channel cross-section used in this work.

The average CTA output was calculated using 512 samples recorded at 200 Hz, and the average of each pressure drop required for P_x was calculated using 40 samples recorded at 4 Hz, with a delay time of 5 s between each successive pressure drop measured. It must be noted that fewer samples than the 200 recommended for the pressure drops measurements obtained from the LFE (section 3.2) were used to reduce the total calibration time. However, this did not affect the accuracy because the pressures measured from the wall-static pressure taps were significantly more stable than those measured from the LFE pressure taps. Furthermore, a total of 10 pressure drops were obtained to calculate P_x, which meant that a total of 400 samples were taken and averaged. The resulting TS pressure distributions, for Re = 95.0, 488.1, 987.8, and 1862.8 are shown in figure 4.14, along with the equations of the least square lines used to fit this data. These lines fitted the data very well, which was a good indication that the flow was indeed fully-developed in the region of interest, even at the highest Re of 1862.8. The different pressure gradients, which correspond to the slopes of these lines, can also be observed in this figure.

Once all calibration runs were completed, the square of the CTA voltage output (E^2) was plotted as a function of the wall-shear stress, and the result is shown in figure 4.15. Following the convention for hot-wire anemometry, a King's law calibration curve ($E^2 = A + B{\tau_w}^n$) was fitted to this data: A, B, and n were determined to be 3.06173, 1.6072, and 0.607969, respectively. The correlation coefficient (R-value) of the fit was 0.9998, which indicated that the quality of the curve fit was excellent. This particular calibration curve was used for obtaining some of the wall-shear-stress results discussed in Chapter 5. Brief discussions of the accuracy of the calibration

and the techniques used to compensate for ambient-temperature drifts between calibration and experiment are provided in Appendix E.

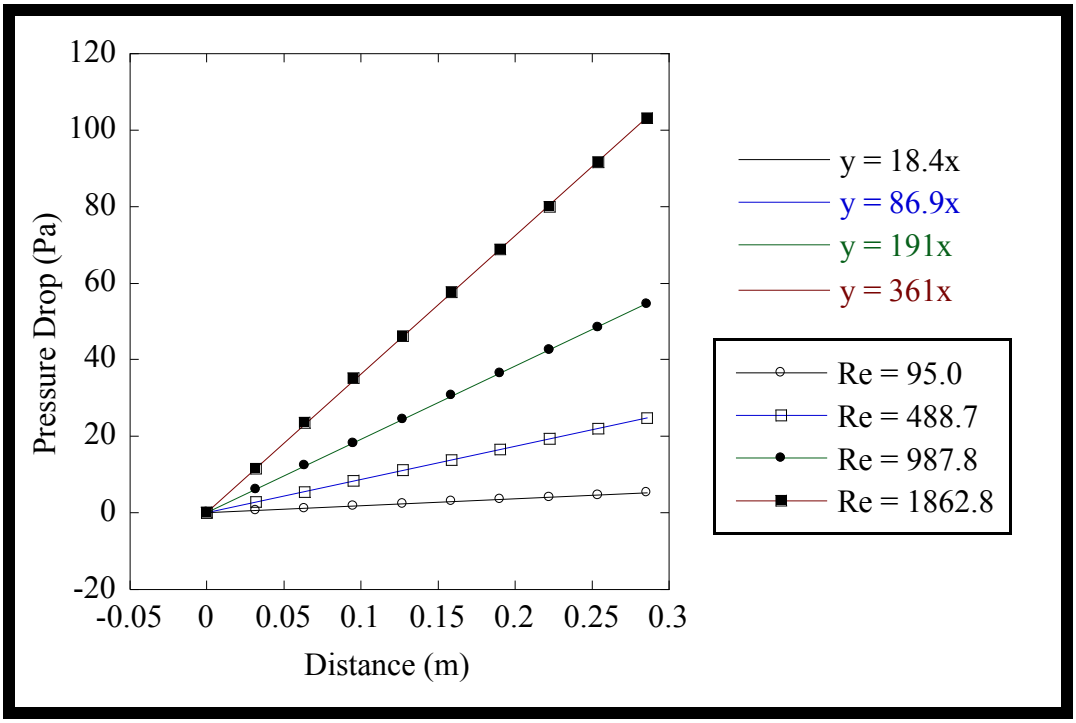

Figure 4.14 – Pressure distribution in the test section (a = 2 mm)

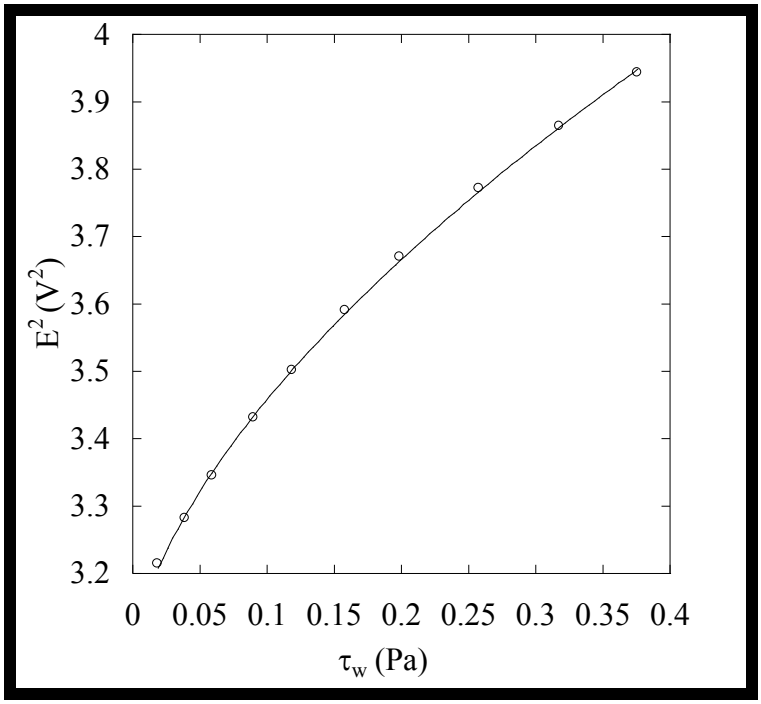

Figure 4.15 – Calibration curve (α = 1.8; a = 2.08 mm)

4.3 Validation of Calibration and Sensitivity Checks

The novel sensor was used to measure the wall-shear stress within the mini-channel described in Chapter 2. However, it was also intended to be used (in the future) for measurements within an actual notebook computer. Thus, it was important to establish various performance characteristics of the sensor, such as its sensitivities to channel height, flow angle, and height offset. The importance of these characteristics and the experiments performed to test them are described in this section.

4.3.1 Validation of Calibration

The mini-channels within notebook computers have non-constant channel heights and could have numerous blockages on both their top and bottom surfaces. Therefore, it was essential that the calibration of the sensor (E^2 vs. τ_w characteristics) be independent of the height of the channel and also the details of the flow above it (the sensor). To test whether this was the case, the sensor was calibrated in the 2 mm and 4 mm channels, and the obtained calibration curves where superimposed. This was done using three different overheat ratios (1.3, 1.5, and 1.8) to determine whether it had any influence on the results. The results, which are presented in figure 4.16, show that the calibration curves obtained at the two different channel heights coincided very well for all three overheat ratios investigated. Moreover, this figure suggests that the results obtained for α = 1.3, were slightly better than those obtained at the higher overheat ratios. Another test was conducted with α = 1.3, 1.5, and, 1.8 in the 2 mm channel but with a slight flush-mounting offset. This latter test also showed better results (less sensitivity to the offset) for the lower overheat ratios. Therefore, the sensitivity of the sensor to both the calibration set-up and also the flush-mounting offset can be reduced by using a lower overheat ratio (at the expense of a lower signal-to-noise ratio). Additional details of the sensitivity of the sensor to flush-mounting offset are provided later in subsection 4.3.3.

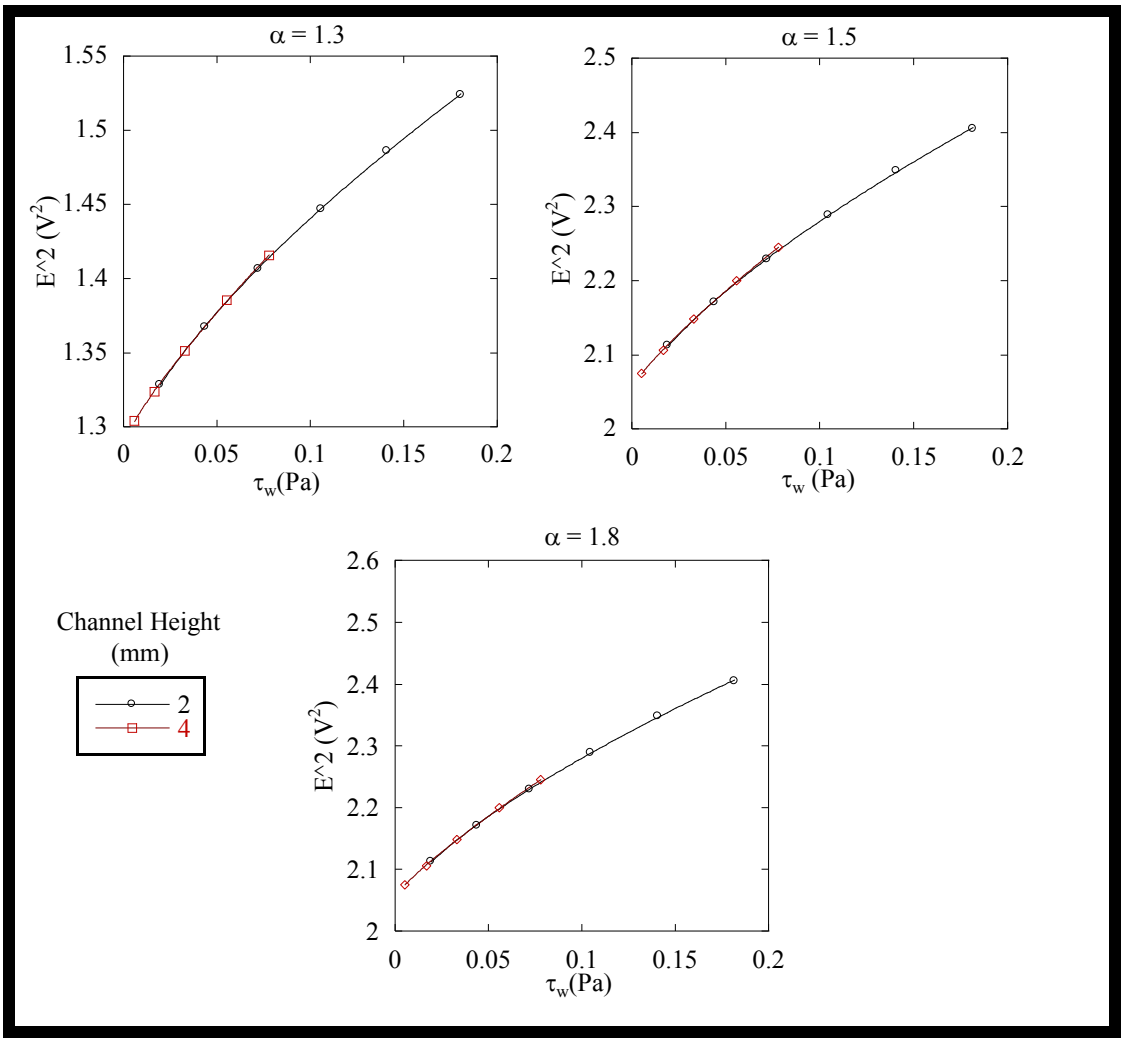

Figure 4.16 – Sensor calibration results at two different channel heights (2 mm and 4 mm, nominal) and three different overheat ratios (α = 1.3, 1.5, and 1.8)

4.3.2 Sensitivity of the Sensor to Flow Angle and Flow Reversals

To quantify the flow-angle sensitivity, the CTA output was recorded with the hot-wire positioned at different angles to the flow (γ, shown in figure 4.17) and compared to the CTA output at γ = 0 degrees (flow perpendicular to hot-wire). A large Reynolds number (Re = 1000) and α = 1.8 was used to heighten the flow-angle sensitivity (Brunn, 1996). The percent difference between the CTA output at the different flow angles and the CTA output with the flow perpendicular to the hot-wire is referred to as 'error'. This error is plotted against the different flow angles in figure 4.18 A). This figure shows that for flow angles smaller than ± 10 degrees, the error was less than 2%. Unfortunately, this figure also showed that the errors for positive and negative flow angles were dissimilar, which suggested that the sensor was sensitive to a flow

reversal (flow angle of 180 degrees). To further study the latter phenomenon, the sensor was calibrated at flow angles of 0 and 180 degrees, and the result is shown in figure 4.18 B). This figure shows that the sensor outputs at the flow angles of 0 and 180 degrees are indeed different, especially at higher wall-shear-stress values. This was hypothesised to be a consequence of the hot-wire not being perfectly centered with the rectangular cavity underneath it, which was caused by imperfections in the machining of the sensor's upper body. However, there is a positive outcome to this result, which is that if the sensor is calibrated at both 0 and 180 degrees, then the direction of the flow can be determined during an experiment by rotating the sensor by 180 degrees and comparing the different CTA voltage outputs (provided that the flow is steady).

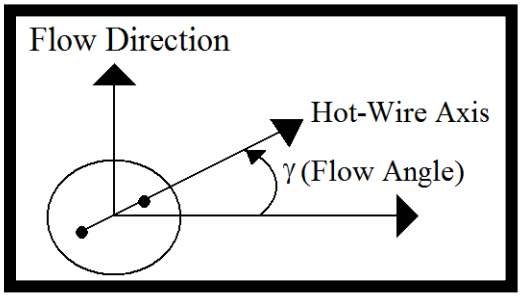

Figure 4.17 – Illustration of flow angle

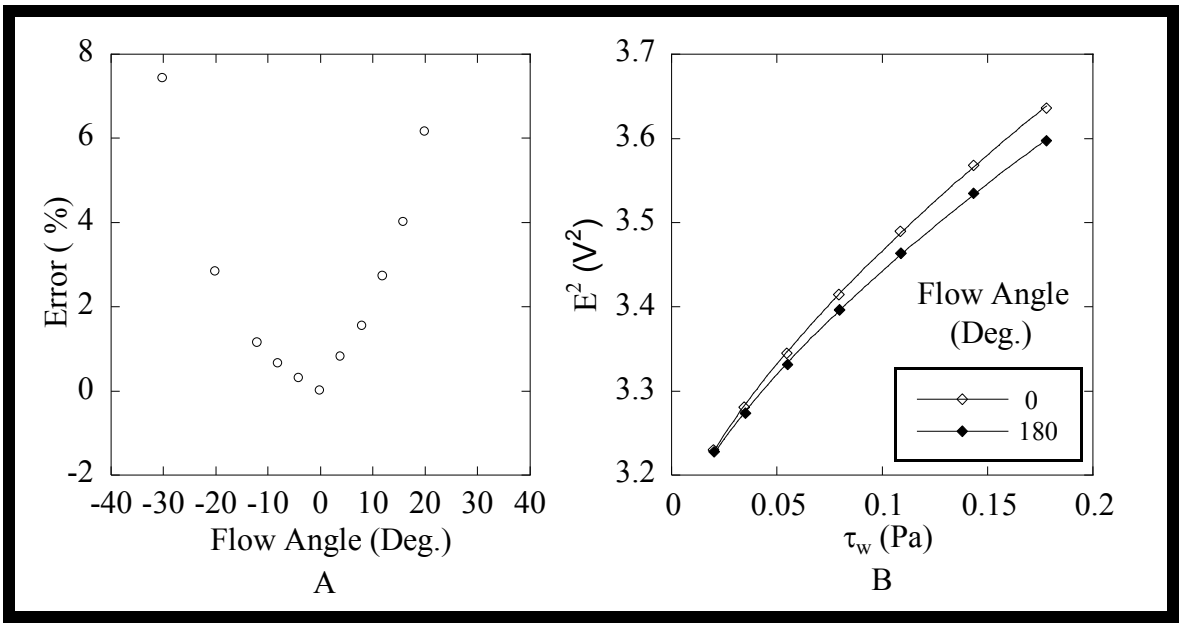

Figure 4.18 – A) Error at different flow angles; B) calibration at 0 and 180 deg. flow angles (Re = 1000; α = 1.8; a = 2.08 mm)

4.3.3 Sensitivity of the Sensor to Flush-Mounting Offset

When a wall-shear-stress sensor is calibrated in a particular set-up and then used in a different setting (in a notebook computer, for example), any mounting imperfections, such as a misalignment in the flushness of the sensor with the surface of interest, could lead to significant errors. Spazzini et al. (1999) demonstrated this effect by calibrating their wall-shear-stress sensor at different height offsets from the surface of interest. From their work, it was anticipated that the sensor proposed and used in this thesis would have similar characteristics. To quantify the sensitivity of the sensor to a flush-mounting offset, an approach similar to the one used by Spazzini et al. (1999) was employed. The sensor was calibrated (with $\alpha = 1.8$) at different height offsets from the bottom of the 2 mm channel, determined using a series of precision gauge blocks, and the results are shown in figure 4.19. They demonstrate that the results obtained at different height offsets are significantly different from each other, and that the negative offset results are far worse (compared with those obtained with zero offset) than the positive ones. They also show that the differences between these results increase with increasing wall-shear stress. However, provided that this offset is kept within ± 0.001 in., which is achievable using the technique described in section 4.2.1, the error in the wall-shear-stress measurement, for the worst case scenario (highest shear stress), will be less than ± 5%.

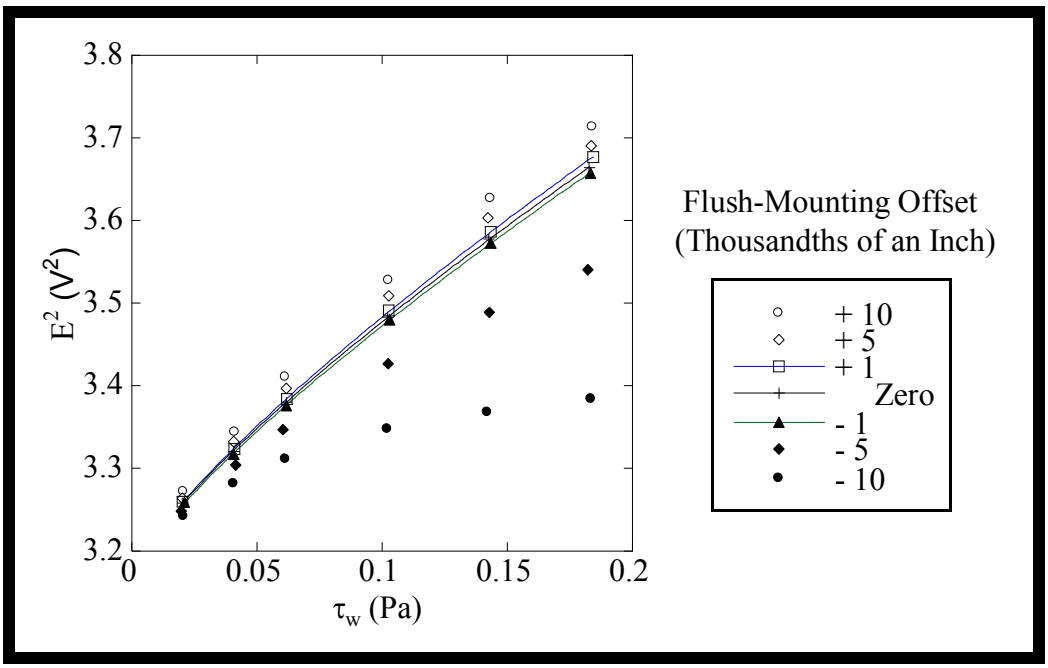

Figure 4.19 – Flush mounting Sensitivity ($\alpha = 1.8$; a = 2.08 mm)

Chapter 5

Applications to Air Flow in a Channel with Partial Blockages: Some Results and Discussions

In the previous chapters, the design, construction, operation, calibration, and validation of the wall-shear-stress sensor were described. Wall-shear-stress measurements obtained with this sensor for air flow in a channel with partial blockages (with different blockage ratios) are presented in this chapter, along with complementary measurements of the upper-wall pressure distributions over and around these blockages. The measurement of both the wall-shear stresses and pressure distributions were conducted in the 2 mm nominal channel (a = 2.08 ±0.02 mm).

5.1 Wall-Shear-Stress Measurements

Instantaneous wall-shear-stress measurements were made at different dimensionless distances (X/H, where H is the actual height of blockage including the thickness of the double-coated tape used to secure it to the channel, if applicable) downstream of blockages, for three different BRs (H/a) and five different nominal Reynolds numbers (100, 300, 500, 700, and 900). The dimensionless downstream distances ranged between 3 and 50, and the actual heights and widths of the blockages along with the blockage ratios investigated are shown in Table 5.1. The Reynolds numbers were based on the average velocity in the TS and the hydraulic diameter ($4A_{cs}/P_w$) of the channel. The average velocity was calculated using data from the wall-static-pressure taps in the upstream-end of the TS (away from the blockages). The accuracies of the measured Reynolds numbers can be shown to be the same as those for the mass flow rate calculated using data from the TSWSPTs (Table 3.2 with L_s = 0.3 m). The correspondence between the nominal and actual Reynolds numbers for all parameters investigated is provided in Appendix F.

Double-Coated Tape Used	H (in.)	Width (in.)	BR (%)
Yes	0.0325	0.755	39.7
Yes	0.0485	0.755	59.2
No	0.0625	1.003	76.3

Table 5.1 – Values of actual blockage height (H), width, and corresponding blockage ratio (BR) for wall-shear-stress measurements

From the acquired instantaneous wall-shear-stress data, the average and root-mean-square (of fluctuations about the average) wall-shear stresses, denoted as τ_{avg} and τ_{rms}, respectively, were calculated for all the (X/H) distances, Reynolds numbers, and BRs investigated. The average wall-shear stress (τ_{avg}) and the root-mean-square of the wall-shear stresses fluctuations (τ_{rms}), were calculated and respectively plotted as a function of the downstream distance from the blockage for all the Reynolds numbers in figures 5.1 A) and B) (BR = 76.3%), 5.2 A) and B) (BR = 59.2%), and 5.3 A) and B) (BR = 39.7%). Given that the sensor can only measure the magnitude (not the direction) of the wall-shear stress, the average wall-shear-stress values plotted in these figures as well all other figures herein (with the exception of figure 5.9) actually represent the absolute value of the wall-shear stress ($|\tau_{avg}|$). The intensity of the wall-shear-stress fluctuations (τ_{rms} / ($|\tau_{avg}|$) is plotted as a function of the downstream distance from the blockage for all Reynolds numbers for the 76.3%, 59.2%, and 39.7% BRs, in figures 5.4, 5.5, and 5.6, respectively. The location of the blockage on these figures is indicated by the solid rectangle on the x-axis. The 59.2% BR measurements performed at dimensionless distances of 4, 25, and 50, were repeated for all Reynolds numbers investigated after having removed and repositioned the blockage, and then once again without removing the blockage. The repeated average and root-mean-square wall-shear stresses, plotted as functions of Reynolds number, are shown in figures 5.7 and 5.8, respectively.

The flow conditions used in the experimental measurements presented in figure 5.3 A) were also investigated numerically, for the case of the fluid flow in the central region of the rectangular duct (away from the side walls) which was assumed to be laminar, steady, and two-dimensional. This laminar flow was simulated using two-dimensional, steady forms of the continuity and Navier-Stokes equations [Schilichting (1979)], in a Cartesian coordinate system. It was assumed that the air flow was effectively isothermal, and its density and dynamic viscosity were constant. A co-located finite-volume method (FVM) proposed by Baliga and Atabaki

(2006) was adapted and used for this work. The computational grids employed were fine enough to ensure that the numerical results were within ± 5% of the extrapolated (Richardson extrapolation) grid-independent values. The experimental measurements and the corresponding numerical predictions are compared in figure 5.9. In this figure, some of the experimental average-wall-shear-stress values were converted to negative values to be consistent with the numerical results. All data pertaining to figures 5.1-5.9 are presented in Appendix F. Finally the power spectral density (PSD) of the wall-shear-stress fluctuations was determined for all the parameters investigated. Plots of these power spectral densities for X/H = 3, BR = 76.3%, and Re = 300, 500, and 900, are shown in figure 5.10.

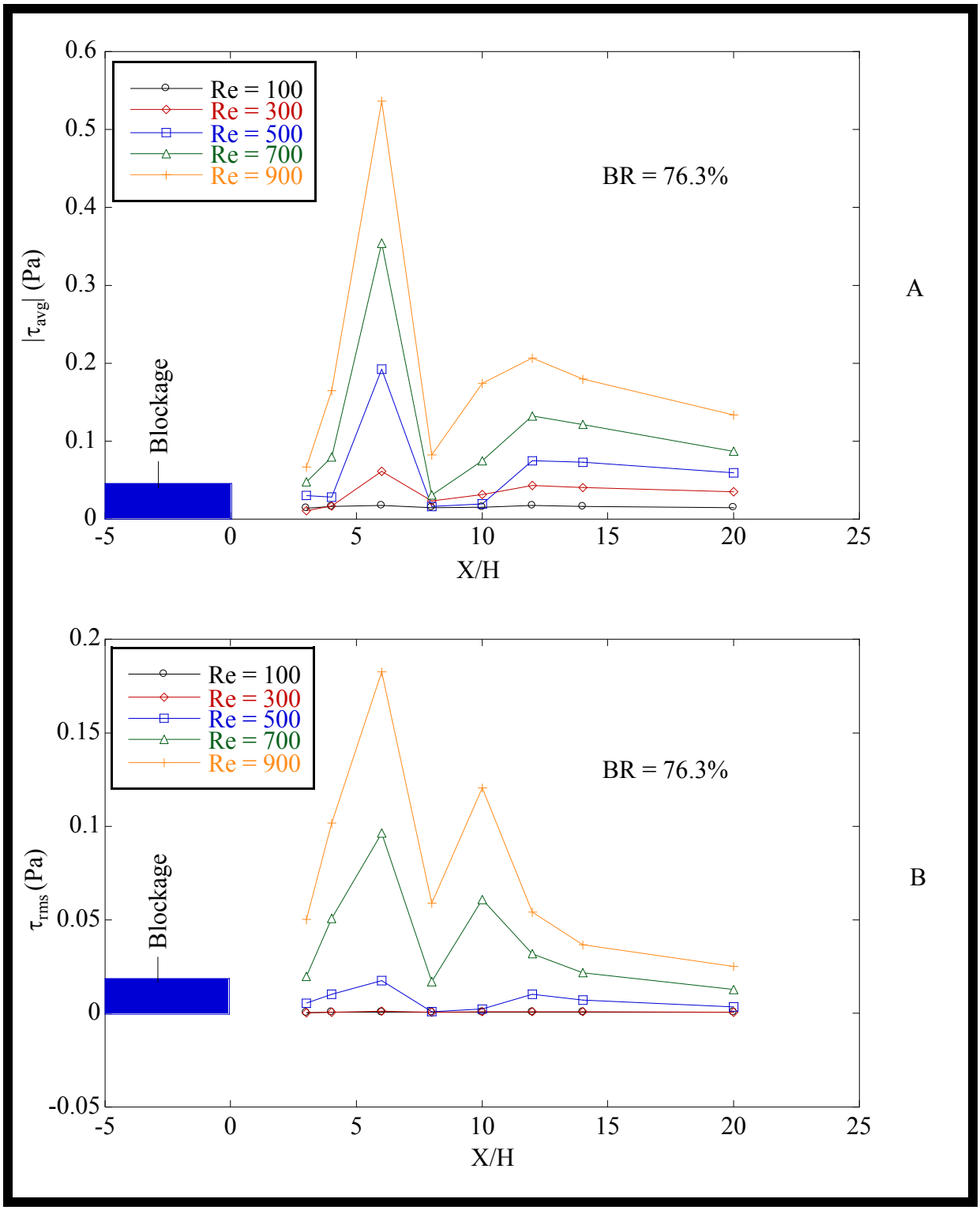

Figure 5.1 – Downstream evolution of the wall-shear stress at different values of Reynolds number (Re) and for BR = 76.3%: A) τ_{avg}; B) τ_{rms}

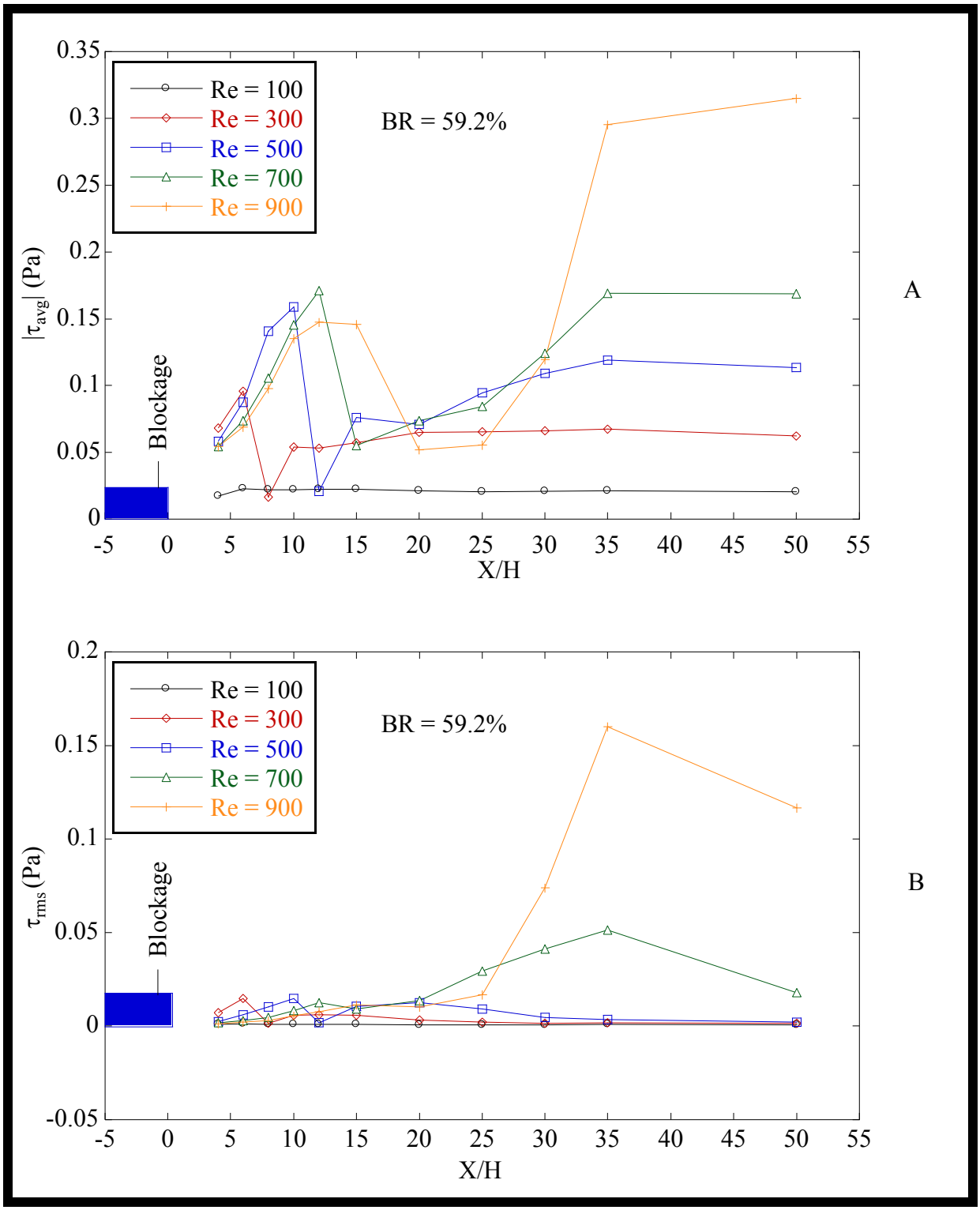

Figure 5.2 – Downstream evolution of the wall-shear stress at different values of Reynolds number (Re) and for BR = 59.2%: A) τ_{avg}; B) τ_{rms}

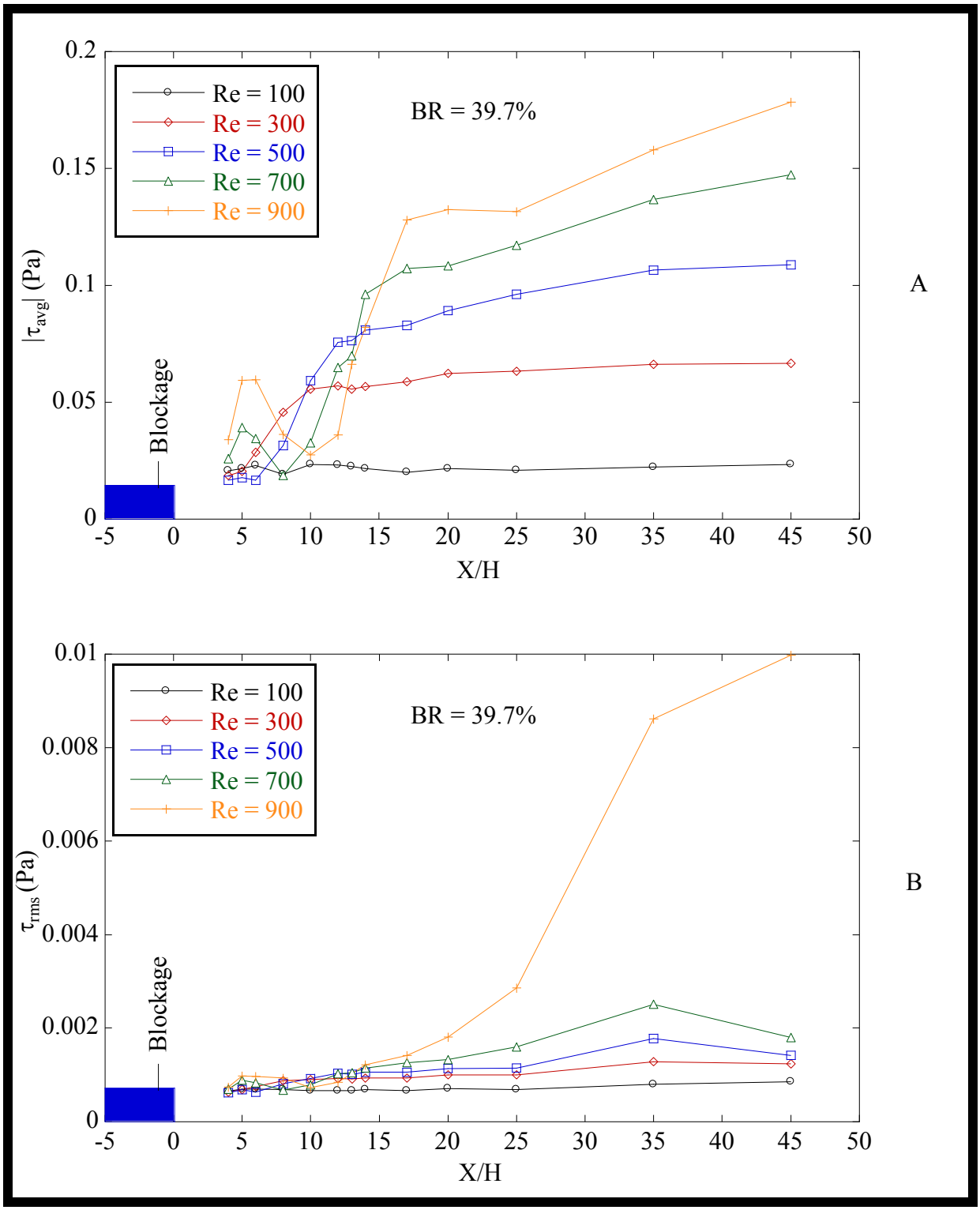

Figure 5.3 – Downstream evolution of the wall-shear stress at different values of Reynolds number (Re) and for BR = 39.7%: A) τ_{avg}; B) τ_{rms}

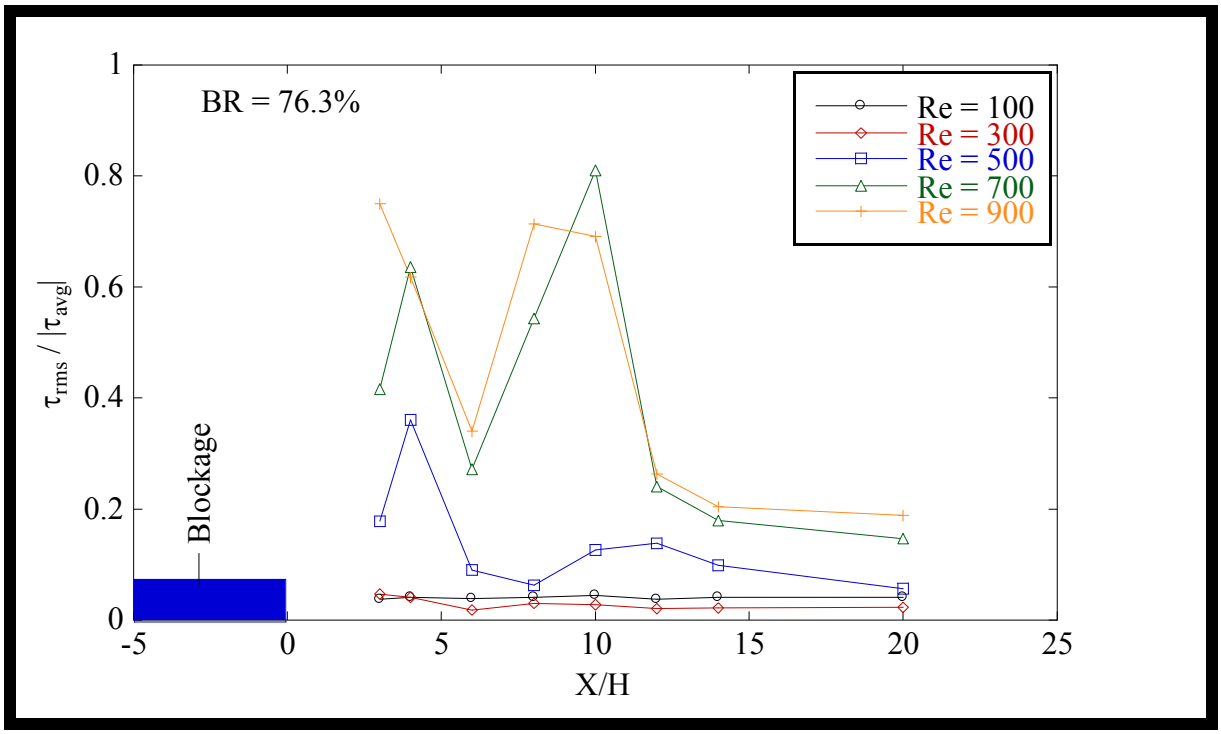

Figure 5.4 – Downstream evolution of the intensity of the wall-shear-stress fluctuations at different values of Reynolds number (Re) and for BR = 76.3%

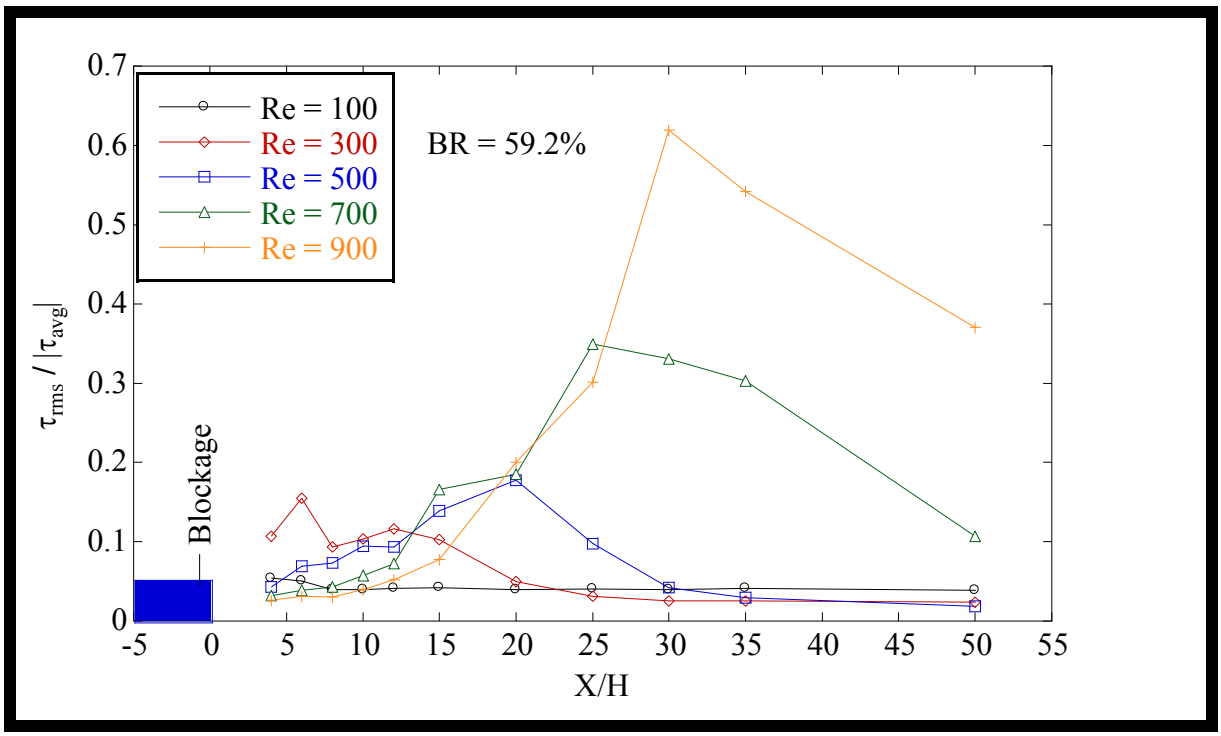

Figure 5.5 – Downstream evolution of the intensity of the wall-shear-stress fluctuations at different values of Reynolds number (Re) and for BR = 59.2%

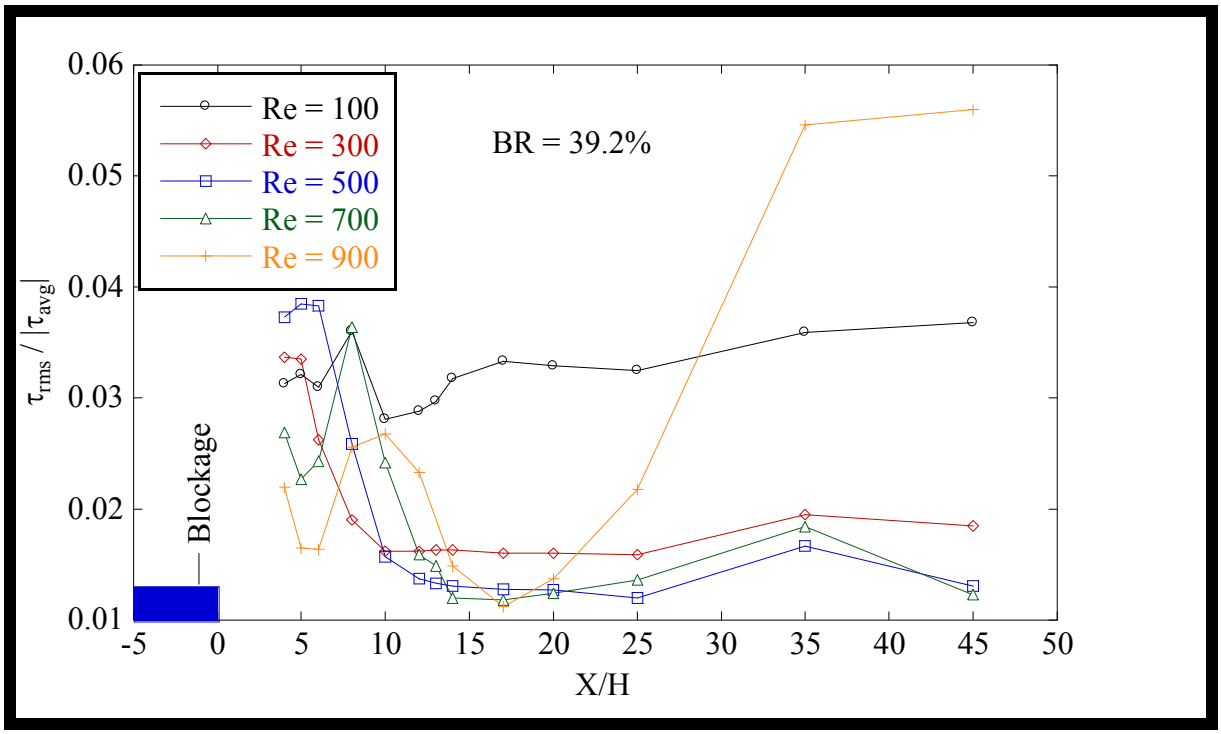

Figure 5.6 – Downstream evolution of the intensity of the wall-shear-stress fluctuations at different values of Reynolds number (Re) and for BR = 39.7%

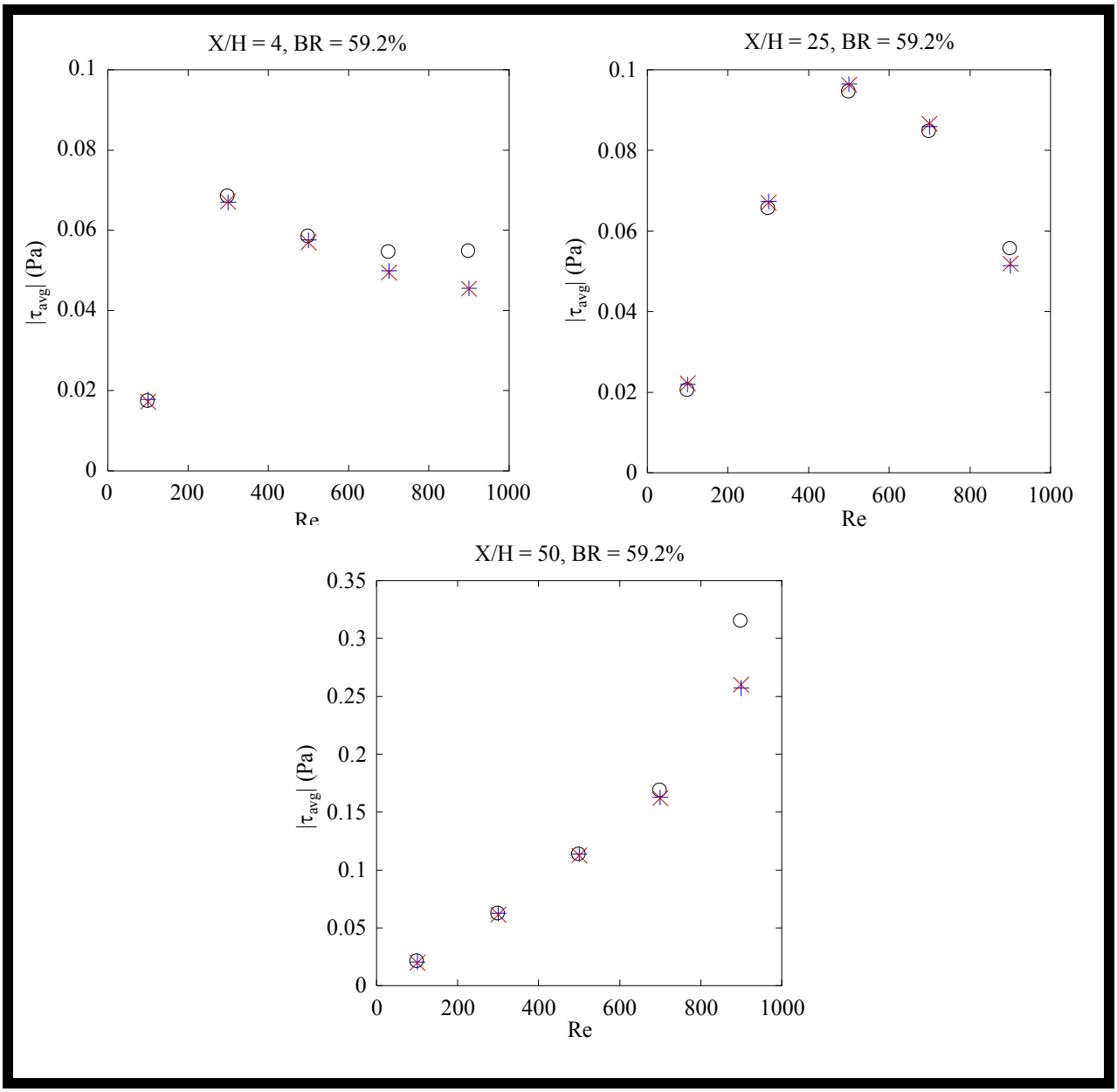

Figure 5.7 – Average wall-shear stress as a function of Re for X/H = 4, 25, and 50. BR = 59.2% Original data: ○; data repeated after repositioning the blockage: +; data repeated without removing blockage: ×)

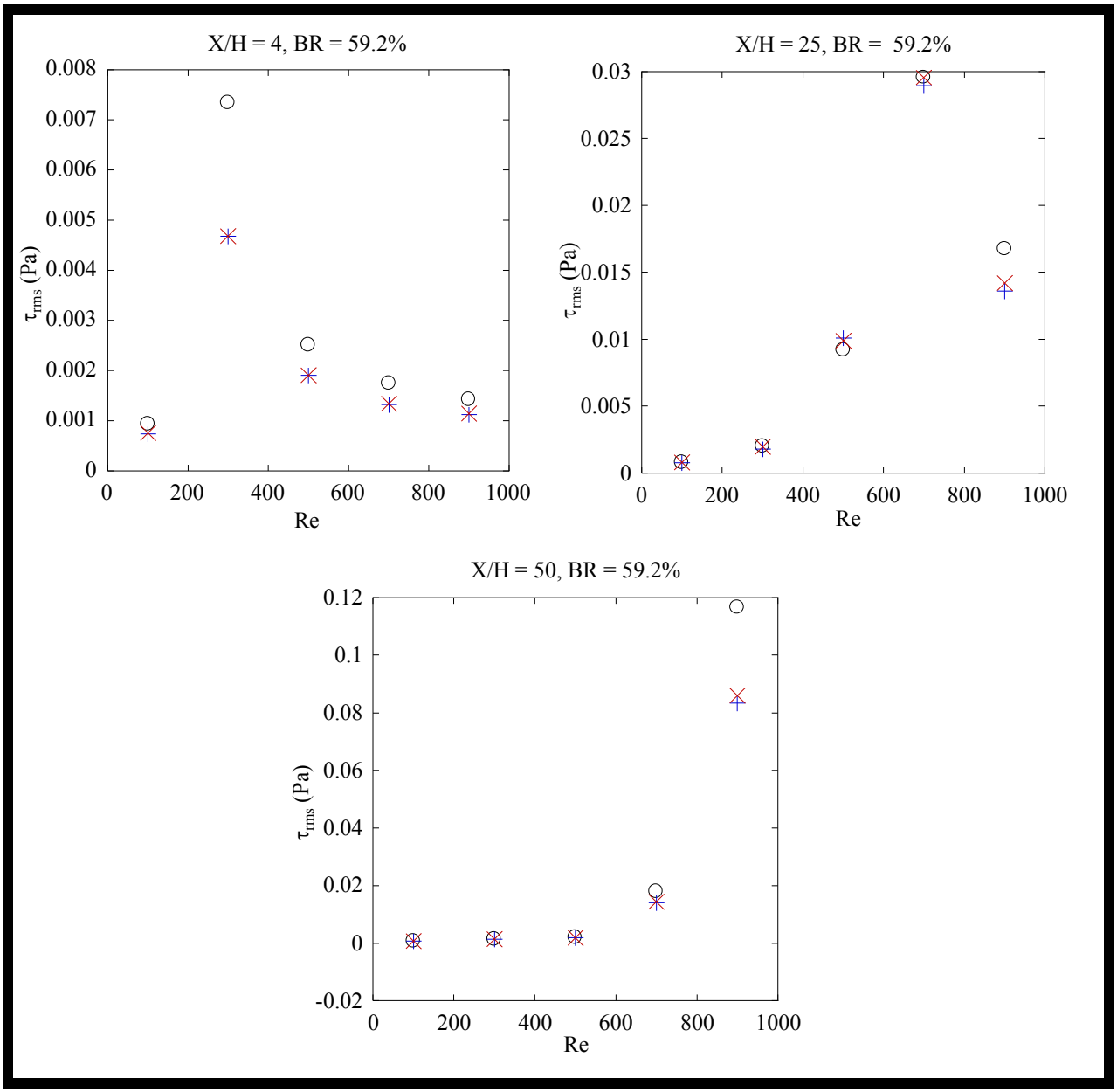

Figure 5.8 – Root-mean-square wall-shear stress as a function of Re for X/H = 4, 25, and 50 BR = 59.2% Original data: ○; results repeated after repositioning the blockage: +; data repeated without removing blockage: ×

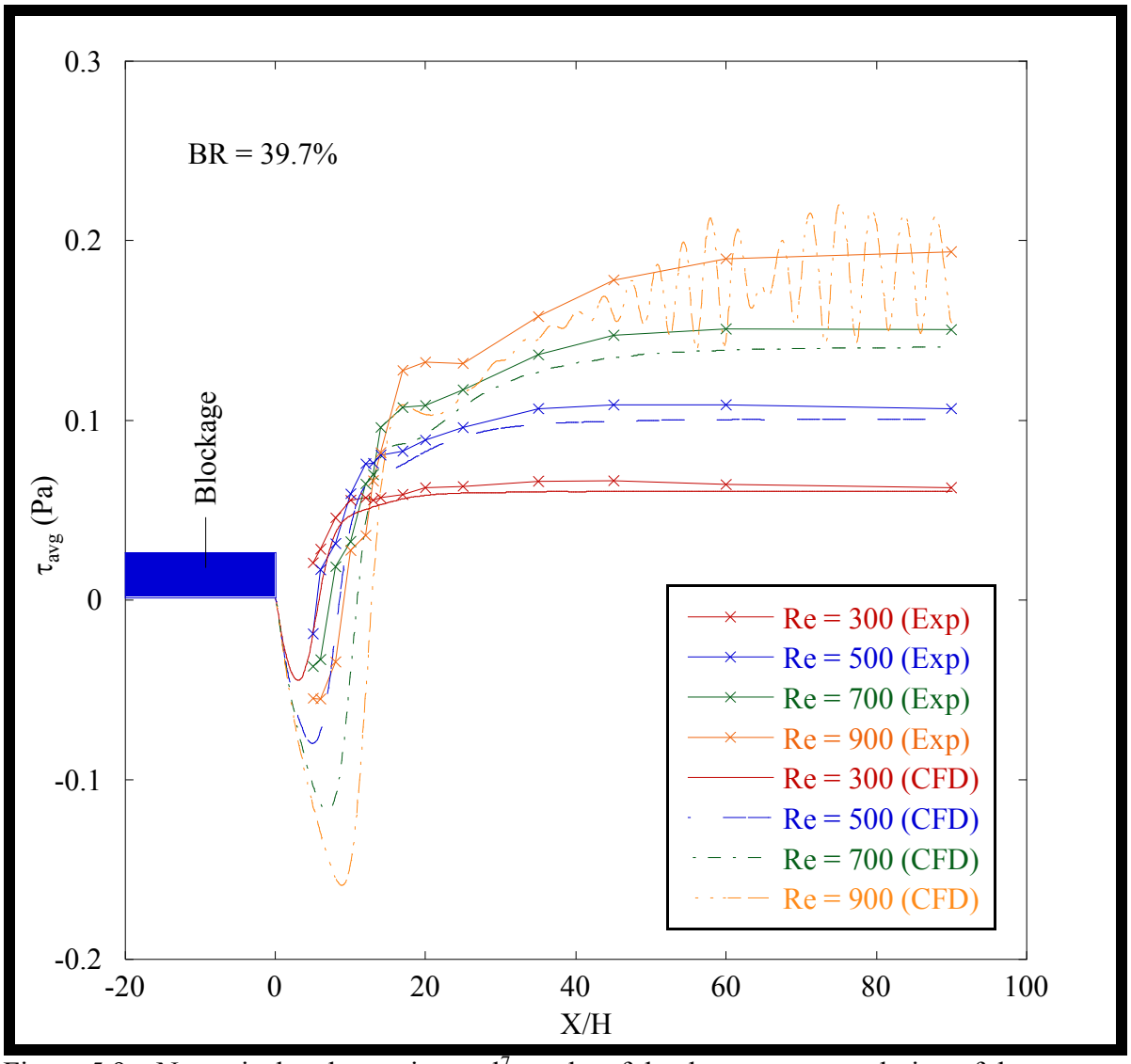

Figure 5.9 – Numerical and experimental[7] results of the downstream evolution of the average wall-shear stress at different values of Reynolds number (BR = 39.7%)

[7] Given that the sensor can only measure the magnitude (not the direction) of the shear stress, some of the experimental wall-shear-stress values obtained in the viscinity of the blockage (within the primary recirculation zone) were converted to negative values, consistent with the corresponding numerical results, which showed that the flow is reversed in this region.

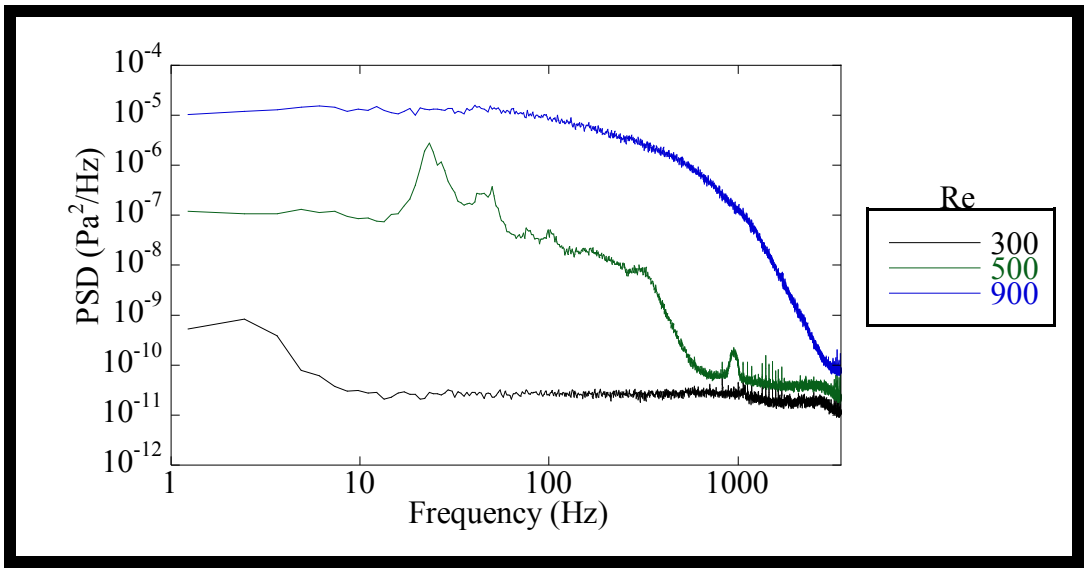

Figure 5.10 – Power spectral densities of wall-shear-stress fluctuations (X/H = 3, BR = 76.2%, Re = 300, 500, and 900)

It is important to note that the sensor was calibrated up to a maximum wall-shear stress of 0.35 Pa. Therefore, all average wall-shear stress data exceeding 0.35 Pa have been calculated using an extrapolation of the calibration curve. Due to the limitations of the sensor, the direction of the wall-shear stress was not accounted for in the previous figures. Furthermore, since the calibration curves at flow angles of 0 and 180 degrees were dissimilar, the results obtained in regions were the flow direction was reversed (mainly within the primary recirculation region) are not entirely accurate. Unfortunately, these regions could not be identified in the experiments undertaken in this work, which means that these parts of the previous figures should be considered qualitatively (as opposed to quantitatively). Despite these limitations, these figures demonstrate some fundamental aspects of the flows encountered downstream of blockages, which are discussed in the next subsection.

5.2 Discussion of the Wall-Shear-Stress Measurements

The average wall-shear stresses obtained for BR = 76.3% (see figure 5.1) were relatively small at the first downstream distance encountered (X/H = 3), then increased to a maximum at X/H = 6, before reducing to a small value at X/H ≈ 8. The region defined by these three dimensionless distances corresponds to the primary recirculation zone, generated immediately downstream of the blockage. Similar increased wall-shear stresses obtained within such

recirculating-flow zones have also been reported for flows downstream of a backward-facing step by Eaton & Johnston (1980), Westphal et al. (1984), Adams & Johnston (1985), Driver & Seegmiller (1985), and Le et al. (1997). The results in figure 5.1 also show that, downstream of the primary recirculation zone, the wall-shear stress increased to a local maximum at around X/H = 12, then slowly settled down to values similar to what would be obtained if no blockages were present. It is possible that this local maximum is caused by a secondary recirculation zone located on the top surface of the channel, which would have the effect of pushing the flow downwards, resulting in an increase in the wall-shear stress on the bottom surface of the channel, as the flow accelerates around the recirculation zone. Additional experiments are needed to confirm this explanation.

The wall-shear-stress results presented in figure 5.2 for the smaller blockage ratio (BR = 59.2%) did not show any evidence of a secondary recirculation zone as observed in figure 5.1. Furthermore, unlike the 76.3% blockage results, which showed that the reattachment lengths were relatively independent of the Reynolds number, the reattachment lengths obtained for the 59.2% blockage (which can be identified by the position of the local minima in figure 5.2) increased in length as the Reynolds number of the flow increased. The approximate values of the reattachment lengths obtained for the 59.2% blockage are: X/H = 8, 12, 15, and 20 for Re = 300, 500, 700, and 900, respectively. The reattachment length for the Re = 100 case was too small to extract from this figure. Similar to the 76.3% blockage results, relatively high wall-shear-stress values were obtained within the primary recirculation zones. However, these high wall-shear stress values were lower than those obtained for the 76.3% blockage.

The wall-shear-stress results for the 39.7% blockage (see figure 5.3) are similar to the ones obtained for the 59.2% blockage because i) no secondary recirculation zone was detected, ii) the reattachment lengths of the primary recirculation zones increased with increasing Reynolds number, and iii) relatively high wall-shear stress values were obtained within the primary recirculation zones. The approximate values of the reattachment lengths obtained for the 39.7% blockage are: X/H = 5, 6, 8, and 11 for Re = 300, 500, 700, and 900, respectively. Once again, the reattachment length for the Re = 100 case could not be extracted for this figure. It is interesting to note that both the reattachment lengths and the relatively high values of wall-shear stress obtained within the primary recirculation region were smaller for the 39.7% blockage than for the 59.2% blockage.

The turbulent shear-stress intensities presented in figures 5.4, 5.5, and 5.6 ranged from 0.01 to 0.8. Regions of high turbulence intensities are usually found within recirculation zones, where the unsteady wall-shear-stress fluctuations are large relative to their average value. Figure 5.4 shows that such a region exists within the primary recirculation zone of the 76.3% blockage. However, for the 59.2% blockage (figure 5.5), the maximum turbulence intensities were located outside the primary recirculation zones and their corresponding distances downstream of the blockage increased as the Reynolds number was increased. The turbulence intensities obtained for the 39.7% blockage (figure 5.6) were relatively small compared to the other two blockages. Furthermore, for all Reynolds numbers investigated (except for Re = 900), the maximum turbulence intensities were located within the primary recirculation zones. It is important to note that when the turbulence intensity is high (above 0.3 – 0.5), there will be some errors in the measured values of τ_{rms} when instantaneous flow reversals occur. As the shear-stress sensor cannot detect flow direction, it was not possible to account for such instantaneous flow reversals.

Figures 5.7 and 5.8 were produced to assess the repeatability of the wall-shear-stress measurements obtained downstream of the 59.2% blockage. It is clear from these figures that if two consecutive series of measurements (covering the range of Reynolds numbers investigated) are taken at a given blockage location, without removing the blockage, then the two sets of data are very repeatable (maximum difference of 4%). Furthermore, these figures show that removing and repositioning the blockage produces repeatable results (maximum difference of 4%) at the lower Reynolds numbers (100-500), but somewhat less repeatable results (maximum difference of 10-20%) at the higher Reynolds numbers (700-900). The lack of repeatability at the higher Reynolds numbers could be attributed to the relatively unsteady nature of these measurements, as attested to in figure 5.5.

The average wall-shear stress downstream of the 39.7% blockage obtained numerically (see figure 5.9) compared relatively well to the ones obtained experimentally, given the complexities involved in such measurements. However, the numerical simulation underpredicted the measured wall-shear-stress data obtained outside the primary recirculation zones and over predicted the wall-shear stress data within these zones. Figure 5.9 also shows that the results obtained at Re = 900 became oscillatory away from the primary recirculation zone. These numerical oscillations confirm that the problem is becoming unsteady at the higher Reynolds numbers. It is also important to note that an attempt was made to numerically predict the wall-

shear stress downstream of the 76.3% blockage using the same numerical scheme described earlier. However, the code was unable to converge, despite some heavy under-relaxation, for all values of Reynolds number higher than 500. This suggested that future numerical studies of such flows most likely require an unsteady numerical scheme.

Lastly, with respect to the power spectral densities (PSDs) shown in figure 5.10 (BR = 76.3%, X/H = 3), the PSD at Re = 300 was relatively flat over the entire range of frequencies, which is a typical of laminar flows. For Re = 900, the PSD obtained started with a high value at the lower frequencies, which gradually decreased at the higher frequencies. This behaviour is characteristic of turbulent flows, which suggests that the blockage may have caused the flow to become turbulent. Furthermore, as can be observed in figure 5.10, for Re = 500, the PSD falls in between that for the other Reynolds numbers and exhibits spikes at certain frequencies. This type of PSD may represent a flow that is undergoing transition. The three distinct flow regimes (laminar, transitional, and turbulent) obtained using this blockage (BR = 76.3%) were also observed with the 59.2% blockage at X/H = 30, and 35. On the other hand, even though the PSDs obtained using the 39.7% blockage exhibited some spikes around certain frequencies, no turbulent PSDs were obtained. These results suggest that for the parameter ranges investigated in this work, turbulent flows are only generated downstream of blockages with large blockage ratios (> 40%).

The results discussed above have confirmed the presence of unsteadiness, separation, reattachment, and laminar-turbulent transition. These results help explain the difficulties experienced by previous researchers and engineers in simulating the flows (using commercial CFD codes) inside notebook computers.

5.3 Pressure Distributions

The pressure distributions over and around blockages with three different BRs were obtained for seven different nominal TS Reynolds numbers (Re = 100, 300, 500, 600, 700, 800, and 900). The actual blockage heights (H), widths, and BRs investigated are shown in Table 5.2. The actual Reynolds numbers achieved during these experiments differed, once again, from the nominal values, because it was difficult to precisely set the flow rate prior to the data acquisition. The actual and nominal values of the Reynolds number for all blockage ratios are provided in Appendix G. These Reynolds numbers were measured using the 5-tube configuration of the

LFEs, and it can be shown that their accuracies are similar to those determined for the mass flow rates measured using the LFEs (Table 3.1).

Double-Coated Tape Used	H (in.)	Width (in.)	BR (%)
No	1/32	1.003	38.2
No	3/64	1.003	57.2
No	1/16	1.003	76.3

Table 5.2 – Values of actual blockage height (H), width, and corresponding blockage ratio (BR) for pressure distributions

The pressure distributions obtained for the seven Reynolds numbers, and for the 38.2%, 57.2%, and 76.3% BRs are presented, in graphical form, in figures 5.12, 5.13, and 5.14, respectively. (The quantitative data for these figures is provided in Appendix G.) In these figures, the pressure drop in the TS relative to a reference point (pressure tap # 60 located 3 inches upstream of the blockage) is plotted as a function of the distance from that reference point. The location of the blockage is denoted by a filled-in rectangle on the x-axis.

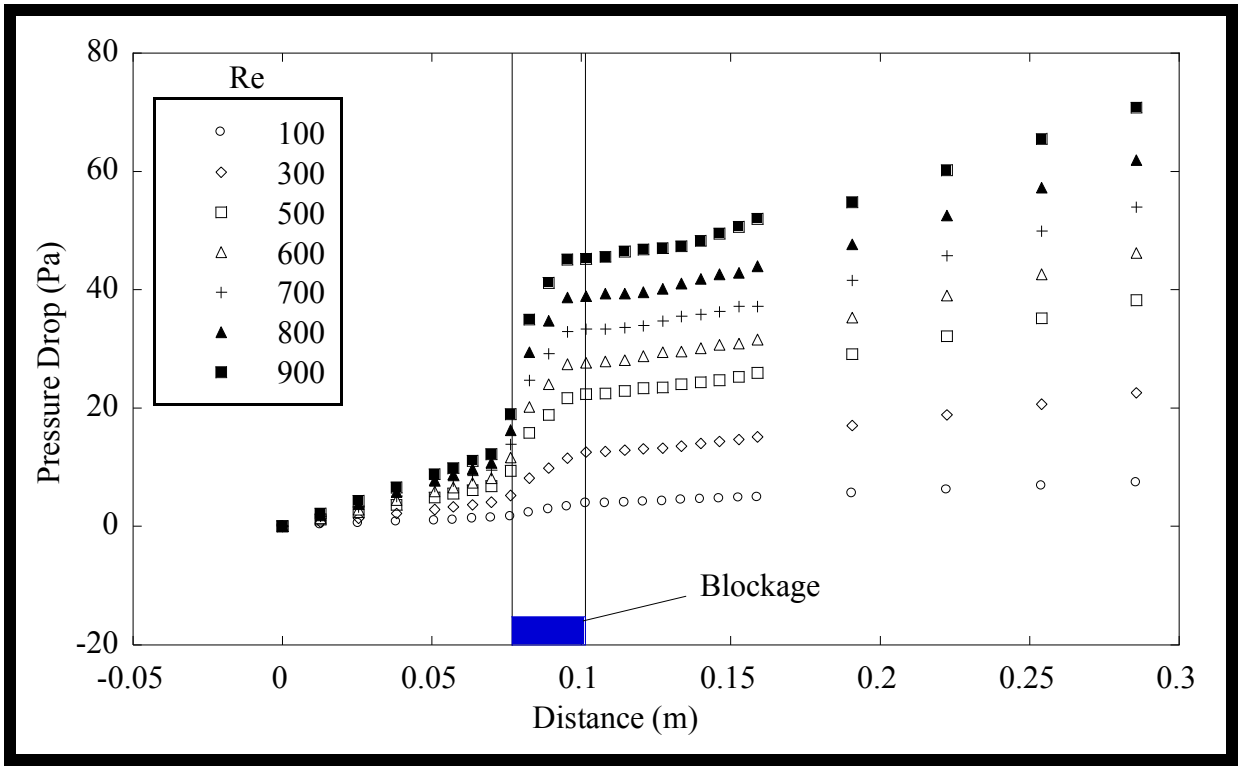

Figure 5.12 – Pressure distributions (BR = 38.2%, a = 2.08 mm)

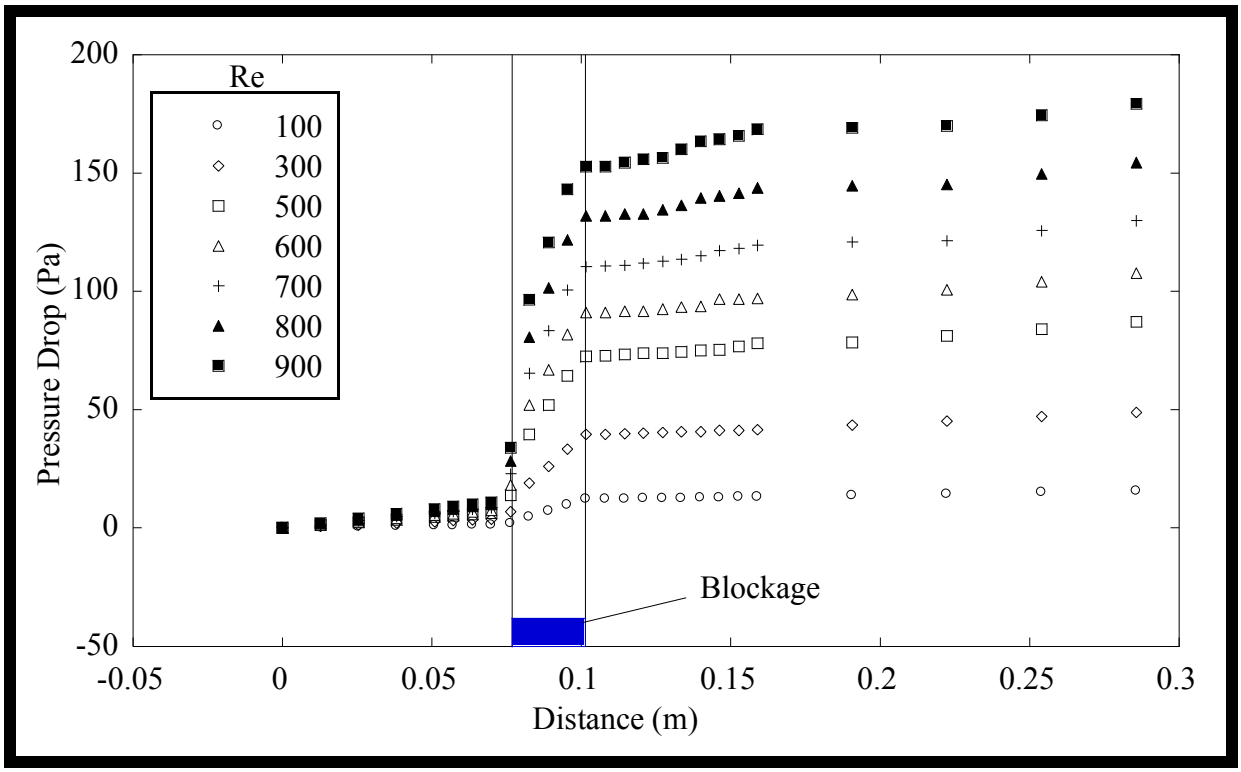

Figure 5.13 – Pressure distributions (BR = 57.2%, a = 2.08 mm)

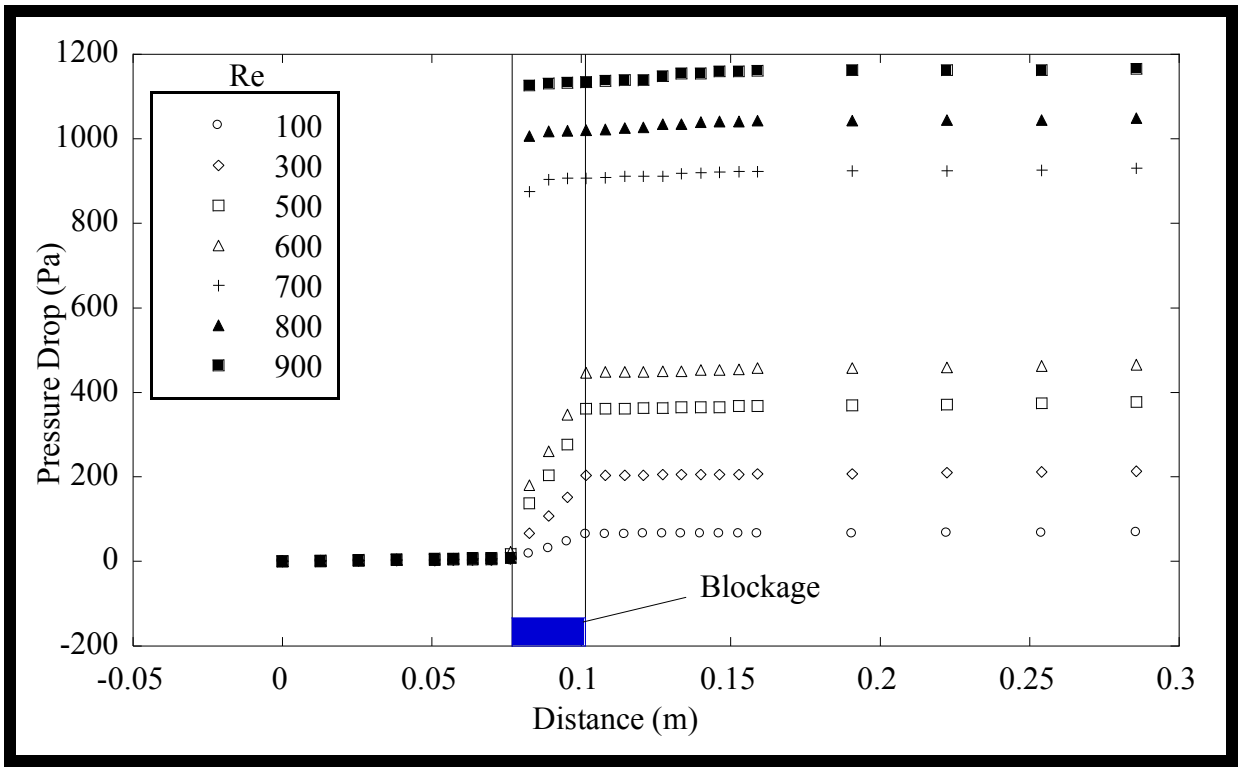

Figure 5.14 – Pressure distributions (BR = 76.2%, a = 2.08 mm)

As expected, the pressure distributions plotted in figures 5.12, 5.13, and 5.14 indicate that the pressure drops across the blockages increase with increasing blockage ratio and Reynolds number. Moreover, the highest BR (76.2%) generated significantly larger pressure drops than the two other BRs. This point is better illustrated in figure 5.15, in which plots of the pressure distributions obtained for the three BRs investigated at a constant Reynolds number of 500 are presented. The results in this figure show that there is a relatively small increase in pressure drop when the blockage ratio is increased from 38.2% to 57.2%. However, there is a significantly greater increase in pressure drop when the blockage ratio is increased from 57.2% to 76.2%. This result is expected because it can be shown (assuming the flow above the blockage to be fully-developed and laminar) that the pressure drop across the blockage is inversely proportional to the gap height (above the blockage) cubed for a constant value of Reynolds number[8]. Lastly, the pressure drops presented in figure 5.14 for Re = 700, 800, and 900 exceeded the 1 kPa limitation of the Barocel and are therefore subject to additional possible error(s).

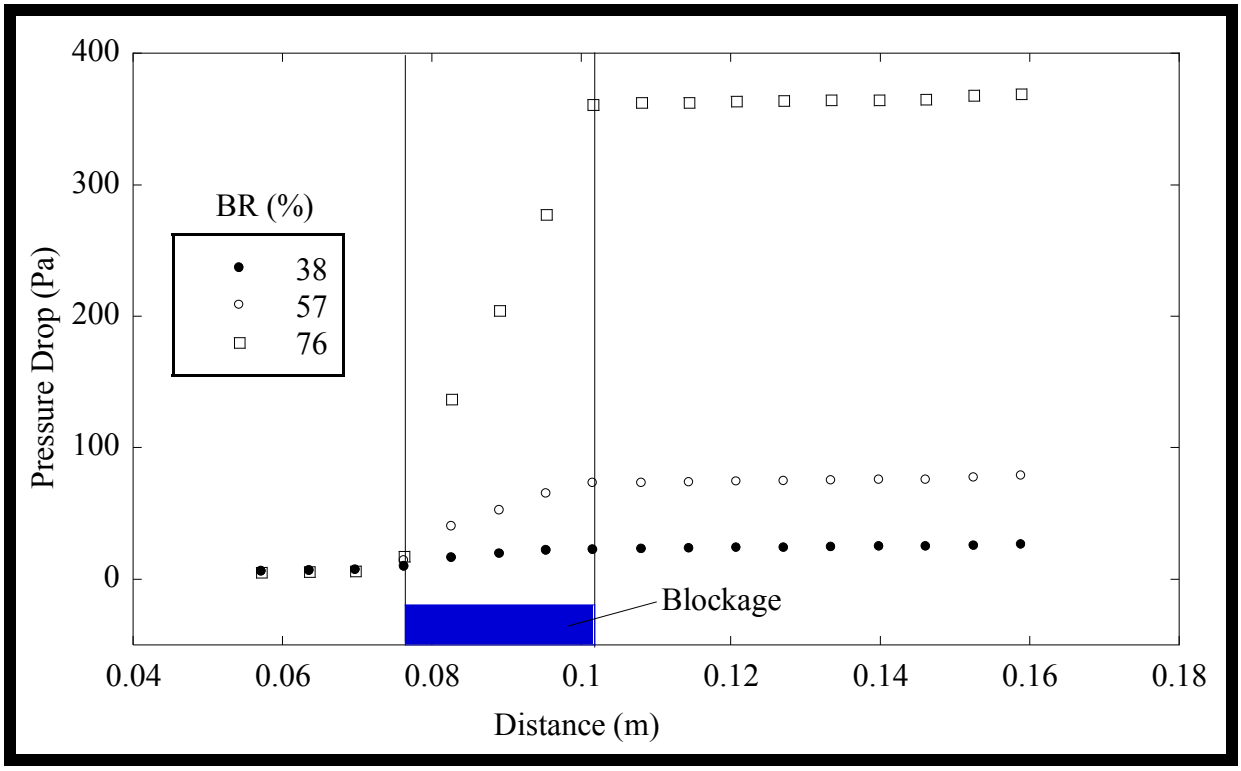

Figure 5.15 – Pressure distributions (Re = 500, BR = 38.2%, 57.2%, and 76.2%)

[8] It can be shown that for a fixed mass flow rate, the Re of a fully developed laminar flow in a parallel-plate channel does not change when the height of the channel is changed. This result is also approximately valid for a wide-aspect-ratio channel, such as the one used in this work. Therefore, the Reynolds number of the flow in the gap above the blockages is almost the same as the Reynolds number of the flow in the TS for a fixed mass flow rate.

Chapter 6

Conclusion

The final chapter of this thesis contains i) a review of the work reported in this thesis and its contributions, and ii) recommendations for extensions of this work.

6.1 Review of the Thesis and its Contributions

In Chapter 1, the motivation, goals, and objectives of this work were discussed. A review of the pertinent published literature was then presented, followed by an overview of the thesis.

In Chapter 2, the components of the air-channel facility were presented and discussed, and three flow-measurement systems (test-section-wall-static-pressure taps, laminar flow elements, and commercial gas-flow meter) were introduced and explained. The development and integration of these flow-measurement systems is one of the contributions to this work. Details on the mini-channel, which is an important component of the air-channel facility, were provided. These details included the procedures for modifying its height, sealing and testing it for leakages, and inserting and positioning blockages within it. The importance of the i) uniformity of the height, and ii) prevention of air leakages was addressed.

In Chapter 3, a comparison of the performance characteristics of the three flow-measurement systems was presented, including a discussion of the use of each system. In this chapter, the temperature- and pressure-measurement techniques, which were required for the two main flow-measurement systems (test-section-wall-static-pressure taps and laminar flow elements), were reviewed. Then, the theoretical equations for calculating the mass flow rate were presented. Finally, the uncertainties and limitations of these two flow-measurement systems were discussed in this chapter.

In Chapter 4, descriptions of the design and construction of the novel wall-shear-stress sensor were first provided. These included i) the manufacturing process for the different components of the sensor, ii) the assembly of these components, and iii) the details on the attachment of a hot-wire. The design of the sensor and the procedures used for constructing it were the main contributions to this work. This chapter then discussed the operating procedures for the novel sensor, which was another important contribution to this work. This discussion also

included the detailed procedure for mounting the sensor flush with the bottom surface of the channel and the calibration of the sensor. Finally, the applicability of the sensor for measurement of flows within the mini-channels of notebook computers was discussed. Most importantly, the sensor was validated by showing that it provided reliable measurements for flows in different channel heights, after having been calibrated in the 2 mm channel.

In Chapter 5, the results of wall-shear-stress measurements performed for air flow in a channel with partial blockages, and pressure distributions over and around these blockages, were presented. Although the accuracy of some of the wall-shear-stress measurements were limited by i) flow reversals, and ii) shear-stress magnitudes outside of the maximum calibrated shear stress, the wall-shear stress measurements nevertheless provided significant physical insights pertaining to the complexity of (nominally) laminar flow over partial blockages within mini-channels. The observed unsteadiness, separation, reattachment, and laminar-turbulent transitions clearly demonstrated the possible complexities of flows within notebook computers (and consequent difficulties in their simulation using commercially available CFD codes).

6.2 Recommendations for Extensions of This Work

The manufacturing process for the proposed sensor was rather difficult and could benefit from some simplifications. For future works, the outer casing, lower body, and lower prongs can be eliminated from its assembly. Instead, the upper body can be designed to replace the outer casing and lower body. This can be achieved by soldering the bottom end of the upper prongs to a solid wire, which extends all the way through and out of the bottom of the sensor. This design would eliminate the need for the lower prongs and lower body. These two wires could then be soldered to a BNC female connector and directly connected to the CTA, rather than using the TSI support column.

The design of the sensor can also be modified to accommodate two hot-wires placed parallel to each other and separated by a small distance. This configuration was used by Spazzini et al. (1999), and has allowed these authors to measure the direction of the wall-shear-stress, which is essential in the investigation of flows exhibiting flow reversals. (However, if knowledge of the direction of the wall-shear stress is not essential, then the addition of a second hot-wire would not be necessary.) Nevertheless, the sensitivity of the single-wire sensor to flow reversals should be reduced as much as possible. This can be achieved by using tighter machining

tolerances to ensure that the cavity and hot-wire are as perfectly centered with the top surface of the upper body as possible.

In this thesis, there was no attempt made to measure the frequency response of the sensor, which would be important if the sensor is to be used in a turbulent flow. The frequency response can be tested by designing a rig, such as the one constructed by Khoo et al. (1998), for producing a know fluctuating flow field. A simpler technique would involve placing the sensor in a fully-developed turbulent channel flow and measuring the wall-shear-stress intensity. If the latter is close to the generally accepted value (0.4), then the sensor will most likely have satisfactory response characteristics. Furthermore, the influence of the substrate material, cavity dimension, and overheat ratio on the frequency response of the sensor should be determined and used to optimize its performance.

It would be desirable to conduct numerical studies on the flow over cavities, such that the influence of the sensor's cavity on the flow field can be assessed. These studies can be extended to include the heat transfer from the hot-wire, and the results can be used to develop a theory for the operating principles of the sensor. With an operating theory, it would be possible to determine appropriate temperature compensation techniques, which would enable the sensor to be used in non-isothermal flows.

It would be useful to modify the test section to enable rapid insertion and positioning of blockages. This would reduce the delay time between experiments and increase the total number of parameters that could be investigated in a reasonable amount of time. Furthermore, it would be interesting to investigate additional parameters, such as the blockage width, the number of blockages, and their positions from the sensor (above or upstream).

Finally, the author expects that the work presented in this thesis will lead to practical measurements of the flow within an actual notebook computer. Such measurements would then be presented to the sponsors of this work (Intel) for validation and verification of corresponding numerical simulations.

References

Adams, E.W., Johnston, J.P. and Eaton, J.K., 1984. Experiments on the structure of turbulent reattaching flow. *Rep. MD-43. Thermosciences Division*, Dept. of Mech. Eng., Stanford University, Palo Alto, United States.

Addad, Y., Laurence, D., Talotte, C., and Jacob, M.C., 2003. Large eddy simulation of a forward-backward facing step for acoustic source identification. *International Journal of Heat and Fluid Flow*, **24**, pp. 562-571.

Alfredsson, P.H., Johansson, A.V., Haritonidis, J.H., and Eckelmann, H., 1988. The fluctuating wall-shear stress and the velocity field in the viscous sublayer. *Physics of Fluids*, **31**, pp. 1026–1033.

Armaly, B.F., Durst, F., Pereira, J.C.F., and Schönung, B., 1983. Experimental and theoretical investigation of backward-facing step. *Journal of Fluid Mechanics*, **127**, pp. 473-496.

Aoyagi, M., Takehana, N., Masuda, S., and Ariga, I., 1986. Improvement of hot film surface gage for wall shear stress measurement. *Fluid Control and Measurement*, **2**, pp. 863-868.

Azad, R.S., 1983. Corrections to measurements by hot wire anemometer in the proximity of a wall. *Report MET-7*, Dept. of Mech. Eng., University of Manitoba, Winnipeg, Canada.

Baliga, B.R. and Atabaki, N., 2006, Control-Volume-Based Finite Difference and Finite Element Methods, Handbook of Numerical Heat Transfer (2nd Ed.),W.J. Minkowycz, E.M. Sparrow, and J.Y. Murthy, Chapter 6, John Wiley & Sons, New York.

Bhatia, J.C., Durst, F., and Johanovic, J., 1982. Corrections of hot-wire anemometer measurements near walls. *Journal of Fluid Mechanics*, **122**, pp. 411–431.

Bellhouse, B.J. and Schultz, D.L., 1966. Determination of mean and dynamic skin friction, separation and transition in low-speed flow with a thin-film heated element. *Journal of Fluid Mechanics*, **24**, pp. 379-400.

Bergles, A.E., 2003. Evolution of cooling technology for electrical, electronic, and microelectronic equipment. *IEEE Transactions on Components and Packaging Technologies*, **26** pp. 6-15.

Blackwelder, R.F. and Haritodinis, J.H., 1983. Scaling of the bursting frequency in turbulent boundary layers. *Journal of Fluid Mechanics,* **132**, pp. 87–103.

Brunn, H.H., 1996. Hot-Wire Anemometry: Principles and Signal Analysis, Oxford University Press.

Carvahlo, M.G., Durst, F., and Pereira, J.C.F., 1985. Predictions and measurements of laminar flow over two-dimensional obstacles. *Applied Mathematical Modelling*, **11**, pp. 23-33.

Castro, I.P., 1992. Pulsed-wire anemometry. *Experimental Thermal and Fluid Science*, **5**, pp. 770-780.

Chambers, F.W., Murphy, H.D., and Mceligot, D.M., 1983. Laterally converging flow. Part 2. Temporal wall shear stress. *Journal of Fluid Mechanics*, **127**, pp. 403-428.

Chew, Y.T., Khoo, B.C., and Li, G.L., 1994. A time-resolved hot-wire shear stress probe for turbulent flow: use of laminar flow calibration. *Experiments in Fluids*, **17**, pp.75–83.

Chew, Y.T., Shi, S.X., and Khoo, B.C., 1995. On the near-wall corrections of single hot-wire measurements. *International Journal of Heat and Fluid Flow*, **16**, pp. 471-476.

Chew, Y.T., Khoo, B.C., Lim, C.P., and Teo, C.J., 1998a. Dynamic response of hot-wire anemometer. Part II: a flush-mounted hot-wire and hot-film probes for wall shear stress measurements. *Measurement Science and Technology*, **9**, pp. 762–776.

Chew, Y.T., Khoo, B.C., and Li, G.L, 1998b. An investigation of wall effects on hot-wire measurements using a bent sublayer probe. *Measurement Science and Technology*, **9**, pp. 67–85.

Comte-Bellot, G., 1965. Ecoulement turbulent entre deux parois paralleles. *Publications Scientifiques et Techniques du Ministere de l'Air*, no. **419**.

Cook, W.J. and Giddings, T.A., 1988. Response of hot-element wall shear-stress gages in laminar oscillating flows. *American Institute of Aeronautics and Astronautics,* **26**, pp. 706–713.

Cook, W.J., 1994. Response of hot-element wall shear stress gauges in unsteady turbulent flows. *American Institute of Aeronautics and Astronautics,* **32**, pp. 1464–1471.

Driver, D.M. and Seegmiller, H.L., 1985. Features of a reattaching turbulent shear layer in divergent channel flow. *American Institute of Aeronautics and Astronautics*, **23**, 163-171.

Eaton, J.K. and Johnston, J.P., 1980. Turbulent flow reattachment: An experimental study of the flow and structure behind a backward-facing step. *Rep. MD-39,* Thermosciences Division, Dept. of Mech. Eng., Stanford University, Palo Alto, United States..

Eckelmann, H., 1974. The structure of the viscous sublayer and the adjacent wall region in a turbulent channel flow. *Journal of Fluid Mechanics*, **65**, pp. 439-459.

Fernholz, H.H., Janke, G., Schober, M., Wagner, P.M., and Warnack, D., 1996. New developments and applications of skin-friction measuring techniques. *Measurement Science and Technology*, **7**, pp. 1396–1409.

Fernholz, H.H. and Warnack, D., 1998. The effects of a favourable pressure gradient and of the Reynolds number on an incompressible axisymmetric turbulent boundary layer. Part 1. The turbulent boundary layer. *Journal of Fluid Mechanics*, **359**, pp. 329-356.

Freymuth, P., 1983. History of Thermal Anemometry, Handbook of Fluids in Motion, Ann Arbor.

Fox, R.B., McDonald, A.T., and Pritchard, P.J., 2006, Introduction to Fluid Mechanics, sixth ed., Wiley.

Garimella, S.V., Joshi, Y.K., Bar-Cohen, A., Mahajan, R., Tohr, K.C., Carey, V.P. Baelmans, M., Lohan, J., Sammakia, B., and Andros, F., 2002. Thermal challenges in next generation electronic systems – summary of panel presentations and discussions. *IEEE Transactions on Components and Packaging Technologies*, **25**, pp. 569-575.

Goldstein, R.J., Eriksen, V.L., Olson, R.M., and Eckert, E.R.G., 1970. Laminar separation, reattachment and transition of the flow over a downstream-facing step. *ASME Journal of Basic Engineering*, **92**, 732-741.

Incropera, F.P., DeWitt, D.P., Lavine, A.S., and Bergman, T.L., 2007. Fundamental of Heat and Mass Transfer, sixth ed., Wiley.

Jiang, F., Gupta, B., Tai, Y.C., and Goodman, R., 1995. Measurement of instantaneous turbulent shear stress distribution by MEMS based sensors. *Bull. APS*, **40** 12', FC 2.

He, S., Ariyaratne, C., and Vardy, A.E., 2011. Wall shear stress in accelerating turbulent pipe flow. *Journal of Fluid Mechanics*, **685**, pp. 440-460.

Kamalesh, K., Sirkar, and Hanratty, T.J., 1970. Relation of turbulent mass transfer to a wall at high Schmidt numbers to the velocity field. *Journal of Fluid Mechanics*, **44**, pp. 589-603.

Khoo, B.C., Chew, Y.T. and Li, G.L., 1996. Time-resolved near-wall hot-wire measurements: use of laminar flow wall correction curve and near-wall calibration technique. *Measurement Science and Technology*, **7**, pp. 564-575.

Khoo, B.C., Chew, Y.T., Lim, C.P., and Teo, C.J., 1998a. Dynamic response of hot-wire anemometer. Part I: a marginally-elevated hot-wire probe for near-wall velocity measurements *Measurement Science and Technology*, **9**, pp. 749–761.

Krishnamoorthy, L.V., Wood, D.H., Antonia, R.A., and Chambers, A.J., 1985. Effect of wire diameter and overheat ratio near a conducting wall. *Experiments in Fluids*, **3**, 121–127.

Leclercq, D.J.J., Jacob, M.C., Louistot, A., and Talotte, C., 2001. Forward-backward facing step pair: aerodynamic flow, wall pressure and acoustic characterization. *American Institute of Aeronautics and Astronautics* 2001-2249.

Le, H., Moin, P., and Kim, J., 1997. Direct numerical simulation of turbulent flow over a backwards-facing step. *Journal of Fluid Mechanics*, **330**, pp. 349-374.

Lee, T. and Mateescu, D., 1998. Experimental and numerical investigation of 2-D backward-facing step flow. *Journal of Fluids and Structure*, **12**, pp. 703-716.

Liepmannh, H. and Skinner, G., 1954. Shearing-stress measurements by use of a heated element. *NACA T N,* no. 3268.

Ligrani, P.M. and Bradshaw, P., 1987. Subminiature hot-wire sensors: development and use. *Journal of Physics E: Scientific Instruments*, **20**, pp. 323–332.

Löfdahl, L. and Gad-el-Hak, M., 1999. MEMS applications in turbulence and flow control. *Progress in Aerospace Sciences*, **35**, pp. 101–203.

McBrien, R.K., 1986. Fully Developed Turbulent Flow in Rectangular Interrupted Plate Ducts. *Doctoral Thesis,* Dept. of Mech. Eng., McGill University, Montréal, Canada.

Madavan, N.K, Deutsch, S., and Merkle, C.L., 1985. Measurements of local skin friction in a microbubble-modified turbulent boundary layer. *Journal of Fluid Mechanics*, **156**, pp. 237-256.

Menendez, A.N., Ramaprian, B.R., 1985. The use of flush-mounted hot-film gauges to measure skin friction in unsteady boundary layers. *Journal of Fluid Mechanics*, **161**, pp. 139-159

Mouromtseff, I.E., 1942. Water and forced-air cooling of vacuum tubes. *Proc. IRE*, **30**, pp. 190-205.

Murphy, J.D. and Westphal, R.V., 1986. The laser interferometer skin friction meter: a numerical and experimental study. *Journal of Physics E: Scientific Instruments*, **12**, pp. 744.

Nagano, Y. and Tsuji, T., 1994. Recent developments in hot- and cold-wire techniques for measurements in turbulent shear flows. *Experimental Thermal and Fluid Science*, **9**, pp. 94-110.

Ng, H.C.H., Marusic, I., Monty, J.P, Hutchins, N., and Chong, M.S., 2007. Oil film interferometry in high Reynolds number turbulent boundary layers, *16th Australasian Fluid Mechanics Conference.*

Padmanabhan, A., Goldberg, H.D., Breuer, K.S., and Schmidt, M.A., 1995. A silicon micromachined floating-element shear-stress sensor with optical position sensoring by photodiodes, *Bull. APS*, **40,** 12, FI 1.

Pope, S.B., 2000. Turbulent Flows, Cambridge University Press.

Popovich, A.T., 1969. Statistical analysis of fluid flow fluctuations in the viscous layer near a solid wall. *Industrial & Engineering Chemistry Fundamentals,* **8**, pp. 609-614.

Samuel, A.D., 2007. Experiments for the determination of the interfacial stress jump for fluid flows in channels with adjacent open and porous domains. *Master Thesis,* Dept. of Mech. Eng., McGill University, Montréal, Canada.

Schlichting, H., 1979, Boundary-Layer Theory, seventh ed., McGraw-Hill, New York.

Schmidt, M.A., Howe, R.T., Senturia, S.D., and Haritonidis, J.H., 1988. Design and calibration of a microfabricated floating-element shear-stress sensor. *IEEE Transactions on Electron Devices*, **35**, pp. 750–757.

Shah, D.A. and Antonia, R.A., 1987. Scaling of wall shear stress fluctuations in a turbulent duct flow. *American Institute of Aeronautics and Astronautics,* **25**, pp. 22–29.

Singh, U.K., and Shaw, R., 1972. Hot-wire anemometer measurements in turbulent flow close to a wall. *DISA Conference on Fluid Dynamic Measurements,* Leicester University Press, Leicester, UK, pp. 35-58.

Spazzini, P.G., Iuso, G., Onorato, M., and Zurlo, N., 1999. Design, test and validation of a probe for time-resolved measurement of skin friction. *Meas. Science and Technology*, **10**, pp. 631–639.

Spazzini, P.G., Iuso, G., Onorato, M., Zurlo, N., and Di Cicca, G.M, 2001. Unsteady behavior of back-facing step flow. *Experiments in Fluids*, **30**, pp. 551-561.

Sturzebecher, D., Anders, S., and Nitsche, W., 2001. The surface hot wire as a means of measuring mean and fluctuating wall shear stress. *Experiments in Fluids*, **31**, pp. 294–301.

Taylor, J. R., 1997. An Introduction to Error Analysis, second ed., University Science Books.

Tennekes, H. and Lumley, J.L. 1972. A First Coarse in Turbulence, MIT Press.

Wagner, P.M., 1991. The use of near-wall hot-wire probes for time resolved skin-friction measurements. *Advances in Turbulences*, **3**, pp. 524–529.

Westphal, R.V., Johnston, J.P., and Eaton, J.K., 1984. Experimental study of flow reattachment in a single-sided sudden expansion. *Rep. MD-41. Thermosciences Division*, Dept. of Mech. Eng., Stanford University.

Wills, J.A.B., 1962. The correction of hot-wire readings for proximity to a solid boundary *Journal of Fluid Mechanics*, **12**, pp. 388–396.

Yazawa, K. and Bar-Cohen, A., 2002. Energy efficient cooling of notebook computers. *The Eighth Intersociety Conference on Thermal and Thermomechanical Phenomena in Electronic Systems*, **8**, pp. 785-791.

Zemskaya, A.S., Levitskiy, V.N., Repik, Y.U., and Sosedko, Y.P., 1979. Effect of the proximity of the wall on hot-wire readings in laminar and turbulent boundary layers. *Journal of Fluid Mechanics*, **8**, pp. 133–41.

Appendix A

Relative Humidity Sensor

A relative humidity sensor (Vaisala HMP60) was purchased and installed next to the inlet of the variable-height mini-channel. This sensor was used to assess the influence of the relative humidity (RH) on both the hot-wire anemometry and pressure drop measurements. The RH sensor requires a stable 11-30 VDC power supply, and outputs a voltage of 0-5 VDC that is linearly proportional to the relative humidity range (0-100%). This sensor's accuracy is ± 3% (0 - 90% RH), and ± 5% (90 – 100% RH). The connection diagram for this sensor is shown in figure A.1. In this figure, pin 2 (signal channel 1), corresponds to the relative humidity signal, and Pin 4 (signal channel 2) corresponds to the temperature signal, which was not used in this work.

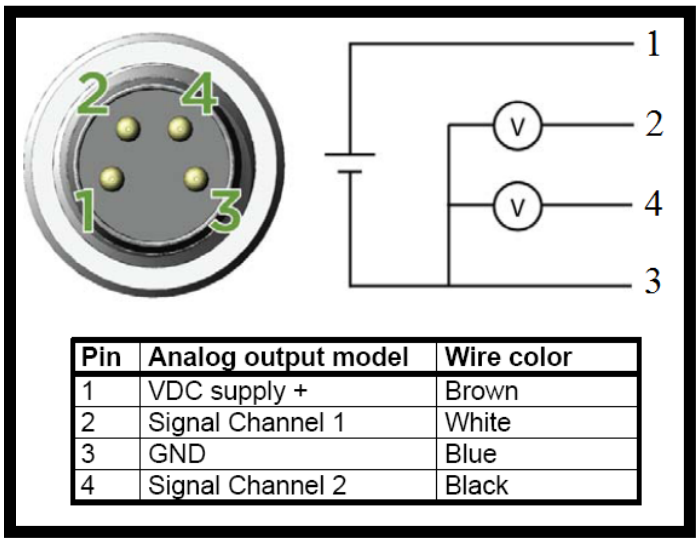

Pin	Analog output model	Wire color
1	VDC supply +	Brown
2	Signal Channel 1	White
3	GND	Blue
4	Signal Channel 2	Black

Figure A.1 – Connection diagram for Vaisala HMP60 RH sensor

Appendix B

Wall-Static-Pressure-Tap Distances

Tap #	Distance (mm)	Tap #	Distance (mm)	Tap #	Distance (mm)	Tap #	Distance (mm)	Tap #	Distance (mm)	Tap #	Distance (mm)
1	62.990	38	297.88	75	533.10	112	768.08	149	1003.1	186	1238.2
2	69.090	39	304.20	76	539.33	113	774.40	150	1009.5	187	1244.5
3	75.450	40	310.50	77	545.83	114	780.84	151	1015.9	188	1250.9
4	81.840	41	316.89	78	552.17	115	787.10	152	1022.2	189	1257.3
5	88.160	42	323.38	79	558.57	116	793.43	153	1028.6	190	1263.6
6	94.570	43	329.67	80	564.90	117	799.89	154	1035.0	191	1269.9
7	100.98	44	336.09	81	571.20	118	806.15	155	1041.2	192	1276.2
8	107.25	45	342.44	82	577.64	119	812.61	156	1047.6	193	1282.6
9	113.73	46	348.76	83	583.91	120	818.98	157	1054.0	194	1289.0
10	119.94	47	355.23	84	590.34	121	825.31	158	1060.3	195	1295.2
11	126.37	48	361.49	85	596.66	122	831.55	159	1066.6	196	1301.7
12	132.65	49	367.76	86	602.88	123	837.86	160	1073.0	197	1307.9
13	139.06	50	374.25	87	609.30	124	844.34	161	1079.4	198	1314.4
14	145.31	51	380.50	88	615.68	125	850.60	162	1085.8	199	1320.7
15	151.65	52	386.85	89	621.95	126	856.97	163	1092.1	200	1326.9
16	158.06	53	393.34	90	628.48	127	863.36	164	1098.4	201	1333.4
17	164.36	54	399.65	91	634.75	128	869.73	165	1104.9	202	1339.8
18	170.79	55	405.92	92	641.04	129	875.91	166	1111.1	203	1346.2
19	177.20	56	412.26	93	647.35	130	882.52	167	1117.5	204	1352.5
20	183.61	57	418.71	94	653.85	131	888.74	168	1123.9	205	1358.8
21	189.85	58	424.92	95	660.17	132	895.16	169	1130.0	206	1365.2
22	196.23	59	431.34	96	666.51	133	901.54	170	1136.6	207	1371.4
23	202.50	60	437.72	97	672.88	134	907.89	171	1142.9	208	1377.8
24	208.91	61	444.16	98	679.16	135	914.21	172	1149.3	209	1384.2
25	215.28	62	450.44	99	685.50	136	920.51	173	1155.5	210	1390.6
26	221.61	63	456.75	100	691.83	137	926.92	174	1162.0	211	1397.0
27	227.97	64	463.20	101	698.36	138	933.26	175	1168.3	212	1403.2
28	234.25	65	469.42	102	704.64	139	939.59	176	1174.6	213	1409.7
29	240.63	66	475.94	103	710.96	140	945.93	177	1181.0	214	1415.9
30	247.00	67	482.18	104	717.40	141	952.31	178	1187.3	215	1422.4
31	253.34	68	488.60	105	723.48	142	958.65	179	1193.7	216	1428.8
32	259.73	69	495.00	106	730.07	143	965.08	180	1200.1	217	1435.1
33	265.98	70	501.38	107	736.53	144	971.45	181	1206.5	218	1441.3
34	272.44	71	507.54	108	742.69	145	977.78	182	1212.8	219	1447.7
35	278.94	72	514.09	109	749.04	146	984.13	183	1219.2	220	1454.1
36	285.19	73	520.40	110	755.38	147	990.48	184	1225.5	221	1460.6
37	291.63	74	526.80	111	761.78	148	996.88	185	1231.9		

Table B.1 – Pressure tap numbers and corresponding distances from the upstream-end of the test-section top plate

Appendix C

Thermocouple Calibration Curve-Fit Data

The following quadratic polynomial was used to fit the calibration data for the 13 thermocouples employed in this work: $T\ (°C) = C1 + C2 \cdot V + C3 \cdot V^2$, where V is the thermocouple output voltage, and C1, C2, and C3 are the calibrations constants. The related details are shown in Table C.1 for each thermocouple.

Thermocouple Code Name	Calibration Constants		
	C1	C2	C3
T40	-0.233	17214.9	-229242
T41	-0.227	17214.5	-231861
T42	-0.218	17200.8	-228320
T43	-0.231	17200.3	-228237
T44	-0.224	17206.4	-229260
T45	-0.225	17206.6	-230772
T46	-0.238	17217.0	-231411
T47	-0.231	17208.1	-228853
T48	-0.234	17201.3	-227860
T49	-0.236	17202.1	-228183
T50	-0.241	17198.8	-226115
T51	-0.248	17199.8	-227125
T52	-0.292	17227.3	-228840

Table C.1 – Thermocouple calibration curve-fit data

Appendix D

Detailed Drawings for the Novel Wall-Shear-Stress Sensor

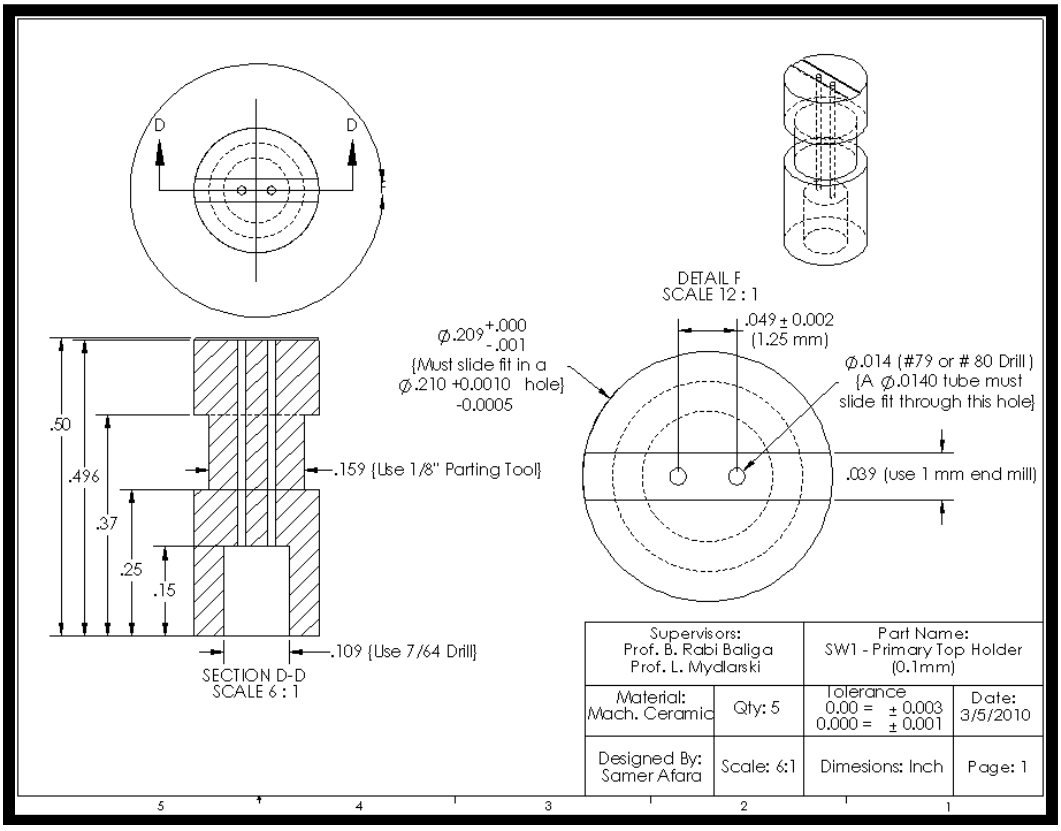

Figure D.1 – Detailed drawings for upper body of sensor

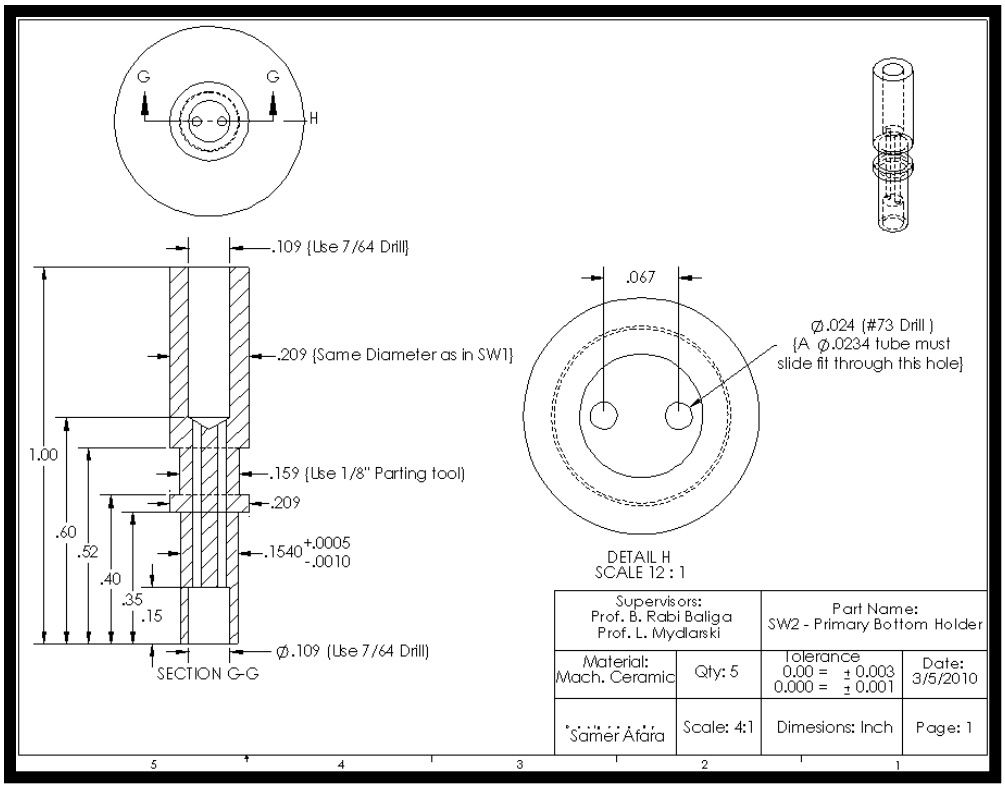

Figure D.2 – Detailed drawings for lower body of sensor

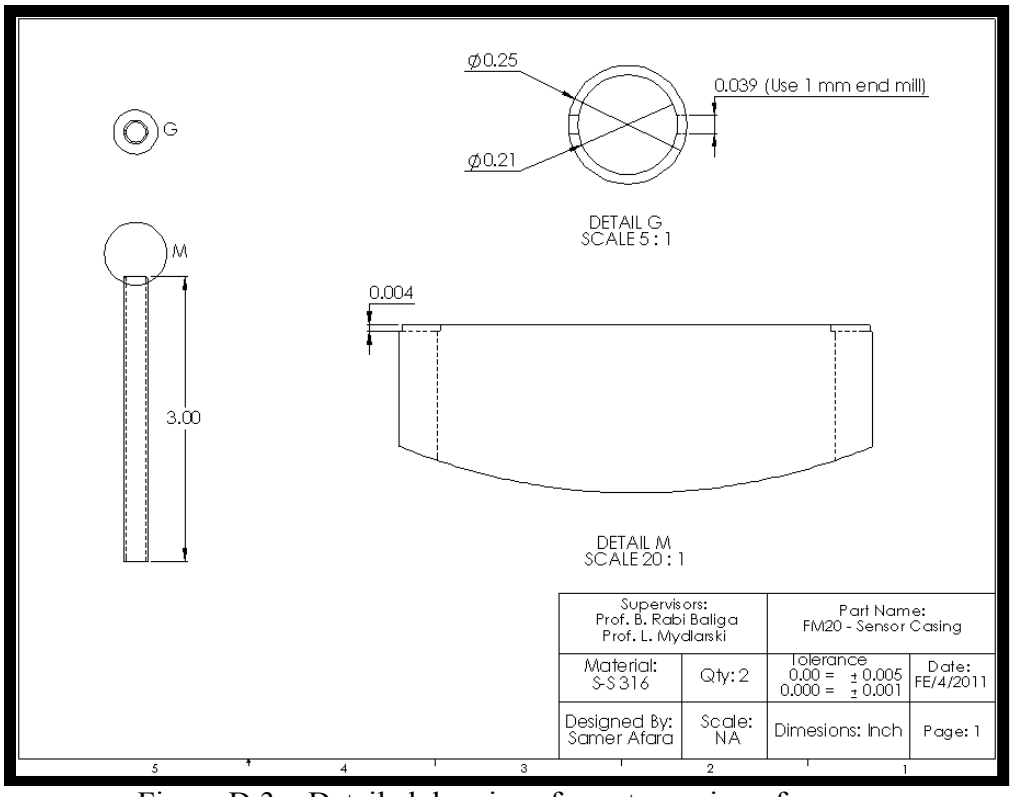

Figure D.3 – Detailed drawings for outer casing of sensor

Appendix E

Ambient-Temperature Drift Compensation

For optimal accuracy, the sensor should be calibrated once thermal equilibrium is achieved between the flow and the surface of the mini-channel (that is, when thermocouples T49 and T40 are within 0.3 °C of each other). By doing so, both the flow temperature and the surface temperature of the mini-channel will be accounted for during the sensor's calibration. The resulting temperature at thermal equilibrium is denoted as the ambient temperature (T_a) herein. Furthermore, the time required for thermal stability can be reduced by maximizing the flow through the mini-channel.

Any drift in T_a will cause a corresponding change in R_a. An approximate relation between these two quantities is:

$$R_2 = R_a[1 + c_a(T_2 - T_a)], \qquad (E.1)$$

where T_2 is the ambient temperature including its drift, R_2 is the resulting hot-wire ambient-temperature resistance at T_2, and c_a is the temperature coefficient of resistivity, which is constant for a given hot-wire material. The latter was determined by i) changing the temperature in the lab to obtain different values of T_2 and corresponding R_2, ii) plotting (R_2/R_a) as a function of ($T_2 - T_a$), iii) fitting a least squares line through this data, and iv) determining the slope of this line. The resulting value for the temperature coefficient of resistivity was approximately 0.0039 $°C^{-1}$, which is almost equal to the standard value for tungsten (0.0036 $°C^{-1}$) tabulated in Brunn (1995).

It remains to determine the appropriate technique required to compensate for a drift in ambient temperature (T_a + drift) during an experiment, after having calibrated the sensor at an ambient temperature equal to T_a. Two different compensation techniques were investigated, which consisted of using the same i) operating resistance (R_w), and ii) overheat ratio, during calibration and experiment. To test these two techniques, a baseline calibration curve was first obtained for a given R_a (14.97 ohms). Then, several other calibration curves were obtained on different days (where T_a and R_a had changed), using both the same operating resistances and overheat ratios as the ones used during the baseline calibration. The different calibration curves

obtained using these two compensating techniques, were compared to the baseline calibration and the results are shown in figure E.1 A) and B), respectively.

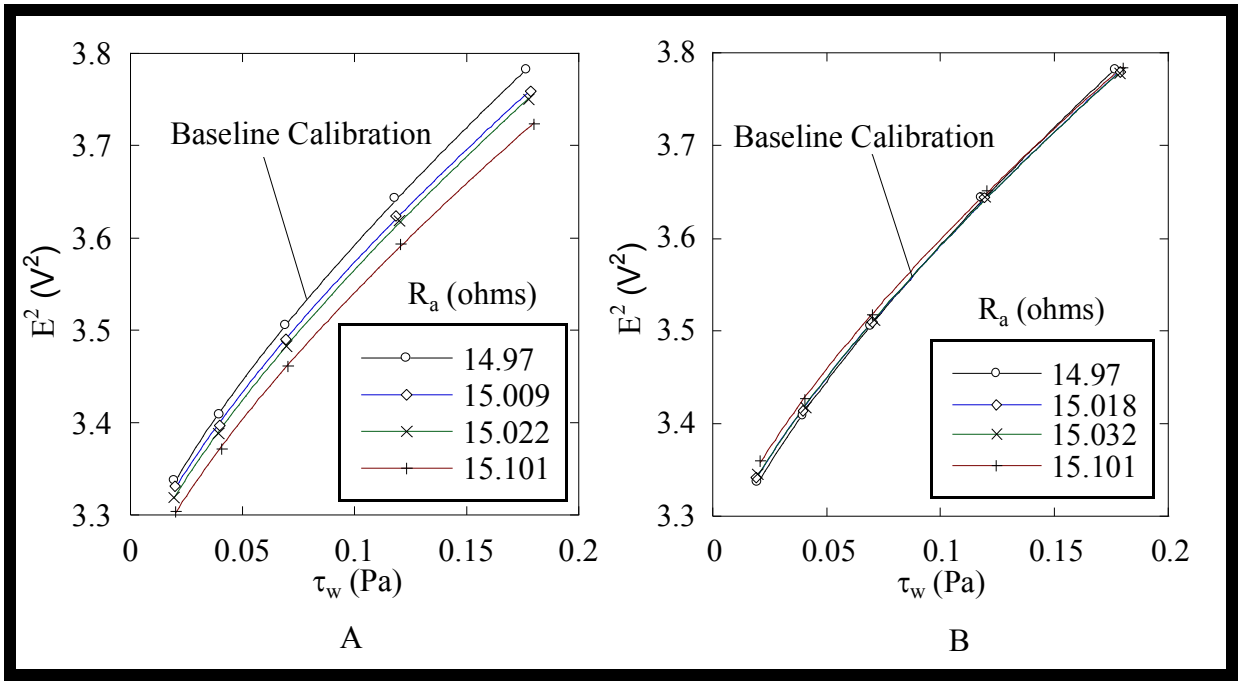

Figure E.1 – Calibration curves: A) same operating resistance; B) same overheat ratio (1.8)

Figure E.1 B) shows that using the same overheat ratio to compensate for ambient-temperature drifts leads to calibration curves that are almost coincident with the baseline calibration provided that the change in R_a is smaller than 0.05 ohms. On the other hand, figure E.1 A) shows that using the same operating resistance to compensate for these drifts leads to significant differences between the calibration curves and the baseline calibration. Therefore, the best compensation technique is to adjust the operating resistance such that the overheat ratio used during an experiment is the same as the one used during the calibration.

Appendix F

Data for Figures in Section 5.1

X/H	Re = 100	Re = 300	Re = 500	Re = 700	Re = 900
3	93.3	301.7	492.5	689.3	899.8
4	99.8	302.3	495.3	718.4	894.3
6	99.4	300.3	500.7	703.6	895.7
8	102.2	303.6	501.2	699.2	904.9
10	101.2	299.3	508.9	694.9	905.0
12	98.3	298.2	499.4	697.8	904.8
14	100.0	300.8	495.5	698.3	895.7
20	100.3	298.1	499.8	703.0	898.9

Table F.1 – Actual Reynolds number corresponding to nominal Reynolds number for wall-shear-stress results (BR = 76.3%)

X/H	Re = 100	Re = 300	Re = 500	Re = 700	Re = 900
4	97.7	302.3	500.9	705.7	902.4
6	99.8	301.4	501.2	704.7	901.1
8	98.2	302.9	505.3	704.6	904.4
10	95.9	298.9	501.7	704.2	898.6
12	102.4	304.1	501.7	704.0	897.9
15	100.0	296.5	498.9	701.0	901.7
20	93.8	300.2	495.5	688.8	888.5
25	99.5	299.4	495.9	701.9	900.9
30	97.2	295.5	499.3	693.7	885.8
35	100.5	301.4	508.3	694.3	894.7
50	100.6	296.2	497.2	699.2	893.3
4R[9]	95.1	301.8	497.1	694.7	896.8
4RR[10]	97.7	298.9	496.4	693.7	898.4
25R	97.1	295.3	502.1	700.3	894.6
25RR	100.4	296.6	491.1	691.8	893.1
50R	97.4	295.8	497.2	688.6	888.8
50RR	96.2	295.5	494.5	689.5	891.4

Table F.2 – Actual Reynolds number corresponding to nominal Reynolds number for wall-shear-stress results (BR = 59.2%)

[9] R represents the results repeated after having removed and repositioned the blockage
[10] RR represents the repeated results without removing the blockage

X/H	Re = 100	Re = 300	Re = 500	Re = 700	Re = 900
4	94.4	293.3	493.1	691.4	879.9
5	100.5	294.0	488.3	679.5	874.7
6	100.4	293.6	484.8	679.7	870.9
8	91.4	292.1	491.1	679.8	872.2
10	101.1	298.1	498.3	691.7	889.4
12	98.9	300.6	500.4	687.9	880.4
13	100.6	297.9	497.4	687.6	883.6
14	104.2	308.8	500.6	708.2	912.1
17	97.4	299.5	506.5	711.4	902.1
20	95.0	301.1	504.9	704.6	907.0
25	101.6	303.2	499.2	701.9	888.7
30	96.6	303.8	497.0	687.4	893.5
35	96.0	301.5	502.8	700.8	898.2
45	104.1	301.7	499.2	718.4	897.3
60	97.8	302.0	498.7	698.6	898.9

Table F.3 – Actual Reynolds number corresponding to nominal Reynolds number for wall-shear-stress results (BR = 39.7%)

X/H	Re = 100		Re = 300		Re = 500		Re = 700		Re = 900	
	τ_{avg}	τ_{rms}	τ_{avg}	τ_{rms}	τ_{avg}	τ_{rms}	τ_{avg}	τ_{rms}	τ_{avg}	τ_{rms}
3	1.44 E-02	5.34 E-04	1.10 E-02	4.93 E-04	2.98 E-02	5.47 E-03	4.64 E-02	1.95 E-02	6.67 E-02	5.02 E-02
4	1.63 E-02	6.12 E-04	1.70 E-02	6.50 E-04	2.76 E-02	9.81 E-03	8.71 E-02	6.13 E-02	1.71 E-01	1.13 E-01
6	1.75 E-02	6.26 E-04	6.01 E-02	1.13 E-03	1.99 E-01	1.94 E-02	3.85 E-01	1.14 E-01	6.05 E-01	2.24 E-01
8	1.52 E-02	5.72 E-04	2.32 E-02	6.79 E-04	1.64 E-02	9.54 E-04	3.04 E-02	1.75 E-02	8.27 E-02	6.37 E-02
10	1.55 E-02	6.28 E-04	3.09 E-02	8.39 E-04	1.74 E-02	2.28 E-03	6.91 E-02	6.20 E-02	1.83 E-01	1.36 E-01
12	1.74 E-02	6.05 E-04	4.24 E-02	8.84 E-04	7.37 E-02	1.06 E-02	1.34 E-01	3.42 E-02	2.15 E-01	6.09 E-02
14	1.61 E-02	6.00 E-04	3.92 E-02	8.82 E-04	7.21 E-02	7.38 E-03	1.22 E-01	2.32 E-02	1.85 E-01	4.07 E-02
20	1.53 E-02	5.78 E-04	3.43 E-02	7.98 E-04	5.81 E-02	3.41 E-03	8.63 E-02	1.32 E-02	1.35 E-01	2.72 E-02

Table F.4 – Wall-shear-stress data for the 76.3% blockage ratio (figure 5.1)

X/H	Re = 100		Re = 300		Re = 500		Re = 700		Re = 900	
	τ_{avg}	τ_{rms}	τ_{avg}	τ_{rms}	τ_{avg}	τ_{rms}	τ_{avg}	τ_{rms}	τ_{avg}	τ_{rms}
4	1.74 E-02	9.34 E-04	6.84 E-02	7.34 E-03	5.84 E-02	2.52 E-03	5.45 E-02	1.75 E-03	5.47 E-02	1.43 E-03
6	2.28 E-02	1.16 E-03	9.58 E-02	1.49 E-02	8.74 E-02	6.03 E-03	7.37 E-02	2.88 E-03	6.92 E-02	2.15 E-03
8	2.23 E-02	8.91 E-04	1.68 E-02	1.57 E-03	1.41 E-01	1.04 E-02	1.06 E-01	4.57 E-03	9.77 E-02	3.01 E-03
10	2.23 E-02	8.91 E-04	5.42 E-02	5.63 E-03	1.59 E-01	1.49 E-02	1.45 E-01	8.36 E-03	1.35 E-01	5.38 E-03
12	2.27 E-02	9.40 E-04	5.33 E-02	6.19 E-03	2.08 E-02	1.95 E-03	1.71 E-01	1.25 E-02	1.47 E-01	7.72 E-03
15	2.24 E-02	9.36 E-04	5.74 E-02	5.91 E-03	7.62 E-02	1.06 E-02	5.54 E-02	9.17 E-03	1.46 E-01	1.13 E-02
20	2.12 E-02	8.44 E-04	6.52 E-02	3.23 E-03	7.08 E-02	1.26 E-02	7.39 E-02	1.37 E-02	5.22 E-02	1.04 E-02
25	2.05 E-02	8.27 E-04	6.55 E-02	2.03 E-03	9.45 E-02	9.20 E-03	8.47 E-02	2.95 E-02	5.56 E-02	1.67 E-02
30	2.09 E-02	8.33 E-04	6.62 E-02	1.68 E-03	1.09 E-01	4.67 E-03	1.24 E-01	4.11 E-02	1.19 E-01	7.39 E-02
35	2.13 E-02	8.83 E-04	6.76 E-02	1.72 E-03	1.19 E-01	3.49 E-03	1.69 E-01	5.13 E-02	2.95 E-01	1.60 E-01
50	2.07 E-02	8.02 E-04	6.22 E-02	1.48 E-03	1.13 E-01	2.07 E-03	1.69 E-01	1.80 E-02	3.15 E-01	1.17 E-01
4R	1.78 E-02	7.36 E-04	6.70 E-02	4.68 E-03	5.76 E-02	1.90 E-03	4.99 E-02	1.32 E-03	4.56 E-02	1.13 E-03
4RR	1.73 E-02	7.58 E-04	6.71 E-02	4.68 E-03	5.70 E-02	1.91 E-03	4.94 E-02	1.34 E-03	4.54 E-02	1.14 E-03
25R	2.20 E-02	7.69 E-04	6.74 E-02	1.80 E-03	9.65 E-02	1.01 E-02	8.59 E-02	2.89 E-02	5.14 E-02	1.36 E-02
25RR	2.22 E-02	8.01 E-04	6.71 E-02	1.97 E-03	9.62 E-02	9.90 E-03	8.66 E-02	2.96 E-02	5.19 E-02	1.42 E-02
50R	2.04 E-02	7.79 E-04	6.26 E-02	1.49 E-03	1.14 E-01	1.97 E-03	1.63 E-01	1.40 E-02	2.57 E-01	8.34 E-02
50RR	1.97 E-02	7.83 E-04	6.13 E-02	1.45 E-03	1.12 E-01	1.93 E-03	1.62 E-01	1.44 E-02	2.60 E-01	8.59 E-02

Table F.5 – Wall-shear-stress data for the 59.2% blockage ratio (figure 5.2, 5.7, 5.8)

X/H	Re = 100		Re = 300		Re = 500		Re = 700		Re = 900	
	τ_{avg}	τ_{rms}	τ_{avg}	τ_{rms}	τ_{avg}	τ_{rms}	τ_{avg}	τ_{rms}	τ_{avg}	τ_{rms}
4	2.08 E-02	6.50 E-04	1.87 E-02	6.30 E-04	1.66 E-02	6.20 E-04	2.60 E-02	7.00 E-04	3.41 E-02	7.50 E-04
5	2.18 E-02	7.00 E-04	2.06 E-02	6.90 E-04	1.79 E-02	6.90 E-04	3.92 E-02	8.90 E-04	5.95 E-02	9.80 E-04
6	2.29 E-02	7.10 E-04	2.86 E-02	7.50 E-04	1.67 E-02	6.40 E-04	3.46 E-02	8.40 E-04	5.98 E-02	9.80 E-04
8	1.92 E-02	6.90 E-04	4.58 E-02	8.70 E-04	3.16 E-02	8.20 E-04	1.87 E-02	6.80 E-04	3.63 E-02	9.30 E-04
10	2.35 E-02	6.60 E-04	5.56 E-02	9.00 E-04	5.93 E-02	9.30 E-04	3.26 E-02	7.90 E-04	2.77 E-02	7.40 E-04
12	2.33 E-02	6.70 E-04	5.70 E-02	9.20 E-04	7.57 E-02	1.04 E-03	6.49 E-02	1.03 E-03	3.61 E-02	8.40 E-04
13	2.25 E-02	6.70 E-04	5.57 E-02	9.10 E-04	7.64 E-02	1.02 E-03	6.99 E-02	1.04 E-03	6.64 E-02	
14	2.17 E-02	6.90 E-04	5.69 E-02	9.30 E-04	8.09 E-02	1.06 E-03	9.62 E-02	1.15 E-03	8.21 E-02	1.22 E-03
17	2.01 E-02	6.70 E-04	5.88 E-02	9.40 E-04	8.31 E-02	1.06 E-03	1.07 E-01	1.26 E-03	1.28 E-01	1.43 E-03
20	2.16 E-02	7.10 E-04	6.25 E-02	1.00 E-03	8.91 E-02	1.13 E-03	1.08 E-01	1.34 E-03	1.32 E-01	1.81 E-03
25	2.09 E-02	6.80 E-04	6.34 E-02	1.01 E-03	9.63 E-02	1.16 E-03	1.17 E-01	1.59 E-03	1.32 E-01	2.87 E-03
30	2.05 E-02	6.60 E-04	6.25 E-02	9.70 E-04	9.84 E-02	1.15 E-03	1.23 E-01	1.79 E-03	1.32 E-01	
35	2.23 E-02	8.00 E-04	6.61 E-02	1.29 E-03	1.07 E-01	1.78 E-03	1.37 E-01	2.52 E-03	1.58 E-01	8.62 E-03
45	2.34 E-02	8.60 E-04	6.67 E-02	1.23 E-03	1.09 E-01	1.43 E-03	1.47 E-01	1.81 E-03	1.78 E-01	9.99 E-03
60	2.32 E-02	8.30 E-04	6.43 E-02	1.23 E-03	1.09 E-01	1.41 E-03	1.51 E-01	1.60 E-03	1.90 E-01	5.74 E-03

Table F.6 – Wall-shear-stress data for the 39.7% blockage ratio (figure 5.3)

X/H	Re = 100	Re = 300	Re = 500	Re = 700	Re = 900
3	3.74E-02	4.67E-02	1.79E-01	4.16E-01	7.50E-01
4	4.06E-02	4.10E-02	3.61E-01	6.36E-01	6.18E-01
6	3.82E-02	1.83E-02	9.09E-02	2.72E-01	3.40E-01
8	4.09E-02	3.04E-02	6.28E-02	5.44E-01	7.14E-01
10	4.40E-02	2.76E-02	1.27E-01	8.10E-01	6.92E-01
12	3.73E-02	2.07E-02	1.39E-01	2.41E-01	2.63E-01
14	4.04E-02	2.24E-02	9.90E-02	1.79E-01	2.05E-01
20	4.10E-02	2.34E-02	5.72E-02	1.46E-01	1.89E-01

Table F.7 – Wall-shear-stress intensity data for the 76.3% blockage ratio (figure 5.4)

X/H	Re = 100	Re = 300	Re = 500	Re = 700	Re = 900
4	5.37E-02	1.07E-01	4.30E-02	3.20E-02	2.62E-02
6	5.09E-02	1.55E-01	6.90E-02	3.90E-02	3.10E-02
8	4.00E-02	9.32E-02	7.35E-02	4.33E-02	3.08E-02
10	4.00E-02	1.04E-01	9.40E-02	5.75E-02	3.98E-02
12	4.14E-02	1.16E-01	9.36E-02	7.28E-02	5.24E-02
15	4.18E-02	1.03E-01	1.39E-01	1.66E-01	7.74E-02
20	3.98E-02	4.96E-02	1.78E-01	1.85E-01	2.00E-01
25	4.04E-02	3.09E-02	9.74E-02	3.49E-01	3.01E-01
30	3.98E-02	2.53E-02	4.27E-02	3.31E-01	6.19E-01
35	4.15E-02	2.55E-02	2.93E-02	3.03E-01	5.42E-01
50	3.87E-02	2.39E-02	1.83E-02	1.07E-01	3.70E-01
4R	4.13E-02	6.98E-02	3.30E-02	2.65E-02	2.47E-02
4RR	4.39E-02	6.97E-02	3.35E-02	2.71E-02	2.52E-02
25R	3.49E-02	2.67E-02	1.05E-01	3.36E-01	2.65E-01
25RR	3.61E-02	2.93E-02	1.03E-01	3.41E-01	2.74E-01
50R	3.81E-02	2.37E-02	1.73E-02	8.61E-02	3.25E-01
50RR	3.97E-02	2.37E-02	1.72E-02	8.86E-02	3.30E-01

Table F.8 – Wall-shear-stress intensity data for the 59.2% blockage ratio (figure 5.5)

X/H	Re = 100	Re = 300	Re = 500	Re = 700	Re = 900
4	3.13E-02	3.37E-02	3.73E-02	2.69E-02	2.20E-02
5	3.21E-02	3.35E-02	3.85E-02	2.27E-02	1.65E-02
6	3.10E-02	2.62E-02	3.83E-02	2.43E-02	1.64E-02
8	3.60E-02	1.90E-02	2.59E-02	3.64E-02	2.56E-02
10	2.81E-02	1.62E-02	1.57E-02	2.42E-02	2.68E-02
12	2.88E-02	1.62E-02	1.37E-02	1.59E-02	2.33E-02
13	2.97E-02	1.63E-02	1.33E-02	1.49E-02	
14	3.18E-02	1.63E-02	1.31E-02	1.20E-02	1.49E-02
17	3.33E-02	1.60E-02	1.28E-02	1.18E-02	1.12E-02
20	3.29E-02	1.60E-02	1.27E-02	1.24E-02	1.37E-02
25	3.25E-02	1.59E-02	1.20E-02	1.36E-02	2.18E-02
30	3.23E-02	1.55E-02	1.17E-02	1.46E-02	
35	3.59E-02	1.95E-02	1.67E-02	1.84E-02	5.46E-02
45	3.68E-02	1.85E-02	1.31E-02	1.23E-02	5.60E-02

Table F.9 – Wall-shear-stress intensity data for the 39.7% blockage ratio (figure 5.6)

X/H	Re = 100	Re = 300	Re = 500	Re = 700	Re = 900
5	0.01851	-0.0177	-0.0799	-0.1036	-0.1150
6	0.01971	0.00636	-0.0719	-0.1138	-0.1305
8	0.02000	0.03807	-0.0153	-0.1077	-0.1553
10	0.02006	0.04735	0.04226	-0.0371	-0.1449
12	0.02012	0.05042	0.06355	0.04185	-0.0548
13	0.02014	0.05196	0.06777	0.06871	0.01614
14	0.02015	0.05312	0.06964	0.07919	0.05998
17	0.02012	0.05641	0.07573	0.08702	0.10881
20	0.02011	0.05837	0.08279	0.09240	0.10323
25	0.02011	0.05837	0.08279	0.09240	0.10323
30	0.02012	0.05998	0.09561	0.11956	0.13337
35	0.02012	0.06024	0.09794	0.12701	0.14554
45	0.02012	0.06036	0.09950	0.13513	0.15821

Table F.10 – Numerical results for the evolution of the average wall-shear-stress downstream of the 39.7% blockage (figure 5.9)

Appendix G

Data for Figures in Section 5.3

Nominal Re	Actual Re		
	BR = 38%	BR = 57%	BR = 76%
100	99.3	102.4	99.8
300	300.1	300.3	299.2
500	500.5	500.5	498.0
600	602.3	599.3	598.5
700	699.9	698.7	698.8
700 R	NA	NA	699.9
800	796.7	801.8	800.6
900	900.0	901.3	901.3
900 R	902.9	902.2	NA

Table G.1 – Actual Reynolds number corresponding to nominal Reynolds number for pressure distribution results (R represents a repeated Reynolds number)

38.2% Blockage Ratio							
Distance from Reference Point (m)	Pressure Drop from Reference Point (Pa)						
	Re = 100	Re = 300	Re = 500	Re = 600	Re = 700	Re = 800	Re = 900
0.0127	0.25	0.73	1.21	1.46	1.70	1.91	2.19
0.0255	0.50	1.44	2.43	2.91	3.37	3.83	4.33
0.0382	0.74	2.21	3.69	4.42	5.14	5.83	6.63
0.0509	0.99	2.92	4.94	5.90	6.84	7.80	8.80
0.0573	1.12	3.31	5.54	6.63	7.72	8.75	9.89
0.0637	1.24	3.68	6.18	7.42	8.61	9.77	11.07
0.0698	1.37	4.07	6.81	8.18	9.50	10.77	12.22
0.0764	1.61	5.20	9.39	11.61	13.90	16.24	18.98
0.0827	2.29	8.23	15.87	20.25	24.73	29.46	34.98
0.0891	2.84	9.90	18.87	24.04	29.26	34.73	41.13
0.0954	3.38	11.55	21.69	27.47	33.01	38.64	45.16
0.1016	3.91	12.56	22.31	27.70	33.39	38.88	45.24
0.1081	3.92	12.61	22.47	27.87	33.40	39.33	45.63
0.1145	4.04	12.87	22.91	28.07	33.58	39.39	46.44
0.1209	4.17	13.15	23.34	28.73	34.00	39.61	46.80
0.1272	4.29	13.24	23.52	29.42	34.77	40.17	46.99
0.1335	4.43	13.60	24.08	29.52	35.56	41.02	47.37
0.1399	4.55	13.98	24.40	30.15	35.83	41.84	48.24
0.1462	4.67	14.36	24.69	30.75	36.34	42.64	49.48
0.1526	4.81	14.75	25.30	30.88	37.25	42.90	50.63
0.1589	4.94	15.13	25.99	31.64	37.26	44.03	51.97
0.1908	5.56	17.02	29.11	35.36	41.59	47.72	54.81
0.2225	6.18	18.88	32.19	39.01	45.75	52.50	60.24
0.2541	6.80	20.70	35.21	42.68	49.94	57.20	65.46
0.2858	7.42	22.53	38.25	46.25	54.05	61.87	70.77

Table G.2 – Pressure distribution data for 38.2% blockage ratio (figure 5.12)

57.2% Blockage Ratio							
Distance from Reference Point (m)	Pressure Drop from Reference Point (Pa)						
	Re = 100	Re = 300	Re = 500	Re = 600	Re = 700	Re = 800	Re = 900
0.0127	0.24	0.70	1.21	1.41	1.67	1.88	2.11
0.0255	0.49	1.41	2.35	2.77	3.25	3.68	4.12
0.0382	0.73	2.13	3.54	4.19	4.88	5.56	6.19
0.0509	0.98	2.84	4.68	5.53	6.44	7.29	8.14
0.0573	1.10	3.17	5.23	6.19	7.19	8.14	9.05
0.0637	1.23	3.54	5.81	6.87	7.98	9.04	10.03
0.0698	1.34	3.87	6.41	7.54	8.73	9.87	10.95
0.0764	1.88	6.94	14.09	18.29	23.05	28.31	33.84
0.0827	4.75	18.93	39.69	51.87	65.49	80.56	96.53
0.0891	7.15	26.10	52.08	66.95	83.36	101.49	120.59
0.0954	9.61	33.37	64.34	81.68	100.78	121.73	143.05
0.1016	12.13	39.47	72.65	90.94	110.61	131.76	152.69
0.1081	12.18	39.73	72.77	91.15	110.80	131.83	152.72
0.1145	12.26	39.88	73.20	91.67	111.03	132.83	154.30
0.1209	12.38	40.07	73.84	91.77	111.87	132.84	155.86
0.1272	12.50	40.49	74.04	92.36	112.75	134.42	156.28
0.1335	12.60	40.77	74.49	93.35	113.48	136.31	160.06
0.1399	12.77	40.83	75.11	93.63	114.89	139.40	163.50
0.1462	12.87	41.19	75.38	96.66	117.40	140.29	164.23
0.1526	12.99	41.28	76.77	96.72	118.20	141.47	165.58
0.1589	13.14	41.59	78.16	96.98	119.60	143.71	168.49
0.1908	13.78	43.41	78.43	98.80	120.94	144.73	169.11
0.2225	14.36	45.23	81.13	100.61	121.58	145.12	169.81
0.2541	15.01	47.11	84.08	104.19	125.70	149.74	174.30
0.2858	15.64	48.87	87.17	107.77	129.87	154.41	179.38

Table G.3 – Pressure distribution data for 57.2% blockage ratio (figure 5.13)

76.2% Blockage Ratio							
Distance from Reference Point (m)	Pressure Drop from Reference Point (Pa)						
	Re = 100	Re = 300	Re = 500	Re = 600	Re = 700	Re = 800	Re = 900
0.0127	0.23	0.67	1.11	1.31	1.43	1.63	1.83
0.0255	0.47	1.34	2.16	2.52	2.74	3.10	3.44
0.0382	0.70	1.99	3.22	3.76	4.01	4.53	5.04
0.0509	0.91	2.61	4.19	4.88	5.15	5.79	6.39
0.0573	1.03	2.92	4.66	5.40	5.68	6.39	7.08
0.0637	1.14	3.23	5.11	5.94	6.23	7.02	7.77
0.0698	1.25	3.54	5.58	6.49	6.53	7.29	7.98
0.0764	1.97	8.12	16.98	22.36	6.78	7.67	8.45
0.0827	17.18	66.56	136.74	180.36	875.58	1006.30	1126.60
0.0891	31.06	107.46	204.07	261.17	904.30	1016.80	1131.20
0.0954	45.82	151.42	276.93	347.30	906.37	1019.40	1132.60
0.1016	63.37	204.09	360.82	446.13	906.45	1020.90	1134.50
0.1081	64.28	204.26	361.82	447.73	909.15	1021.80	1137.60
0.1145	64.29	204.28	361.91	447.82	911.15	1025.30	1138.50
0.1209	64.44	204.32	363.00	448.55	911.57	1026.70	1138.70
0.1272	64.54	204.94	363.60	449.46	911.87	1034.60	1148.80
0.1335	64.68	205.19	363.90	449.91	917.47	1035.40	1154.90
0.1399	64.79	205.19	363.95	451.98	919.70	1039.50	1155.30
0.1462	64.89	205.62	364.30	451.98	921.79	1040.80	1159.20
0.1526	65.02	205.81	367.58	454.79	922.49	1041.30	1159.40
0.1589	65.21	207.32	368.51	457.65	922.84	1042.40	1160.30
0.1908	65.81	207.76	369.50	457.89	924.07	1042.70	1162.20
0.2225	66.46	209.81	371.11	458.40	924.49	1043.80	1162.70
0.2541	67.05	211.65	373.44	461.75	926.59	1043.90	1162.80
0.2858	67.65	213.47	376.63	465.23	930.70	1048.70	1165.80

Table G.4 – Pressure distribution data for 76.2% blockage ratio (figure 5.14)